



UNIVERSITAT
POLITÈCNICA
DE VALÈNCIA



UNIVERSITAT POLITÈCNICA DE VALÈNCIA

School of Industrial Engineering

Analysis of the mechanical behaviour and structural
characterisation of high entropy quaternary alloys

Master's Thesis

Master's Degree in Industrial Engineering

AUTHOR: González Guillén, Celia

Tutor: Amigó Borrás, Vicente

External cotutor: ROMERO RESENDIZ, LILIANA

Experimental director: VICENTE ESCUDER, ANGEL

ACADEMIC YEAR: 2021/2022



UNIVERSITAT
POLITÈCNICA
DE VALÈNCIA



ESCUOLA TÉCNICA
SUPERIOR INGENIERÍA
INDUSTRIAL VALENCIA

INDUSTRIAL ENGINEERING MASTER THESIS

ANALYSIS OF THE MECHANICAL BEHAVIOUR AND STRUCTURAL CHARACTERISATION OF HIGH ENTROPY QUATERNARY ALLOYS

AUTHOR: CELIA GONZÁLEZ GUILLÉN

SUPERVISOR: VICENTE AMIGÓ BORRÁS

SUPERVISOR: ÁNGEL VICENTE ESCUDER, LILIANA ROMERO RESENDIZ

Academic year: 2021-22

To my family

ACKNOWLEDGEMENTS

I would like to thank all those who have been part of this project, starting with Dr. Vicente Amigó, who placed his trust in me from the very beginning. I would also like to thank Mr. Ángel Vicente and Dr. Liliana Romero, who have helped me along the way, as well as Dr. Gonzalo González and my lab partners.

But, above all, to my family, for their unconditional support, and to Andrés, for accompanying and helping me on this long path.

RESUMEN

Los avances de los materiales de alta entropía han llevado a distintas aplicaciones de los mismos como materiales estructurales o biomateriales entre otros. Estas aleaciones, a diferencia de las convencionales donde se tiene una matriz de un elemento principal a la que se le añaden precipitados de otros elementos para mejorar sus propiedades en función de su aplicación, se componen de al menos cinco elementos principales, lo que resulta en un material que posee una alta entropía de mezcla que determina la formación de las fases y, en consecuencia, el comportamiento del material. Aquellas aleaciones compuestas de cuatro elementos principales se denominan de media entropía. El comportamiento mecánico a elevadas temperaturas es una de las propiedades que se mejoran en las aleaciones de alta y media entropía con respecto a las convencionales.

Dentro de los materiales, los elementos que más biocompatibilidad poseen son el circonio, titanio, niobio y tántalo, en ese mismo orden, siendo además elementos refractarios que permiten mantener sus propiedades mecánicas y frente a la oxidación en aplicaciones donde las temperaturas pueden alcanzar niveles muy elevados. Por lo anterior, se desarrollaron aleaciones cuaternarias de media entropía. Distintas aleaciones de Ti-Nb-Zr-Ta fueron fabricadas con diferentes proporciones, equiatómicas y equimásicas, por técnicas de pulvimetalurgia y fusión por arco eléctrico, consiguiendo de este modo una aleación que, a priori, se entiende por muy biocompatible y que podría paliar los efectos negativos de emplear, en aplicaciones biomédicas, aleaciones con elementos tóxicos como el aluminio o el vanadio.

Las aleaciones obtenidas se caracterizaron microestructural y mecánicamente utilizando ensayos en microprobetas para poder determinar sus principales parámetros mecánicos. Además, se elaboró el presupuesto asociado al desarrollo del presente trabajo, el cual ascendió a una cantidad de treinta y cinco mil setecientos sesenta y tres euros y cuarenta y ocho céntimos.

Palabras clave: Aleaciones de media entropía; Ti-Nb-Zr-Ta; pulvimetalurgia; aleación mecánica; microestructura; caracterización mecánica; caracterización química.

Aportación a los ODS: El desarrollo de este trabajo está directamente vinculado a tres de los Objetivos de Desarrollo Sostenible (ODS), (3) Salud y Bienestar, (9) Industria, Innovación e Infraestructura y (12) Producción y Consumo Responsables. En este sentido, se busca indagar en nuevas aleaciones que puedan permitir una mayor vida útil de los implantes, acompañando así al incremento de la esperanza de vida de la población, lo que resulta beneficioso para la salud y el bienestar social. Para ello, es necesario estudiar aleaciones cuyo proceso de fabricación sea posteriormente industrializable para su comercialización, de modo que se encuentra asociado con la industria manufacturera. Finalmente, para el desarrollo del proyecto de investigación se ha trabajado con procesos pulvimetalúrgicos, los cuales proporcionan un mayor aprovechamiento de la materia prima, consiguiendo con ello un consumo responsable.

RESUM

Els avanços dels materials d'alta entropia han portat a diferents aplicacions dels mateixos com a materials estructurals o biomaterials entre altres. Aquests aliatges, a diferència de les convencionals on es té una matriu d'un element principal a la qual se li afigen precipitats d'altres elements per a millorar les seues propietats en funció de la seua aplicació, es componen d'almenys cinc elements principals, la qual cosa resulta en un material que posseeix una alta entropia de mescla que determina la formació de les fases i, en conseqüència, el comportament del material. Aquells aliatges compostos de quatre elements principals es denominen de mitja entropia. El comportament mecànic a elevades temperatures és una de les propietats que es milloren en els aliatges d'alta i mitjana entropia respecte als convencionals.

Dins dels materials, els elements que més biocompatibilitat posseeixen són el zirconi, titani, niobi i tàntal, en aqueix mateix ordre, sent a més elements refractaris que permeten mantindre les seues propietats mecàniques i enfront de l'oxidació en aplicacions on les temperatures poden aconseguir nivells molt elevats. Per l'anterior, es van desenvolupar aliatges quaternaris de mitja entropia. Diferents aliatges de Ti-Nb-Zr-Ta van ser fabricades amb diferents proporcions, equiatòmiques i equimàsiques, per tècniques de pulvimetalurgia i fusió per arc elèctric, aconseguint d'aquesta manera un aliatge que, a priori, s'entén per molt biocompatible i que podria pal·liar els efectes negatius d'emprar, en aplicacions biomèdiques, aliatges amb elements tòxics com l'alumini o el vanadi.

Els aliatges obtinguts es van caracteritzar microestructural i mecànicament utilitzant assajos en microprovetes per a poder determinar els seus principals paràmetres mecànics. A més, es va elaborar el pressupost associat al desenvolupament del present treball, el qual va ascendir a una quantitat de trenta-cinc mil set-cents seixanta-tres euros i quaranta-huit cèntims.

Paraules clau: Aliatges de mitja entropia; Ti-Nb-Zr-Ta; pulvimetalurgia; aliatge mecànic; microestructura; caracterització mecànica; caracterització química.

Aportació als ODS: El desenvolupament d'aquest treball està directament vinculat a tres dels Objectius de Desenvolupament Sostenible (ODS), (3) Salut i Benestar, (9) Indústria, Innovació i Infraestructura i (12) Producció i Consum Responsables. En aquest sentit, es busca indagar en nous aliatges que puguin permetre una major vida útil dels implants, acompanyant així a l'increment de l'esperança de vida de la població, la qual cosa resulta beneficiós per a la salut i el benestar social. Per a això, és necessari estudiar aliatges que el seu procés de fabricació siga posteriorment industrializable per a la seua comercialització, de manera que es troba associat amb la indústria manufacturera. Finalment, per al desenvolupament del projecte d'investigació s'ha treballat amb processos pulvimetalúrgics, els quals proporcionen un major aprofitament de la matèria primera, aconseguint amb això un consum responsable.

ABSTRACT

Advances in high entropy materials have led to various applications of these materials as structural materials or biomaterials, among others. Unlike the conventional ones, where there is a matrix of the main element to which precipitates of other elements are added to improve their properties, high entropy alloys are composed of at least five main elements. As a result, the material has a high entropy of mixture, which determines the formation of the phases and its mechanical behaviour. The mechanical behaviour at high temperatures is one of the properties that is improved in high and medium entropy alloys concerning the conventional ones.

Among the materials, the most biocompatible elements are zirconium, titanium, niobium, and tantalum, in that order, being also refractory elements that allow maintaining their mechanical properties and against oxidation in applications where temperatures can reach very high levels. Therefore, quaternary alloys of medium entropy were developed in this work. Different Ti-Nb-Zr-Ta alloys were manufactured with different equiatomic and equiatomic ratios by powder metallurgy and electric arc melting techniques, thus achieving an alloy that, a priori, is understood to be very biocompatible and that could alleviate the adverse effects to use, in biomedical applications, alloys with toxic elements such as aluminium or vanadium.

The alloys obtained were microstructurally and mechanically characterised using microprobes tests to determine their main mechanical parameters. In addition, the budget associated with developing this work was drawn up, which amounted to thirty-five thousand seven hundred and sixty-three euros and forty-eight cents.

Keywords: medium-entropy alloys; Ti-Nb-Zr-Ta; powder metallurgy; mechanical alloying; microstructure; mechanical characterisation; chemical characterisation.

Contribution to the SDGs: The development of this work is directly linked to three of the Sustainable Development Goals (SDGs), (3) Good Health and Well-being, (9) Industry, Innovation, and Infrastructure, and (12) Responsible Consumption and Production. In this sense, the aim is to investigate new alloys that can enable implants to last longer, thus

accompanying the increase in life expectancy of the population, which is beneficial for health and social well-being. To this end, it is necessary to study alloys whose manufacturing process can subsequently be industrialised to be marketed, what is related to the manufacturing industry. Finally, powder metallurgical processes have been used to develop the research project, which provides better use of the raw materials and, consequently, responsible consumption.

DOCUMENTS

DOCUMENT I: REPORT

In this first document, background, motivation, objectives, and discussion and analysis of results are exposed, among others. Thus, it can be considered the central document of this work.

DOCUMENT II: BUDGET

This second document details the budget for carrying out a project of these characteristics. In it, different chapters, which are broken down into other units of work consisting of machinery, materials, and workforce, can be found.

CONTENTS FOR BOTH DOCUMENTS

<i>DOCUMENT I: REPORT</i>	<i>i</i>
1. INTRODUCTION	1
1.1. BACKGROUND	1
1.2. MOTIVATION	7
1.3. OBJECTIVES	9
2. WORKING PLAN	12
3. MATERIALS AND METHODS	15
3.1. SAMPLE COLLECTION	15
3.1.1. Conventional powder metallurgy	20
3.1.2. As cast	27
3.2. MICROSTRUCTURAL CHARACTERISATION	29
3.2.1. X-Ray Diffraction	29
3.2.2. Optical Microscopy	30
3.2.3. Field - Emission Scanning Electron Microscopy	31
3.2.4. Electron Backscatter Diffraction	33
3.2.5. Transmission Electron Microscopy	35
3.3. MECHANICAL CHARACTERISATION	40
3.3.1. Archimedes test	40
3.3.2. Determination of elastic modulus by ultrasounds	41
3.3.3. Hardness test	42
3.3.4. Microhardness test	42
3.3.5. 4-Point bending, micro-tensile, and micro-compression tests	42
3.3.6. Small punch test	47

3.4. CHEMICAL CHARACTERISATION	49
3.4.1. Electrochemical corrosion	49
3.4.2. Wettability and contact angle	53
4. RESULTS.....	56
4.1. POWDER OBTENTION BY MECHANICAL ALLOYING.....	56
4.2. MICROSTRUCTURAL CHARACTERISATION.....	61
4.2.1. Porosity.....	62
4.2.2. Crystallographic phase distribution.....	65
4.2.3. Chemical distribution throughout the phases	66
4.2.4. Crystalline structure.....	70
4.2.5. Crystallographic orientation	77
4.3. MECHANICAL CHARACTERISATION	79
4.3.1. Hardness	80
4.3.2. Microhardness	81
4.3.3. Determination of elastic modulus by ultrasounds	82
4.3.4. 4-Point bending, micro-tensile, and micro-compression tests	83
4.3.5. Small-punch test.....	85
4.3.6. Fractography analysis.....	87
4.4. CHEMICAL CHARACTERISATION	88
4.4.1. Corrosion resistance	88
4.4.2. Wettability	91
5. EXPERIMENTAL DISCUSSION.....	93
6. CONCLUSIONS.....	104
7. FUTURE WORKS	106
8. REFERENCES	107

RESULT'S DISSEMINATION 112

DOCUMENT II:..... i

1. UNIT PRICES 1

2. PRICE BREAKDOWN 5

3. EXECUTION BUDGET 20

4. OVERALL BUDGET 23



UNIVERSITAT
POLITÈCNICA
DE VALÈNCIA



ESCUELA TÉCNICA
SUPERIOR INGENIERÍA
INDUSTRIAL VALENCIA

ANALYSIS OF THE MECHANICAL BEHAVIOUR AND STRUCTURAL CHARACTERISATION OF HIGH ENTROPY QUATERNARY ALLOYS

DOCUMENT I: REPORT

CELIA GONZÁLEZ GUILLÉN

Student, Instituto de Tecnología de Materiales, Universitat Politècnica de Valencia, Valencia, Spain

VICENTE AMIGÓ BORRÁS

University Professor, Instituto de Tecnología de Materiales, Universitat Politècnica de Valencia, Valencia, Spain

ÁNGEL VICENTE ESCUDER

Teaching and Research Staff, Instituto de Tecnología de Materiales, Universitat Politècnica de Valencia, Valencia, Spain

LILIANA ROMERO RESENDIZ

Postdoctoral Researcher, Materials Science and Engineering Department, City University of Hong Kong, Hong Kong

CONTENTS

1. INTRODUCTION.....	1
1.1. BACKGROUND	1
1.2. MOTIVATION.....	7
1.3. OBJECTIVES.....	9
2. WORKING PLAN	12
3. MATERIALS AND METHODS.....	15
3.1. SAMPLE COLLECTION	15
3.1.1. Conventional powder metallurgy.....	20
3.1.2. As cast	27
3.2. MICROSTRUCTURAL CHARACTERISATION.....	29
3.2.1. X-Ray Diffraction	29
3.2.2. Optical Microscopy	30
3.2.3. Field - Emission Scanning Electron Microscopy	31
3.2.4. Electron Backscatter Diffraction	33
3.2.5. Transmission Electron Microscopy.....	35
3.3. MECHANICAL CHARACTERISATION	40
3.3.1. Archimedes test.....	40
3.3.2. Determination of elastic modulus by ultrasounds	41
3.3.3. Hardness test.....	42
3.3.4. Microhardness test.....	42
3.3.5. 4-Point bending, micro-tensile, and micro-compression tests	42
3.3.6. Small punch test	47
3.4. CHEMICAL CHARACTERISATION	49
3.4.1. Electrochemical corrosion	49

3.4.2. Wettability and contact angle	53
4. RESULTS.....	56
4.1. POWDER OBTENTION BY MECHANICAL ALLOYING.....	56
4.2. MICROSTRUCTURAL CHARACTERISATION.....	61
4.2.1. Porosity.....	62
4.2.2. Crystallographic phase distribution.....	65
4.2.3. Chemical distribution throughout the phases	66
4.2.4. Crystalline structure.....	70
4.2.5. Crystallographic orientation	77
4.3. MECHANICAL CHARACTERISATION	79
4.3.1. Hardness	80
4.3.2. Microhardness	81
4.3.3. Determination of elastic modulus by ultrasounds	82
4.3.4. 4-Point bending, micro-tensile, and micro-compression tests	83
4.3.5. Small-punch test.....	85
4.3.6. Fractography analysis.....	87
4.4. CHEMICAL CHARACTERISATION	88
4.4.1. Corrosion resistance	88
4.4.2. Wettability	91
5. EXPERIMENTAL DISCUSSION.....	93
6. CONCLUSIONS.....	104
7. FUTURE WORKS	106
8. REFERENCES	107
RESULT'S DISSEMINATION	112

LIST OF FIGURES

Fig. 1. Alloying philosophy in (a) conventional metallurgy and (b) HEAs (Torralba & García-Junceda, 2019).....	1
Fig. 2. Titanium binary phase diagram: (a) α -stabiliser, (b) isomorphic β -stabiliser, (c) eutectoid β -stabiliser, and (d) neutral.	7
Fig. 3. Main alloying elements in the HEAs studied (Torralba & García-Junceda, 2019).....	8
Fig. 4. Hip replacement per one hundred thousand inhabitants' evolution (Lario, Poler & Amigó, 2022).	9
Fig. 5. (a) Ti, (b) Nb, (c) Zr hydride, and (d) Ta powder secondary electron images.	17
Fig. 6. (a) Ti, (b) Nb, (c) Zr hydride, and (d) Ta powder particle size distribution.	18
Fig. 7. XRD of Ti, Nb, Zr, and Ta powders used as raw materials.	19
Fig. 8. Sample collection route followed to obtain TNZT MEAs.	20
Fig. 9. Glove box of the Jacomex manufacturer, model GP Campus.....	22
Fig. 10. Planetary ball mill of the Retsch manufacturer, model PM 400/2 (ITM).	22
Fig. 11. Process of preparing the stainless-steel jars prior to mechanical alloying (MA): (a) balls introduction, (b) dust discharge, and (c) final result (ITM).....	23
Fig. 12. Floating bending die seen from (a) a front and (b) a top view.	24
Fig. 13. High vacuum furnace of the manufacturer Carbolite Gero Limited, model HVT 15-75-450.....	25
Fig. 14. Sintering cycle.	26
Fig. 15. Grain formation process during sintering: (a) before, (b) after.	26
Fig. 16. Arc melting furnace of the Edmund Bühler GmbH manufacturer, model MAM-1...	27
Fig. 17. Grain formation process during casting: (a) first step, (b) second step, (c) third step, (d) fourth step.	28
Fig. 18. Metallographic preparation of the samples with two types of resin: non-conductive and conductive.....	31
Fig. 19. (a) Sketch of the operation principle of the FESEM microscope and (b) sample placement in the sample holder.	32
Fig. 20. FESEM ZEISS ULTRA 55 (Servicio de Microscopía Electrónica of the UPV).	32
Fig. 21. Fractures of (a) equiatomic and (b) equimassic TNZT press and sinter samples.....	33
Fig. 22. Kikuchi bands obtained by EBSD.	33
Fig. 23. FIB ZEISS AURIGA Compact (Servicio de Microscopía Electrónica of the UPV).	34

Fig. 24. (a) Sketch of the operation principle of the EBSD microscope and (b) sample placement in the sample holder.	34
Fig. 25. TEM JEOL JEM 2100F (Servicio de Microscopía Electrónica of the UPV).....	35
Fig. 26. Electron Microscopy operation principle.	36
Fig. 27. Lamella obtained by FIB for TEM.	36
Fig. 28. (a) Horizontal distance measurement between (b) the diffraction points.	37
Fig. 29. (a) Vertical distance measurement between (b) the diffraction points.	37
Fig. 30. (a) Diagonal distance measurement between (b) the diffraction points.	38
Fig. 31. (a) Measurement of the angle between d_1 and d_2 and (b) association to a crystallographic plane.	39
Fig. 32. (a) Measurement of the angle between d_1 and d_3 and (b) association to a crystallographic plane.	39
Fig. 33. (a) Measurement of the angle between d_2 and d_3 and (b) association to a crystallographic plane.	39
Fig. 34. Archimedes equipment (a) during and (b) after its assembly.	40
Fig. 35. Shimadzu Autograph AG-100 KN Xplus universal testing machine.	43
Fig. 36. Bending test (a) sketch and (b) procedure.	44
Fig. 37. Sample (a) before and (b) after the 4-point bending test.	44
Fig. 38. (a) Samples geometry for micro-tensile test in mm and (b) micro-tensile test procedure.	45
Fig. 39. Sample (a) before and (b) after the tensile test.	45
Fig. 40. (a) Samples geometry for micro-compression test in mm and (b) micro-compression test procedure.	46
Fig. 41. Sample (a) before and (b) after the compression test.	46
Fig. 42. (a) Dimensions of the ball used during small punch test in mm and (b) small punch test procedure.	47
Fig. 43. Sketch of (c) the top and (d) the bottom of the small punch tooling in mm.	48
Fig. 44. Sample (a) before and (b) after the small punch test.	48
Fig. 45. Small-punch data treatment of the TNZT equiatomic mechanical alloying sample by powder metallurgy number 05 (EA-MA-PM_05) where yellow, and green line represents the elastic and the plastic slope, respectively, blue line the first breakage, and the grey one the maximum supported force by the sample.	49

Fig. 46. Potentiodynamic polarisation curve.	50
Fig. 47. (a) Complex plane and (b)(c)Bode plots for (d) a double-porous-layer circuit $R_0(R_1C_1)(R_2C_2)$ where R_0 represent the electrolyte resistance, R_1C_1 the compact layer, and R_2C_2 the porous one (Lasia, 2014).	51
Fig. 48. Effect of (a) capacitance and (b) resistance in the complex impedance plane by means of Nyquist plots (Martín & Bautista, 2014).	52
Fig. 49. Electrochemical corrosion equipment.	53
Fig. 50. (a) DSA25S KRÜSS Drop Shape Analyzer and (b)results obtained for the TNZT equiatomic mechanical alloying sample by powder metallurgy and casting, were Θ^l represents de contact angle measured on the left side and Θ^d that measured on the right one.	54
Fig. 51. Wettability procedure for TNZT mechanical alloying samples (a) by powder metallurgy and (b) by powder metallurgy and casting.	55
Fig. 52. Cross section of the equiatomic TNZT mechanically alloyed powder by (a) SE, and (b) BSE, and the equimassic TNZT mechanically alloyed powder by (c) SE, (d) BSE.	57
Fig. 53. TNZT alloyed powder particle size distribution for (■) equiatomic and (■) equimassic composition.	59
Fig. 54. TNZT alloyed powders XRD that shows crystallographic planes for each diffraction pick according to the distinct phases detailed.	59
Fig. 55. TNZT samples shrinkage after sintering for (■) equiatomic and (■) equimassic mechanical alloying by powder metallurgy: (a) length, width, and thickness, (b) volume.	60
Fig. 56. Comparison between equiatomic and equimassic TNZT mechanical alloying samples density before and after sintering.	61
Fig. 57. Influence of sample positioning during the sintering process on porosity.	62
Fig. 58. Relatively porosity comparison between (■) equiatomic and (■) equimassic TNZT mechanical alloying by powder metallurgy, and (■) equiatomic and (■) equimassic TNZT mechanical alloying by powder metallurgy and casting.	63
Fig. 59. Porosity distribution for (■) equiatomic and (■) equimassic TNZT mechanical alloying by powder metallurgy, and (■) equiatomic and (■) equimassic TNZT mechanical alloying by powder metallurgy and casting.	64
Fig. 60. Macropore in the TNZT casting sample.	65

Fig. 61. Acid etching for (□) equiatomic and (■) equimassic TNZT mechanical alloying by powder metallurgy, and (■) equiatomic and (■) equimassic TNZT mechanical alloying by powder metallurgy and casting.	66
Fig. 62. Element mapping by FESEM for equiatomic TNZT mechanical alloying by powder metallurgy.....	67
Fig. 63. <i>Element mapping by FESEM for equimassic TNZT mechanical alloying by powder metallurgy.....</i>	68
Fig. 64. Element line scanning by FESEM for equiatomic TNZT mechanical alloying by powder metallurgy and casting.	69
Fig. 65. Element line scanning by FESEM for equimassic TNZT mechanical alloying by powder metallurgy and casting.	70
Fig. 66. (□) Equiatomic and (■) equimassic TNZT mechanical alloying by powder metallurgy, and (■) equiatomic and (■) equimassic TNZT mechanical alloying by powder metallurgy and casting XRD that shows crystallographic planes for each diffraction pick according to the distinct phases detailed.	71
Fig. 67. Band and crystallographic phase contrast by EBSD with the same magnification for (□) equiatomic and (■) equimassic TNZT mechanical alloying by powder metallurgy, and (■) equiatomic and (■) equimassic TNZT mechanical alloying by powder metallurgy and casting, where red represents BCC and yellow FCC.....	72
Fig. 68. Element mapping by TEM for equiatomic TNZT mechanical alloying by powder metallurgy.....	74
Fig. 69. Electron diffraction of a Ti-Nb-Ta-rich TNZT zone that confirms the presence of a BCC microstructure in the equiatomic TNZT mechanical alloying by powder metallurgy, [001] zone axis: (a) selected area diffraction (SAD), (b) diffraction pattern.	74
Fig. 70. Electron diffraction of a Zr-rich TNZT zone Zr that confirms the presence of a FCC microstructure in the equiatomic TNZT mechanical alloying by powder metallurgy, [215] zone axis: (a) selected area diffraction (SAD), (b) diffraction pattern.....	75
Fig. 71. Element mapping by TEM for equiatomic TNZT mechanical alloying by powder metallurgy and casting (zone 1).	75
Fig. 72. Electron diffraction of a Ti-Nb-Ta-rich TNZT zone that confirms the presence of a BCC microstructure in the equiatomic TNZT mechanical alloying by powder metallurgy and casting, [311] zone axis: (a) selected area diffraction (SAD), (b) diffraction pattern.....	76

Fig. 73. Element mapping by TEM for equiatomic TNZT mechanical alloying by powder metallurgy and casting (zone 2).	76
Fig. 74. Electron diffraction of a Zr-rich TNZT zone Zr that confirms the presence of a FCC microstructure in the equiatomic TNZT mechanical alloying by powder metallurgy and casting, [111] zone axis: (a) selected area diffraction (SAD), (b) diffraction pattern.....	77
Fig. 75. Inverse polar figures with same magnification of the crystalline orientation in the z-direction (IPF-Z) for (□) equiatomic and (■) equimassic TNZT mechanical alloying by powder metallurgy, and (□) equiatomic and (■) equimassic TNZT mechanical alloying by powder metallurgy and casting.	78
Fig. 76. Pitsch crystallographic orientation relationship for (□) equiatomic and (■) equimassic TNZT mechanical alloying by powder metallurgy and casting.	79
Fig. 77. Hardness results for (□) equiatomic and (■) equimassic TNZT mechanical alloying by powder metallurgy, and (□) equiatomic and (■) equimassic TNZT mechanical alloying by powder metallurgy and casting.	80
Fig. 78. Microhardness results for (□) equiatomic and (■) equimassic TNZT mechanical alloying by powder metallurgy, and (□) equiatomic and (■) equimassic TNZT mechanical alloying by powder metallurgy and casting.	81
Fig. 79. Elastic modulus results for (□) equiatomic and (■) equimassic TNZT mechanical alloying by powder metallurgy, and (□) equiatomic and (■) equimassic TNZT mechanical alloying by powder metallurgy and casting.	82
Fig. 80. (a) Equiatomic and (b) equimassic TNZT mechanical alloying behaviour by powder metallurgy.....	83
Fig. 81. Micro-compression tooling deformation after testing: (a) top and (b) bottom.....	84
Fig. 82. Comparison between principal test parameters for (□) equiatomic and (■) equimassic TNZT mechanical alloying by powder metallurgy: (a)elastic modulus, (b) ultimate strength, and (c) elongation.	85
Fig. 83. Small-punch results for (□) equiatomic and (■) equimassic TNZT mechanical alloying by powder metallurgy, and (□) equiatomic and (■) equimassic TNZT mechanical alloying by powder metallurgy and casting: (a) elastic slope, (b) plastic slope, (c) maximum force, and (d) first breakage. Grey lines delimited the maximum and minimum values corresponding to the elastic slope and the maximum force.	86

Fig. 84. Fractography after the 4-point bending test for (■) equiatomic and (■) equimassic TNZT mechanical alloying by powder metallurgy.	87
Fig. 85. (a) OCP graphs as a function of time and (b) potentiodynamic polarisation curves for (■) equiatomic and (■) equimassic TNZT mechanical alloying by powder metallurgy, and (■) equiatomic and (■) equimassic TNZT mechanical alloying by powder metallurgy and casting. Grey lines delimited the maximum and minimum values corresponding to the elastic slope and the maximum force.	88
Fig. 86. Nyquist plots for (■) equiatomic and (■) equimassic TNZT mechanical alloying by powder metallurgy, and (■) equiatomic and (■) equimassic TNZT mechanical alloying by powder metallurgy and casting.	89
Fig. 87. Bode plots for (a) equiatomic and (b) equimassic TNZT mechanical alloying by powder metallurgy, and (c) equiatomic and (d) equimassic TNZT mechanical alloying by powder metallurgy and casting.	90
Fig. 88. Single-layer EEC used for fitting the experimental data, where R_s represents the electrolyte resistance and RC the compact layer (Lasia, 2014).	90
Fig. 89. (a) Contact angle and (b) surface free energy results for equiatomic and equimassic TNZT mechanical alloying by powder metallurgy (EA MA PM, EM MA PM), and equiatomic and equimassic TNZT mechanical alloying by powder metallurgy and casting (EA MA C, EM MA C).	92
Fig. 90. Thermodynamic simulations of the cooling-phase diagram for equiatomic TNZT MEAs made by Thermo-Calc software AB, version 2022a and TCHEA3: High Entropy Alloy v3.1 database.	93
Fig. 91. Thermodynamic simulations of the cooling-phase diagram for equimassic TNZT MEAs by Thermo-Calc software AB, version 2022a and TCHEA3: High Entropy Alloy v3.1 database.	94
Fig. 92. Thermodynamic simulations of the C influence on the equiatomic TNZT MEAs phase diagram MEA by Thermo-Calc software AB, version 2022a and TCHEA5: High Entropy Alloy v5.0 database.	95
Fig. 93. Thermodynamic simulations of the C influence on the equimassic TNZT MEAs phase diagram by Thermo-Calc software AB, version 2022a and TCHEA5: High Entropy Alloy v5.0 database.	96
Fig. 94. Abstract presented.	112

LIST OF TABLES

Table 1. Classification of alloys based on mixing entropy (Miracle & Senkov, 2017).	2
Table 2. Biological impact (Biesiekierski, Wang, Gepreel & Cuie, 2012).	4
Table 3. List of tasks corresponding to each phase of the project working plan.....	13
Table 4. Powder characteristics provided by the suppliers Atlantic Equipment Engineers and Alfa Aesar.	15
Table 5. Chemical analysis of elemental powders supplied by Atlantic Equipment Engineers and Alfa Aesar.....	16
Table 6. Particle sizes of Ti, Nb, Zr, and Ta for percentiles 10, 50, and 90.....	19
Table 7. Main characteristics of the elements Ti, Nb, Zr and Ta and their weight and atomic percentages for each type of alloy, equiatomic or equimassic.	21
Table 8. Elementary mixture powder preparation for each type of alloy, equiatomic or equimassic TNZT MEAs.	21
Table 9. Alloying powder obtention after MA.	23
Table 10. Grain formation process during sintering caption.	26
Table 11. Melting temperatures of the different elements that compose TNZT alloys.....	27
Table 12. Grain formation process during casting caption.....	28
Table 13. Extinction rules for crystallographic planes according to cell type.	38
Table 14. Distilled water and diiodomethane surface tension properties.....	55
Table 15. TNZT MEAs legend.....	56
Table 16. Compositional analysis of the equiatomic TNZT mechanically alloyed powder from the spectra illustrated in Fig. 52 (a) and the mappings of Fig. 52 (a) and (b).	58
Table 17. Compositional analysis of the equimassic TNZT mechanically alloyed powder from the mapping of Fig. 52 (c) and the spectrum illustrated in Fig. 52 (d).....	58
Table 18. TNZT samples shrinkage after sintering for equiatomic and equimassic mechanical alloying by powder metallurgy.	60
Table 19. Comparison between equiatomic and equimassic TNZT mechanical alloying samples density before and after sintering.	61
Table 20. Open, closed, and total porosity (P_{OP} , P_{CL} , P_T) corresponding to equiatomic and equimassic TNZT mechanical alloying samples by powder metallurgy (EA MA PM, EM MA PM).....	63

Table 21. Relative density and relative porosity comparison between equiatomic and equimassic TNZT mechanical alloying by powder metallurgy (EA MA PM, EM MA PM), and equiatomic and equimassic TNZT mechanical alloying by powder metallurgy and casting (EA MA C, EM MA C).....	64
Table 22. Analysis of the overall composition and light and dark areas of the element mapping by FESEM for equiatomic TNZT mechanical alloying sample by powder metallurgy.....	67
Table 23. Analysis of the overall composition and light and dark areas of the element mapping by FESEM for equimassic TNZT mechanical alloy sample by powder metallurgy.	68
Table 24. Analysis of the overall composition and light and dark areas of the element line scanning by FESEM for equiatomic TNZT mechanical alloying by powder metallurgy and casting.....	69
Table 25. Analysis of the overall composition and light and dark areas of the element line scanning by FESEM for equimassic TNZT mechanical alloying by powder metallurgy and casting.....	70
Table 26. TNZT MEAs grain size values corresponding to equiatomic and equimassic TNZT mechanical alloying by powder metallurgy, and equiatomic and equimassic TNZT mechanical alloying by powder metallurgy and casting.	73
Table 27. TNZT MEAs comparison of the microstructure type percentage for XRD and EBSD for equiatomic and equimassic TNZT mechanical alloying by powder metallurgy, and equiatomic and equimassic TNZT mechanical alloying by powder metallurgy and casting...	73
Table 28. Pitsch crystallographic orientation relationship (OR).	78
Table 29. Tests for TNZT MEA mechanical characterisation: (a) hardness, (b) microhardness, (c) determination of elastic modulus by ultrasounds, (d) 4-point bending, (e) micro-tensile (f) micro-compression, and (g) small punch. Specifically, for equiatomic and equimassic mechanical alloying by powder metallurgy (EA MA PM, EM MA PM), and equiatomic and equimassic mechanical alloying by powder metallurgy and casting (EA MA C, EM MA C).	79
Table 30. Hardness results for equiatomic and equimassic TNZT mechanical alloying by powder metallurgy (EA MA PM, EM MA PM), and equiatomic and equimassic TNZT mechanical alloying by powder metallurgy and casting (EA MA C, EM MA C).....	80

Table 31. Microhardness results for equiatomic and equimassic TNZT mechanical alloying by powder metallurgy (EA MA PM, EM MA PM), and equiatomic and equimassic TNZT mechanical alloying by powder metallurgy and casting (EA MA C, EM MA C).....	81
Table 32. Elastic modulus of TNZT MEA for equiatomic and equimassic mechanical alloying by powder metallurgy (EA MA PM, EM MA PM), and equiatomic and equimassic mechanical alloying by powder metallurgy and casting (EA MA C, EM MA C).....	82
Table 33. 4-Point bending test results for equiatomic and equimassic TNZT mechanical alloying by powder metallurgy (EA MA PM, EM MA PM).....	83
Table 34. Micro-tensile test results for equiatomic and equimassic TNZT mechanical alloying by powder metallurgy (EA MA PM, EM MA PM).....	83
Table 35. Micro-compression test results for equiatomic and equimassic TNZT mechanical alloying by powder metallurgy (EA MA PM, EM MA PM).....	84
Table 36. Small punch results for equiatomic and equimassic TNZT mechanical alloying by powder metallurgy (EA MA PM, EM MA PM), and equiatomic and equimassic TNZT mechanical alloying by powder metallurgy and casting (EA MA C, EM MA C).....	86
Table 37. Corrosion parameters for equiatomic and equimassic TNZT mechanical alloying by powder metallurgy (EA MA PM, EM MA PM), and equiatomic and equimassic TNZT mechanical alloying by powder metallurgy and casting (EA MA C, EM MA C).....	88
Table 38. Passive layer parameters for equiatomic and equimassic TNZT mechanical alloying by powder metallurgy (EA MA PM, EM MA PM), and equiatomic and equimassic TNZT mechanical alloying by powder metallurgy and casting (EA MA C, EM MA C).....	89
Table 39. EEC parameters theoretical approach to the experimental behaviour of the equiatomic and equimassic TNZT mechanical alloying by powder metallurgy (EA MA PM, EM MA PM), and equiatomic and equimassic TNZT mechanical alloying by powder metallurgy and casting (EA MA C, EM MA C).....	91
Table 40. Wettability parameters and surface energy for equiatomic and equimassic TNZT mechanical alloying by powder metallurgy (EA MA PM, EM MA PM), and equiatomic and equimassic TNZT mechanical alloying by powder metallurgy and casting (EA MA C, EM MA C).....	91
Table 41. Compositional analysis to the thermodynamic simulated stable phases for equiatomic TNZT MEAs shown in Fig. 92.....	97

Table 42. Compositional analysis to the thermodynamic simulated stable phases for equimassic TNZT MEAs shown in Fig. 93.....	98
Table 43. Hardness properties comparison between TNZT MEAs and Ti-6Al-4V, 316 SS, and Stellite 6 (Yeh et al., 2004).....	100
Table 44. Intrinsic elastic modulus comparison between TNZT MEAs and Ti-6Al-4V, 316L SS, Co-Cr-Mo (Semlitsch & Willert, 1980), CP-Ti (grade 4) (Li, 2000), Ti-35Nb-5Ta-7Zr (Narayan, 2012), and bone (Castro, Jaeger, Baptista, & Oliveira, 2021).	101
Table 45. Kinetic corrosion parameters for CP-Ti and Ti-6Al-4V (Rossi, Ventura, Milián, Escuder, & Amigó Borrás, 2022).....	102

1. INTRODUCTION

1.1. BACKGROUND

High-entropy alloys (HEAs) have been studied since relatively little time, starting in 2004. In contrast to conventional alloys with a matrix of one main element to which precipitates of other elements are added to improve their properties (Yeh et al., 2004). HEAs are characterised by containing at least five main elements with an atomic concentration of 5 - 35 %. This results in a stable solid solution instead of a formation of intermetallic compounds or segregated states (**Fig. 1**). However, in the case of refractory materials, it is enough to contain four instead of five different elements. It is referred to as medium-entropy alloys (Castro, Jaeger, Baptista & Oliveira, 2021).

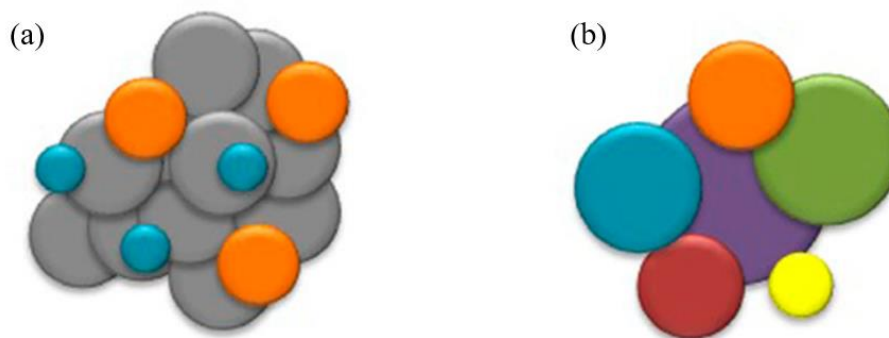


Fig. 1. Alloying philosophy in (a) conventional metallurgy and (b) HEAs (Torralba & García-Junceda, 2019).

On the other hand, HEAs can be described by four core effects, the high entropy effect, the lattice distortion effect, sluggish diffusion, and the cocktail effect (Miracle & Senkov, 2017).

i. *High entropy effect.*

The high entropy term reflects through the mixing entropy the stability of the disordered solution relative to the perfectly ordered intermetallic compound. Considering this mixing entropy for ideal configurations, $\Delta S_{\text{mix}} = -R \cdot \sum (x_i \cdot \ln(x_i)) = -R \cdot \ln(n)$, where 'n' refers to the

concentration of mixing elements in equiatomic proportion and ‘R’ to the Boltzmann constant (Sharma, Dwivedi & Dwivedi, 2021). Previous experimental results have shown that the higher entropy of mixing, the lower number of phases. Consequently, an increase in the ease of formation of the aforementioned solid solution is resulted (Tsai & Yeh, 2014). The classification of alloys according to their entropy is shown in **Table 1**.

Table 1. Classification of alloys based on mixing entropy (Miracle & Senkov, 2017).

Classification	Mixing entropy
High-entropy alloys	$1.61 \cdot R \leq \Delta S_{\text{mix}}$
Medium-entropy alloys	$0.69 \cdot R \leq \Delta S_{\text{mix}} \leq 1.61 \cdot R$
Low-entropy alloys	$\Delta S_{\text{mix}} \leq 0.69 \cdot R$

ii. *Lattice distortion effect.*

Considering that there are different atomic sizes due to the several elements that make up this type of alloy, there is a higher distortion of the crystallographic lattice than in conventional alloys. This results in a high solution hardening effect associated with improved properties such as strength and hardness and a low-temperature dependence of these ones.

iii. *Sluggish diffusion.*

This effect states that the number of elements in the alloy matrix is proportional to the degree of the diffusion rate. Thus, sluggish diffusion leads to slower grain growth and particle coarsening (Castro, Jaeger, Baptista & Oliveira, 2021) than conventional alloys.

iv. *The cocktail effect.*

Finally, the properties of HEAs are in some way related to those of their constituent elements. Nevertheless, their properties are also influenced by the interatomic relationships between the elements.

Then again, the literature offers hundreds of different compositions that can be divided into four families. These are 3d transition metals, lightweight material, lanthanide, and refractory (Torralba & García-Junceda, 2019).

Specifically, refractory HEAs show promising properties such as ultrahigh strength at room temperature, significant resistance to softening at elevated temperatures, and excellent corrosion resistance. High-melting-point metals include Hf, Ta, Nb, Zr, Ti, V, W, Mo, and Cr (Nguyen et al., 2020).

Thus, the breakthroughs in this field have led to several potential applications as refractory, structural, functional, and biomedical (Castro, Jaeger, Baptista & Oliveira, 2021). Of the high-melting-point elements specified above, Ti, Ta, Zr, and Nb are the premier biocompatible metals for load-bearing bone-implant applications, as well as for other structural applications, including those at elevated temperatures (Nguyen et al., 2020). This biological impact can be seen in **Table 2**, where red indicates serious concern, yellow indicates moderate concern, and green shows minimal or no concern.

Titanium and its alloys are widely used in many fields thanks to their excellent corrosion resistance, biocompatibility, and high mechanical properties. Despite these brilliant properties, other ones, like wear resistance, are not good enough for biomedical devices (Jakubowicz, 2020). Some applications are the conformability of Ti-16Nb porous scaffolds as studied by Yilmaz et al. (2018) or the development of shape memory Ni-free β -type Ti-Nb alloys with shape memory, reported by Nagoshi et al. (2020). After all, the outstanding alloy in the biomedical field is Ti-6Al-4V.

Table 2. *Biological impact (Biesiekierski, Wang, Gepreel & Cuie, 2012).*

Element	Biocompatible	Carcinogenic	Genotoxic	Mutagenic	Cytotoxic	Allergenic	Prone to corrosion	Other (*)
Ti	Yes	No	No	No	Med	No	No	No
V	No	Yes	Yes	Yes	High	Disputed	No	No
Cr	No	Disputed	Yes	Yes	High	Yes	No	No
Mn	No	No	Yes	No	High	No	Yes	No
Fe	No	No	Yes	Disputed	Med	No	Yes	No
Co	No	Yes	Yes	Yes	High	Yes	Yes	Yes
Ni	No	Yes	Yes	Yes	High	Yes	Yes	Yes
Cu	No	No	Yes	Yes	High	Yes	Yes	Yes
Zr	Yes	No	No	No	Low	No	No	No
Nb	Yes	No	No	No	Low	No	No	No
Mo	No	Disputed	Yes	Yes	Low	Yes	Yes	Yes
Tc	No - Radioactive -							
Ru	Yes	No	No	No	Med	No	No	Yes
Rh	No	Yes	Yes	Yes	High	Unknown	No	No
Pd	No	Yes	No	Disputed	Med	Yes	No	No
Ag	No	No	No	No	High	Yes	No	Yes
Hf	Unknown	Unknown	Unknown	Unknown	Med	No	No	Unknown
Ta	Yes	No	No	No	Low	No	No	No
W	No	Yes	Yes	No	Med	No	Yes	No
Re	Unknown	Unknown	Unknown	Unknown	Unknown	No	No	Unknown
Os	No	Unknown	Yes	Yes	High	No	Yes	No
Ir	No	No	No	Yes	High	No	No	Yes
Pt	No	Yes	Yes	Yes	High	Yes	No	No
Au	Yes	No	No	No	High	No	No	No
Al	No	No	Yes	No	Low	No	No	Yes
Zn	No	No	No	No	High	No	No	Yes
Sn	Yes	No	No	No	Low	No	No	Yes

(*) Other: Refers to issues beyond those already listed. For example, haemolysis, and neurological effects, among others.

On the other hand, niobium offers great potential in this biomedical field because of its excellent corrosion resistance. Nevertheless, its mechanical properties are quite poor. Despite all of them, its first significant clinical application, reported by Beier et al. (2006), is the use of standard Nb-15Zr for cardiovascular devices such as stents. Another use of this element is a technique where its deposition is applied to the surface of non-biocompatible materials. The aim is to create an attractive surface for implant acceptance (O'Brien, 2015).

Zirconium and its alloys exhibit excellent biocompatibility, good corrosion behaviour, and favourable mechanical properties. Specifically, these alloys are suitable for applications in orthopaedic and dentistry owing to their low Young's modulus. Despite being similar to Ti alloys, they have had little attention as biomaterials (Kiyoshi et al., 2020). Nowadays, Ti-Zr alloys have recently started to receive attention as promising materials for dental applications. In addition, Medvedev et al. (2016) suggest that the Ti-15Zr alloy is a promising candidate to replace CP-Ti. Furthermore, Slokar et al. (2012) studied about Ti-Nb-Zr alloys concluding their great use as biomaterials.

Finally, tantalum is a highly biocompatible, corrosion-resistant, and tough metal. Being physiologically inert, among many applications, it can be used to manufacture surgical instruments and implants. In this field, its osteointegration and osteoconductive capacity acquire high importance. Thus, it is used to manufacture implants that trigger the biological fixation between the prosthesis and the bone. After some experimental essays, results confirmed the expected corrosion resistance and biocompatibility of the studied Ti-Ta alloys, being even better than pure Ti or Ti-6Al-4V (Long, Niinomi, Akahori, Fukui & Toda, 2005).

Along with the developed alloys mentioned above, different chemical compositions have been studied to evaluate the properties obtained with each one. Likewise, several researchers have focused their studies on different Ti-Nb-Ta-Zr (TNZT) alloys, such as Ti-4Nb-15Zr-4Ta (Okazaki, 2001), Ti-5Nb-10Zr-5Ta (Raducanu et al., 2011), Ti-21Nb-6Zr-15Ta, Ti-25Nb-10Zr-8Ta (Carmen, Kamel & Carmen-Iulia, 2014), Ti-35Nb-7Zr-5Ta (Lario, Escuder, Segovia & Amigó, 2022) or Ti-29Nb-4.6Zr-13Ta (Niinomi M., 2003), among others, with different chemical composition and obtention methods. In this respect, casting is the most

popular way of obtaining samples. Nevertheless, the drawbacks of the process make powder metallurgy a reliable alternative.

These drawbacks are referred to the molten material's high reactivity and the difficulty associated with the differences between the melting points of the elements. This difference may alter the intended homogeneity. To avoid this and to achieve chemical homogeneity, samples are remelted six times. Melting, by contrast, offers a fast-manufacturing process.

Powder metallurgy, likewise, has both advantages and disadvantages. The latter are the lack of diffusion of alloying elements, the difficulty of grain size control, and the appearance of remaining porosity. In contrast, many advantages can be offered, such as the ability to alloy large quantities of alloying elements or the absence of anisotropy. All this by means of a relatively simple process.

Titanium has two allotropic forms, HCP and BCC. This transformation from the HCP structure, known as α , to the BCC, known as β , occurs at 882.5 °C. The addition of alloying elements changes the transformation temperature and, depending on the number of alloying elements, the microstructure of the alloys is classified as α , $\alpha + \beta$, and β , as shown in **Fig. 2**.

Some elements tend to stabilise a specific structure. Both Nb and, to a lesser extent, Ta act as β -stabilizers to form homogeneous solid solutions, while Zr acts as a neutral element forming a homogeneous solid solution in the α - and β -phases. Furthermore, Nb and Ta reduce the elastic modulus when alloyed with titanium in specific preferred quantities (Elias, Schneider, Schneider, Silva & Malvisi, 2008).

Finally, Nguyen et al., (2018) conducted a research focused on the evaluation of microstructural and mechanical behaviour of the quaternary equiatomic TNZT obtained via arc melting. With it, it was concluded that the alloy showed an excellent combination of mechanical properties as well as a significant reduction of the elastic modulus compared to its starting alloy Ti-Nb-Zr-Ta-Mo. However, it is comparable to that of the Ti-6Al-4V alloy.

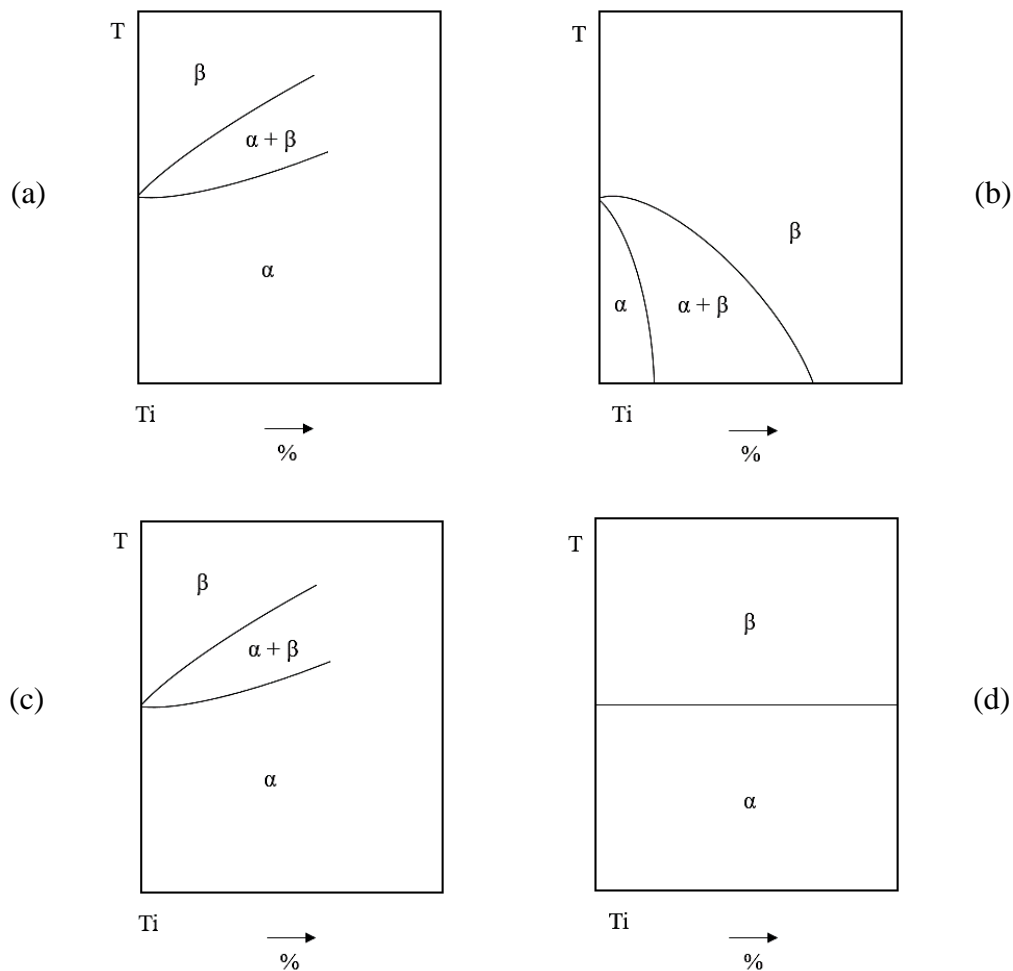


Fig. 2. Titanium binary phase diagram: (a) α -stabiliser, (b) isomorphous β -stabiliser, (c) eutectoid β -stabiliser, and (d) neutral.

1.2. MOTIVATION

So far, advances in this field have mainly been made in alloys with a high iron, cobalt, or nickel content (**Fig. 3**). This has led to different applications of these materials as structural materials, mainly used in the aeronautical sector or biomaterials, among others.

About the latter sector, some conventional materials, such as titanium alloys, cobalt-chromium, or stainless steels, are characterised by their good mechanical and corrosion properties. In biomedical applications, however, they have significant disadvantages. The first is that due to tribo-corrosion, particles are released. Thus, allergic reactions and diseases such as cancer or Alzheimer's disease can be caused. The second one is that the elastic modulus of

these materials is much higher than that of bone. Consequently, a stress-shielding effect can lead to osteoporosis and long-term problems such as implant loosening (Yang, Liu, Pang, Liaw & Zhang, 2020).

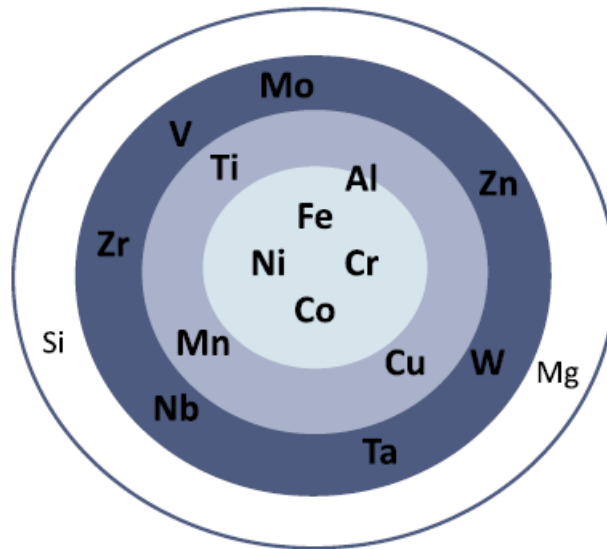


Fig. 3. Main alloying elements in the HEAs studied (Torralba & García-Junceda, 2019).

In contrast, the rise of High and Medium-entropy alloys is due to the fact that they generally provide good mechanical, physical and chemical properties. Moreover, they afford a combination of interesting properties, such as high resistance to fatigue, corrosion, and wear, as well as improved mechanical behaviour at high temperatures.

Nevertheless, in the biomedical sector, it is necessary not only to use refractory elements that allow improving these behaviours at high temperatures but also to search for greater compatibility. Together with the increase in life expectancy, this makes it necessary to develop alloys with more demanding capabilities since the average implant longevity is estimated to last between 12 and 15 years. This longevity, in turn, means that patients under 65 will need at least one surgical revision (Li et al., 2014).

Population ageing, produced by the development of the economy and technology, increases the risk of hard tissue failure. Metallic implants solve the need for hard tissue replacement in

most cases (70 ÷ 80%) (Li et al., 2014). This evolution is shown in **Fig. 4** for hip cases in particular.

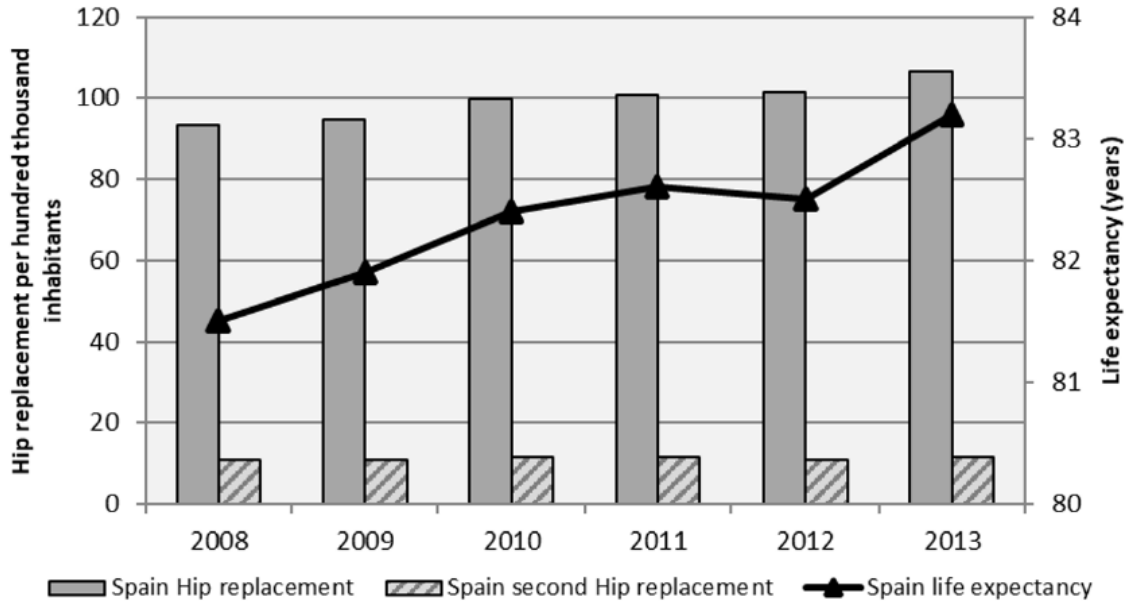


Fig. 4. Hip replacement per one hundred thousand inhabitants' evolution (Lario, Poler & Amigó, 2022).

Concerning this aspect, the impact on biocompatibility and long-term implant performance is directly related to the microstructure obtained during alloy consolidation and surface treatments. Both factors modulate implant corrosion resistance, ion release, cell differentiation and cytotoxicity (Lario, Amigó, Vicente & Segovia, 2016).

All those reasons are why this project has committed to the selection of 4 refractory elements that present greater biocompatibility, such as zirconium, titanium, niobium, and tantalum, in that order.

This work aims to propose solutions for some of the abovementioned problems in current implant biomaterials.

1.3. OBJECTIVES

The main objective of the present work is the mechanical and structural characterisation of the quaternary titanium alloy TNZT starting from its consolidation, sintering and subsequent

casting. Both in its equiatomic and equimassic composition because these are the most general starting compositions for an alloy of this type. This is because this form is considered the best way to access a new alloy.

Consequently, the specific objectives to be achieved with the development of this project are the following:

- Exploration of different sample collection routes to evaluate the influence of the conventional powder metallurgy, which has been little used so far for the obtention of this type of alloys.
- Atomic diffusion analysis through the microstructure.
- Evaluation of the suitability of the obtention process.
- Study the compactness and shrinkage of the alloys during the sintering process.
- Porosity measurements.
- Analysis of the number of phases, its crystallographic microstructure, and composition.
- Grain size and crystallographic orientation analyses.
- Determination of the elastic modulus, hardness, microhardness, and strength.
- Evaluation of the corrosion resistance and wettability.

To achieve the proposed objectives, the following operational objectives are proposed:

- Alloy's obtention by mechanical alloying of powders and evaluate the feasibility of two obtaining routes: casting and powder metallurgy by press and sintering.
- Analysis of the starting powder as well as the alloying one after carrying out the mechanical alloying in the planetary mill.
- Determination of the geometry of the samples before and after the sintering process in the high vacuum furnace.
- Casting of some samples obtained previously by powder metallurgy.
- Carrying out Arquimedes' tests and optical microscopy to compare the porosity results using both techniques. At the same time, determination of the number of phases of the alloys by the optic microscope.

- Performance of electron microscopy techniques.
- Analysis of the alloys by X-Ray Diffraction.
- Carrying out different tests to allow the mechanical characterisation of these alloys.
- Performance of some tests to characterise the service properties of these alloys.

2. WORKING PLAN

This research project has been divided into 4 distinct phases that can be broken down into several tasks to achieve the project's objectives (**Table 3**). Phase 1 consists of obtaining the samples by mixing the raw material, which is mechanically alloyed and then compacted and sintered, what makes them resilient. However, throughout this phase, numerous analyses are executed to characterise both the raw material and the alloyed powders gotten. This way, it allows the evaluation of the process carried out. Finally, different pieces are melted after fracturing the samples obtained by press and sintering in one of the mechanical tests. Thus, the casting samples are obtained, what gives different alloys to be assessed:

- Equiatomic mechanical alloying by powder metallurgy
- Equimassic mechanical alloying by powder metallurgy
- Equiatomic mechanical alloying by powder metallurgy + casting
- Equimassic mechanical alloying by powder metallurgy + casting

On the other hand, Phase 2 groups together those tasks related to the use of techniques that allow microstructural characterisation. Some characteristics can be determined as the quantity and distribution of the phases, as well as their chemical composition, crystalline structure, or grain size, among other aspects. This requires the use of different high-tech equipment. In addition, it is necessary to carry out a perfect preparation of the samples in order to obtain suitable results. Thus, this phase requires X-Ray Diffraction, metallographic preparation of the samples, optical and electronic microscopy, as Field - Emission Scanning Electron Microscopy, Electron Backscatter Diffraction or Transmission Electron Microscopy.

In Phase 3, different tests and analyses are carried out to characterise the mechanical behaviour of the samples, as well as to determine other physical characteristics. This mechanical characterisation turns out of vital importance in assessing the applicability of the alloys. Consequently, in order to carry out many of the tests proposed, it is necessary to

process the samples obtained by milling and cutting operations. This is due to the fact that it is required to adapt their handling to the equipment. Thus, the tests included in this phase are Archimedes, determination of elastic modulus by ultrasounds, hardness, micro-hardness, 4-point bending, tensile, compression and small punch.

Finally, Phase 4 involves chemical characterisation, where the service properties of the alloys are evaluated by performing electrochemical corrosion and contact angle tests. Concerning the latter, it is possible to analyse the wettability of the alloys and their surface energy.

Table 3. List of tasks corresponding to each phase of the project working plan.

PHASE 1.	Sample obtention
1.1.	Powder mixing
1.2.	Mechanical alloying
1.3.	Compaction
1.4.	Sintering
1.5.	As cast
PHASE 2.	Microstructural characterisation
2.1.	X-Ray Diffraction
2.2.	Metallographic preparation
2.3.	Optical Microscopy
2.4.	Field - Emission Scanning Electron Microscopy
2.5.	Electron Backscatter Diffraction
2.6.	Transmission Electron Microscopy
PHASE 3.	Mechanical characterisation
3.1.	Archimedes test
3.2.	Determination of elastic modulus by ultrasounds

- 3.3. Hardness test
- 3.4. Microhardness test
- 3.5. 4-Point bending test
- 3.6. Tensile test
- 3.7. Compression test
- 3.8. Small punch

PHASE 4. Chemical characterisation

- 4.1. Electrochemical corrosion
 - 4.2. Wettability and contact angle
-

3. MATERIALS AND METHODS

This section details the materials used throughout the project and the methodology followed in carrying out the different tests to achieve the previously defined objectives.

This work has been carried out at the Instituto de Tecnología de Materiales (ITM), with the collaboration of the Servicio de Microscopía Electrónica, both belonging to the Universitat Politècnica de València (UPV).

3.1. SAMPLE COLLECTION

The raw materials have been used in the form of high-purity powders. These have been provided by the suppliers Atlantic Equipment Engineers and Alfa Aesar, who produce Ti and Nb, and Ta and ZrH₂, respectively.

The material suppliers also provide a physicochemical analysis of the products, indicating the degree of purity, average particle size, and crystalline structure. For all 4 types of materials used, these characteristics are detailed in **Table 4**, while the compositions of the powders supplied are given in **Table 5**. It should be noted that in order to improve diffusion, raw materials with a particle size below 50 microns have been sought.

Table 4. Powder characteristics provided by the suppliers Atlantic Equipment Engineers and Alfa Aesar.

Raw material	Purity (%)	Average particle size (µm)	Crystalline structure
Ti	99.9	44	Hexagonal
Nb	99.8	1 - 5	BCC
ZrH ₂	99.9	4.5 - 6.5	FCC
Ta	99.9	1 - 5	BCC

Table 5. Chemical analysis of elemental powders supplied by Atlantic Equipment Engineers and Alfa Aesar.

Ti chemical analysis (%)		Nb chemical analysis (%)		ZrH ₂ chemical analysis (%)		Ta chemical analysis (%)	
O	0.2290	Mo	0.0200	Ca	< 0.0100	H	0.0200
N	0.0160	Al	0.0300	Fe	< 0.0800	N	0.0060
H	0.0222	Zn	0.0200	Hf	< 0.0100	Si	0.0020
Fe	0.0100	Si	0.0200	ZrH ₂	99.9000	W	0.0030
Si	< 0.0100	Mn	0.0400	-	-	Al	0.0005
Al	< 0.0100	Cu	0.0200	-	-	K	0.0015
S	< 0.0010	Mg	0.0100	-	-	C	0.0070
C	0.0180	Ni	0.0100	-	-	Nb	0.0020
Mg	0.0100	O	0.0200	-	-	Ni	0.0010
Mn	0.0100	Nb	99.8000	-	-	Ti	0.0005
Na	< 0.0100	-	-	-	-	Mn	0.0005
Cl	< 0.0100	-	-	-	-	Mo	0.0005
P	< 0.0020	-	-	-	-	O	0.3500
Ti	99.9000	-	-	-	-	Fe	0.0040
-	-	-	-	-	-	Cr	0.0015
-	-	-	-	-	-	Na	0.0015
-	-	-	-	-	-	Ca	0.0010
-	-	-	-	-	-	Ta	99.9000

Since the morphology and size of the powders are influential factors in the production of powder metallurgy alloys, these parameters are additionally analysed before the development of the alloys.

Morphology has been evaluated by scanning electron microscopy using secondary electron images, shown in **Fig. 5**. There, a percentage of fine particles can be shown in all cases. Ti and Nb powder have an irregular morphology with different particle sizes ranging from less than 10 microns to just over 75 microns. Whereas in the case of ZrH₂ and Ta, agglomerations are less than 10 microns in size with irregular morphology.

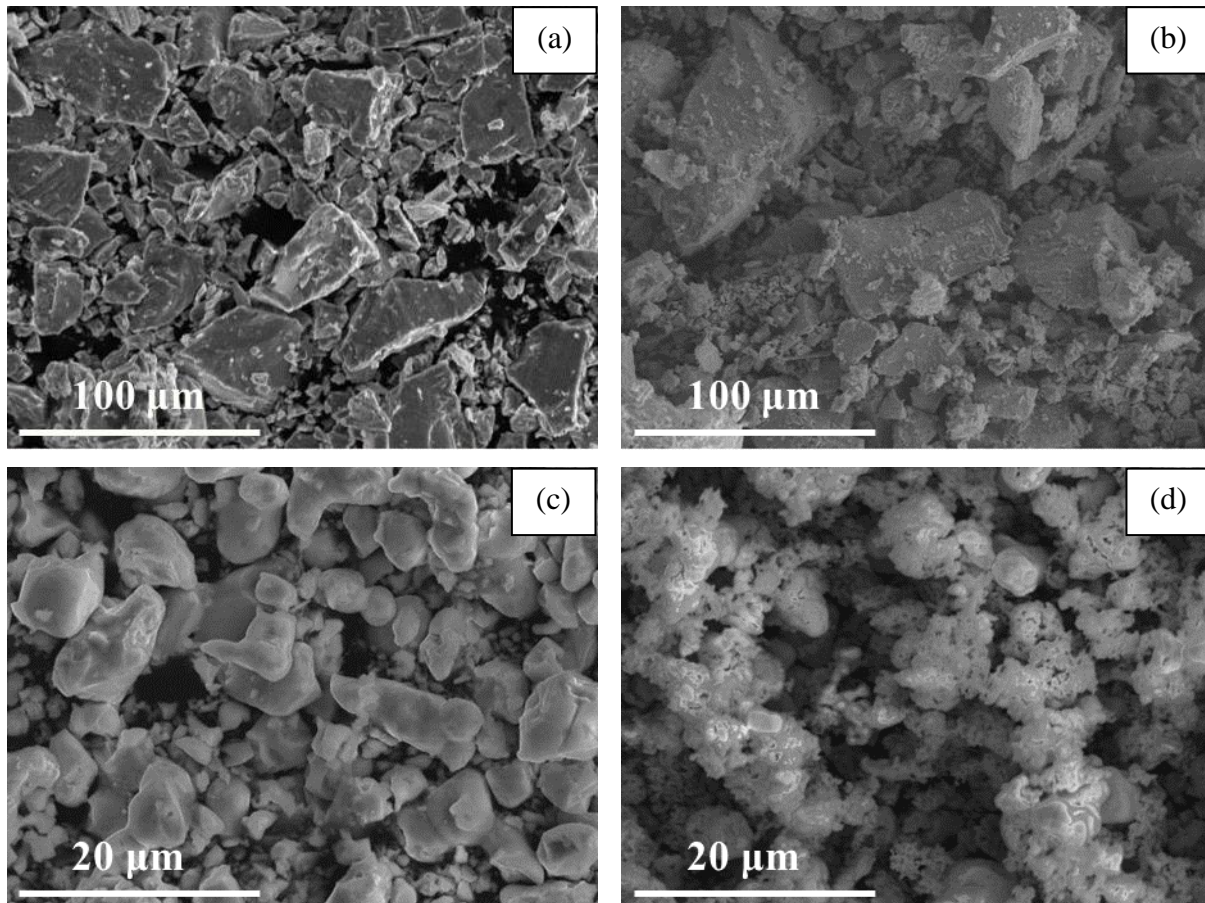


Fig. 5. (a) Ti, (b) Nb, (c) Zr hydride, and (d) Ta powder secondary electron images.

On the other hand, the granulometry is obtained using a Mastersizer 2000 laser diffraction equipment. In **Fig. 6**, results show, in line with the morphological results, that Ti powder has a higher concentration of particles smaller than 30 microns. This is approximately 33% lower than the size marked in the supplier's specifications, what indicates that the powder morphology is not equiaxial.

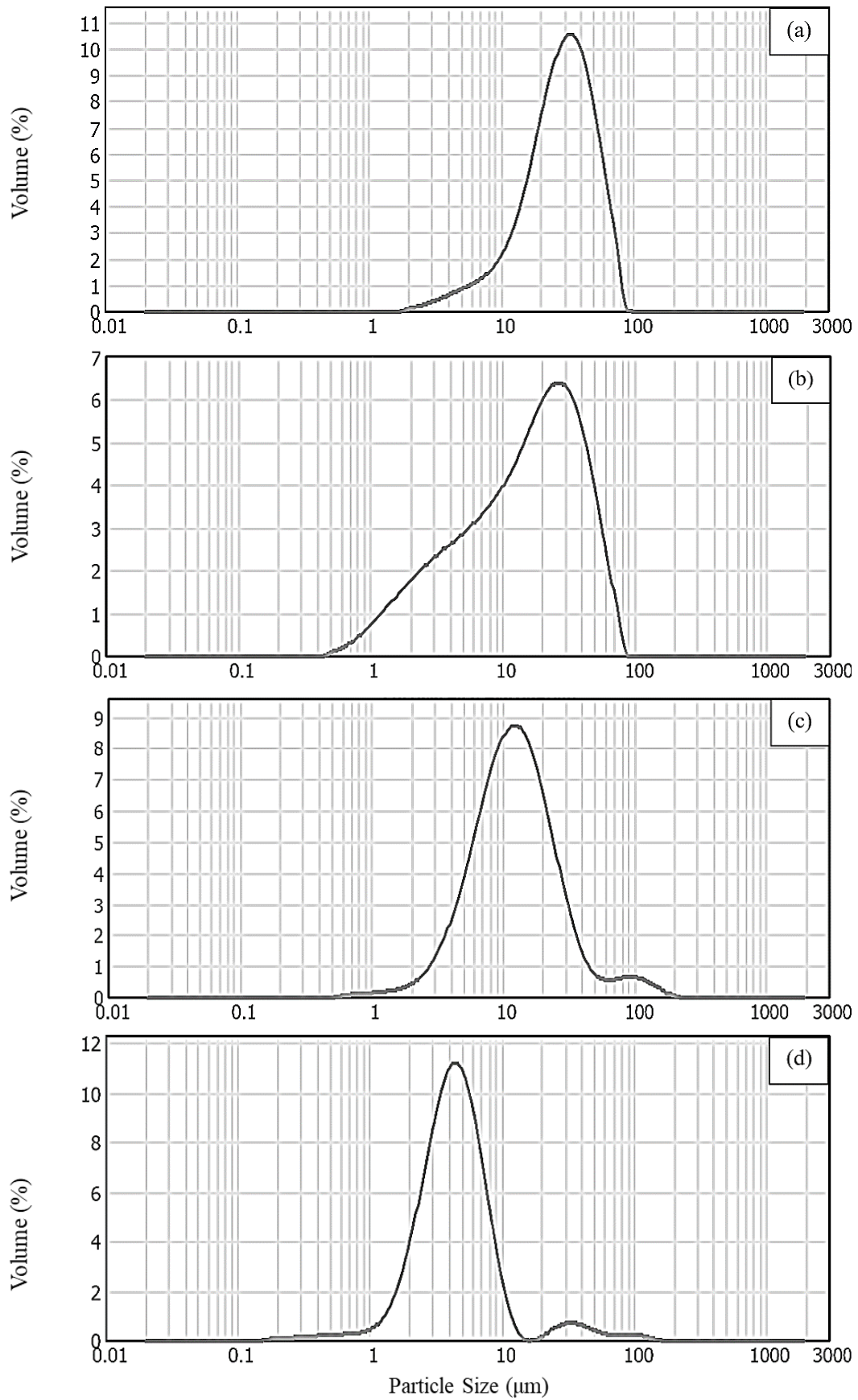


Fig. 6. (a) Ti, (b) Nb, (c) Zr hydride, and (d) Ta powder particle size distribution.

In contrast, Nb and ZrH₂ powders have a larger effective size than expected due to the agglomeration of different particles, which may hinder the diffusion of these elements. Finally, from the Ta powder distribution, it can be seen that the average particle size does correspond to the supplier's specifications.

Table 6. Particle sizes of Ti, Nb, Zr, and Ta for percentiles 10, 50, and 90.

Raw material	P ₁₀ particle size (μm)	P ₅₀ particle size (μm)	P ₉₀ particle size (μm)
Ti	11.064	29.227	55.929
Nb	2.529	15.942	45.002
ZrH ₂	4.757	12.074	30.436
Ta	2.057	4.326	8.791

To conclude the analysis of the raw materials, XRD of each powder type was carried out, obtaining the diffractogram shown in **Fig. 7**.

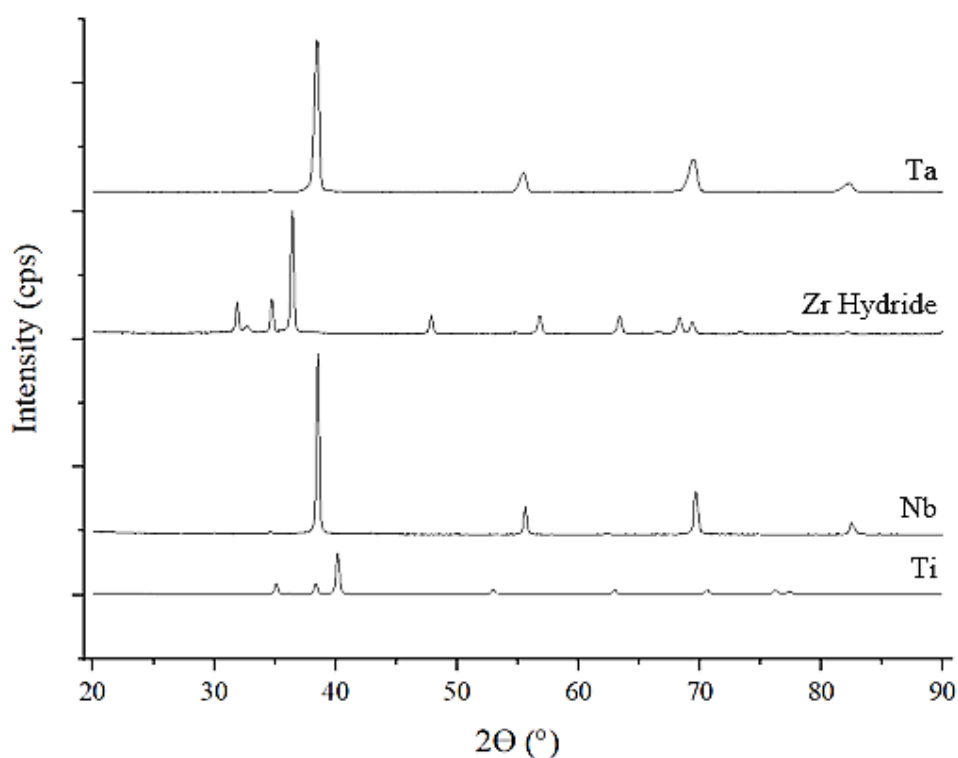


Fig. 7. XRD of Ti, Nb, Zr, and Ta powders used as raw materials.

Then, the manufacturing route followed (**Fig. 8**) starts with the elemental mixing of powders and their subsequent alloying in a planetary mill for a total of 40 hours, namely in work cycles of 8 minutes on and 10 minutes off. After, they are compacted at a pressure of 1,000 MPa and sintered in a high vacuum furnace at a temperature of 800 and 1,400 °C for 1 and 3 hours, respectively. Finally, electric arc casting is carried out on some of the samples obtained, as detailed above in the working plan.

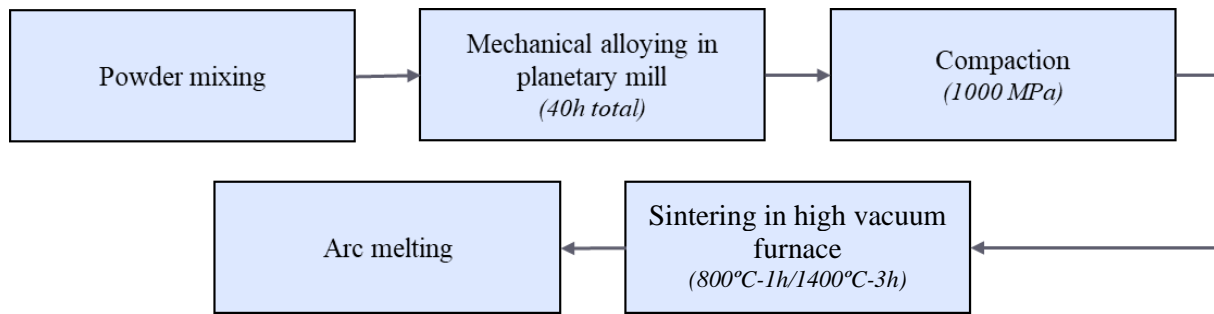


Fig. 8. Sample collection route followed to obtain TNZT MEAs.

3.1.1. Conventional powder metallurgy

Preceding the elemental mixing of powders, it is necessary to calculate the mass of each element to form the TNZT alloys in their equiatomic and equimassic form. To do this, the density of the different elements that make up the alloy and that of the alloy itself may be considered. Following **Equation 1**, ρ_{TNZT} represents the density of the mixture, ρ_i the density of each element, and $\%w_i$ the percentage by weight of the elements (**Table 7**).

$$\rho_{\text{TNZT}}[\text{g/cm}^3] = \frac{100}{\frac{\%w_{\text{Ti}}}{\rho_{\text{Ti}}[\text{g/cm}^3]} + \frac{\%w_{\text{Nb}}}{\rho_{\text{Nb}}[\text{g/cm}^3]} + \frac{\%w_{\text{Zr}}}{\rho_{\text{Zr}}[\text{g/cm}^3]} + \frac{\%w_{\text{Ta}}}{\rho_{\text{Ta}}[\text{g/cm}^3]}} \quad \text{Equation 1.}$$

It should be noted that, in the case of Zr, despite the use of ZrH_2 , the characteristics of the element have been respected since the hydride evaporates at high temperatures, namely during sintering.

Table 7. Main characteristics of the elements Ti, Nb, Zr and Ta and their weight and atomic percentages for each type of alloy, equiatomic or equimassic.

Raw material	Atomic radius (pm)	Atomic weight (u)	Density (g/cm ³)	Equiatomic mixing		Equimassic mixing	
				Wt. %	At. %	Wt. %	At. %
Ti	140	47.867	4.507	11.59	25.00	25.00	43.39
Nb	145	92.906	8.570	22.50	25.00	25.00	22.36
Zr	155	91.224	6.505	22.09	25.00	25.00	22.77
Ta	145	180.947	16.670	43.82	25.00	25.00	11.48

As seen in **Table 8**, the amount of each element used has varied very slightly according to the calculations, causing a modification of the theoretical density. However, it can be assumed that this difference is negligible for both alloys.

Table 8. Elementary mixture powder preparation for each type of alloy, equiatomic or equimassic TNZT MEAs.

Alloy	Sample	Theoretical mixing density (g/cm ³)	Sample mass (g)	Number of samples	Mass of mixture (g)	Final mass (g)	Final mixing density (g/cm ³)
Equiatomic TNZT	1644	8.911	14.437	4	57.746	57.754	8.923
	1645						
	1646						
	1647						
Equimassic TNZT	1648	7.243	11.733	4	46.933	58.652	7.245
	1649						
	1650						
	1651						

The high reactivity of some elements used makes it indispensable to work in controlled atmospheres or vacuum conditions. This is why mixing the elements in the determined quantities is carried out using the glove box of the Jacomex manufacturer, model GP Campus (**Fig. 9**). It is made up of a pressure regulator and a system that allows working under an argon-controlled atmosphere.



Fig. 9. Glove box of the Jacomex manufacturer, model GP Campus.

After that, mechanical alloying (MA) was committed in a planetary ball mill of the Retsch manufacturer, model PM 400/2 (**Fig. 10**). For this purpose, elemental mixtures were poured into two stainless-steel jars (**Fig. 11**) to alloy them. In these jars, chromium-steel balls make up the milling media. The milling process parameters were as follows: ball-powder weight ratio of 10/1 with 1 wt.% of stearic acid and milling speed of 350 rpm for 40 h. Stearic acid acts such a process control agent (PCA). Thus, it avoids excessive welding and limits particle growth.

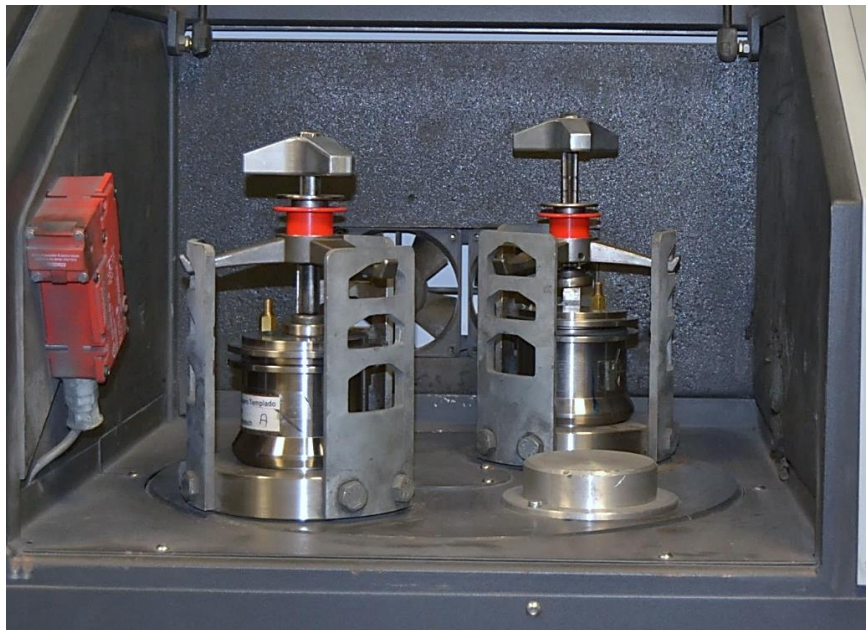


Fig. 10. Planetary ball mill of the Retsch manufacturer, model PM 400/2 (ITM).

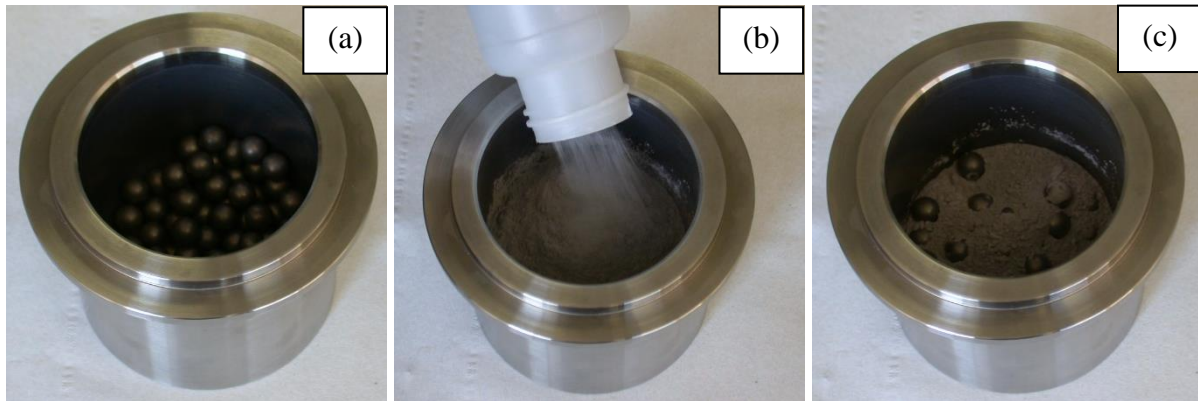


Fig. 11. Process of preparing the stainless-steel jars prior to mechanical alloying (MA): (a) balls introduction, (b) dust discharge, and (c) final result (ITM).

With this duration, the mixing powders were alloyed enough, allowing the reduction of energy consumption, and the avoidance of flaring when removing the powder. In addition, no stops were made in order to prevent burning. Actually, during the alloying procedure, the mixing powders were also protected within a high-purity Ar-atmosphere.

After the end of the cycle, although the powder was easily detached, it completely adhered. For that reason, it could not be fully recovered, as detailed in (**Table 9**).

Table 9. Alloying powder obtention after MA.

Raw material	Mass put into the jars (g)	Mass removed from the jars (g)	Losses (%)
Equiatomic TNZT	57.754	57.305	1
Equimassic TNZT	58.652	57.252	2

Subsequently, the powders were compacted using a hydraulically operated compaction press model WPP 50 M of the Metallkraft manufacturer. The compaction was carried out by applying a pressure of 1,000 MPa for 10 seconds. For this purpose, the floating bending die (**Fig. 12**) is used, whose cavity for powder deposition has dimensions of 30x12x5 mm, namely a volume of 1.8 cm³. After performing this process for all the alloyed powder, green samples are obtained, which have the same dimensions as the die cavity and whose mass is calculated in **Table 8**. However, green samples have very poor properties, so a sintering process is necessary.

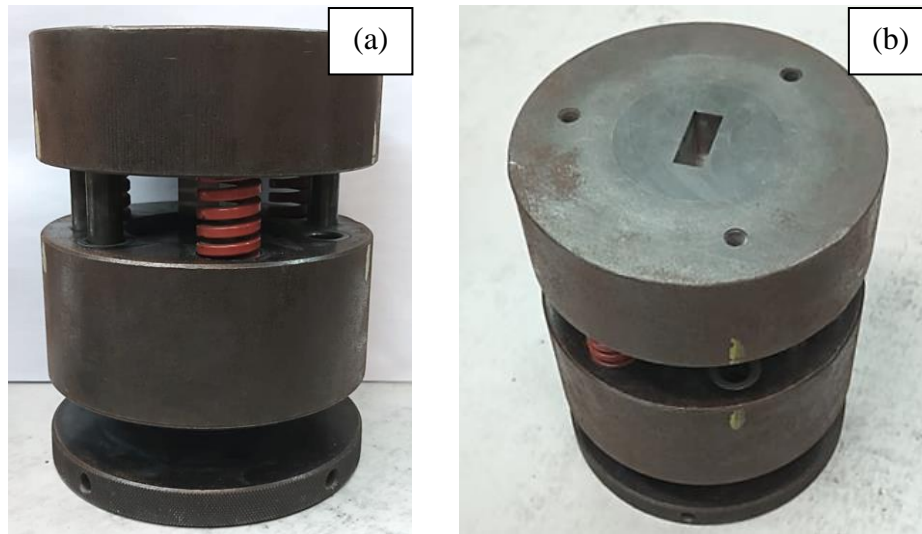


Fig. 12. *Floating bending die seen from (a) a front and (b) a top view.*

Although this process is easy to perform, it must be carried out with special care since contaminating particles can be adhered to the alloy as a consequence of the lack of a protective atmosphere. To avoid this, the surfaces in contact with the samples must be cleaned frequently.

After the end of the compaction process, measurements of the mass and dimensions of each sample were taken. It was then possible to determine the green density of the alloys, which subsequently allowed for further analysis of the sintering process.

In this case, sintering was carried out in a high vacuum furnace of the manufacturer Carbolite Gero Limited, model HVT 15-75-450 (**Fig. 13**), with a protective Ar-atmosphere to avoid sample oxidation. In this sense, sintering is an isothermal process that provides the alloys with energy to achieve their specific mechanical properties. This is gotten by the bonding of the particles as a cause of the generation of bridges that results in the enlarged contact area between the particles after diffusion, what increases the strength of the samples. Afterwards, densification occurs due to the growth of the grain size growth, which is accelerated with increasing temperature.



Fig. 13. High vacuum furnace of the manufacturer Carbolite Gero Limited, model HVT 15-75-450.

The main factors to be taken into account in this process are the sintering temperature and the exposure time. To determine these ones, it is necessary to consider the physical characteristics of the alloying elements. These are, for example, the particle size distribution of the raw materials (**Fig. 6**), the morphology of the powder (in **Fig. 5**), or the melting points of the different elements (**Table 11**).

In the sintering cycle performed at atmospheric pressure (**Fig. 14**), the temperature was increased by 5 °C per minute until a temperature of 800 °C was reached and kept up for one hour. This allows homogenisation of the temperature in the samples during the allotropic transition of titanium, which occurs at a lower temperature due to the addition of large amounts of alloying elements. After this time, the temperature was again increased to 1,400 °C and samples were exposed to this one for a period of three hours. After this time, the temperature was naturally reduced to room temperature.

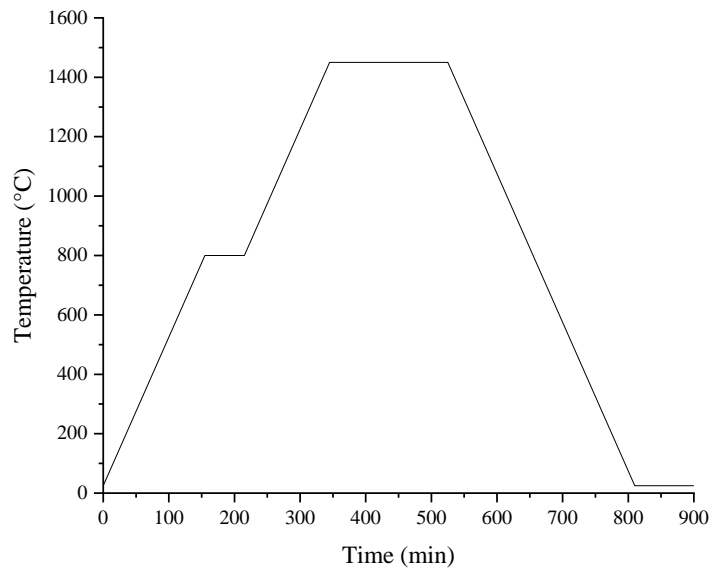


Fig. 14. Sintering cycle.

As can be seen in **Fig. 15 (a)**, which shows the state of the samples before sintering, and **(b)**, after sintering, during this process, grain formation occurs along with a volume shrinkage. This shrinkage is due to the rearrangement of the particles as a consequence of their exposure to high temperatures.

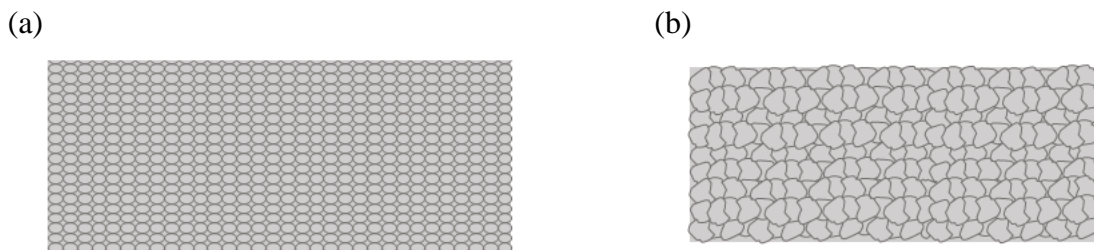




Fig. 15. Grain formation process during sintering: (a) before, (b) after.

Table 10 shows the legend associated with **Fig. 15**.

Table 10. Grain formation process during sintering caption.

Item	Allusion
	Compacted powders
	Sintered grains

3.1.2. As cast

When casting, it is important to bear in mind the very high values of the different elements melting points, especially in the case of Nb and Ta (**Table 11**). Moreover, these are very different, so it is to be expected that some segregations will occur due to these huge temperature differences between the melting points, what would produce a lack of homogeneity in the microstructure.

Table 11. Melting temperatures of the different elements that compose TNZT alloys.

Element	Melting temperature (°C)	Element	Melting temperature (°C)
Ti	1,668	Zr	1,855
Nb	2,477	Ta	3,017

The alloys casting was carried out using a compact arc melting furnace MAM-1 from Edmund Bühler GmbH. As in the case of sintering, the process was carried out under a protective vacuum atmosphere to avoid the appearance of oxides on the samples. To achieve chemical homogeneity, the alloys were remelted six times and turned over before each remelting.



Fig. 16. Arc melting furnace of the Edmund Bühler GmbH manufacturer, model MAM-1.

In addition to the limitation of the casting process, associated with the disparity of the elements melting temperatures, there is also an energy problem. The samples to be melted come, first of all, from a mixture of mechanically alloyed powders. This means that the samples contain a large amount of internal energy, which added to the high energy provided by the electric arc, can lead to the sample explosion. This occurs due to excess energy and could not only lead to a loss of material but could also cause damage to the equipment used.

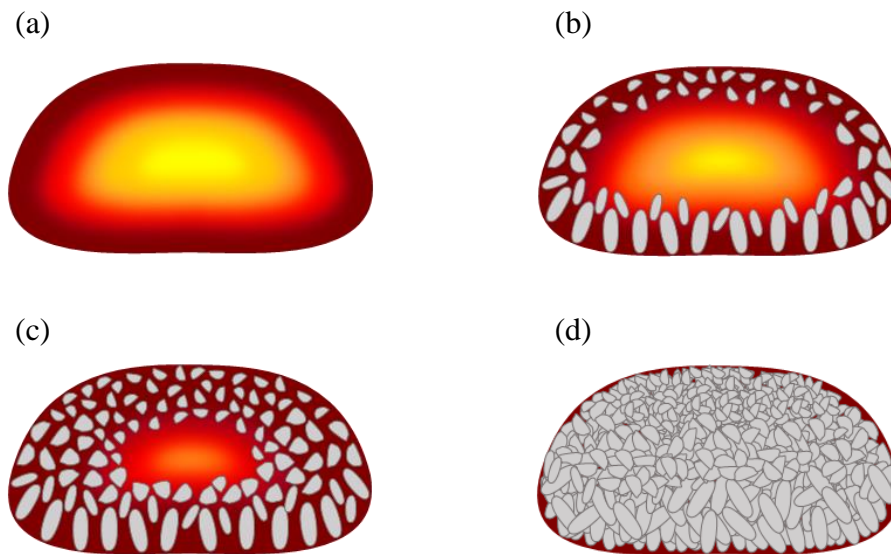





Fig. 17. Grain formation process during casting: (a) first step, (b) second step, (c) third step, (d) fourth step.

Fig. 17 shows the cooling process after sample casting according to the sequence (a) - (b) - (c) - (d). During cooling, the formation of dendritic grains in the perpendicular direction to the bearing surface, referred to as the bottom of the samples, is expected. **Table 12** shows the legend associated with **Fig. 17**.

Table 12. Grain formation process during casting caption.

Item	Allusion
	Top grains
	Central grains
	Dendrites

3.2. MICROSTRUCTURAL CHARACTERISATION

First of all, the following techniques have been used to characterise the obtained alloys microstructurally:

- X-Ray Diffraction.
- Optical Microscopy.
- Field - Emission Scanning Electron Microscopy.
- Electron Backscatter Diffraction.
- Transmission Electron Microscopy.

3.2.1. X-Ray Diffraction

This technique uses a diffractometer of the Bruker manufacturer, model D2 Phaser, consisting of an X-ray tube which emits wavelength $\text{Cu-K}\alpha$, a radiation detector, and a sample holder in which alloys are placed. Working conditions in the 2Θ range are between 20° to 90° of scanning and 0.02° step every 8 seconds at 30 kV and 15 kA. These parameters are important because for good Rietveld refinement, at least 8,000 counts must be achieved. Then, MAUD open software, version 2.993, developed by the University of Trento (2022) allows data treatment.

A given crystalline phase always produces a characteristic diffraction pattern. This landmark is the basis for the use of diffraction as a method of chemical analysis which is performed by identifying the pattern of each phase.

X-rays are electromagnetic radiation produced when an electrically charged particle with is slowed down in haste. In this sense, electrons are the commonly used particles, and the radiation is obtained in a device known as an X-ray tube.

Thus, X-ray interaction with matter occurs essentially through two basic processes. In the first one, some electrons from the incident beam are deflected without energy loss. These constitute the scattered radiation that exhibits exactly the same wavelength as the incident

radiation, which is the source of the diffraction phenomenon. In the second one, when incident, photons can undergo inelastic shocks, what causes the sample temperature to increase and gives rise to the Fluorescence phenomenon.

Diffraction is therefore essentially a scattering phenomenon, so a suitably large surface is required to ensure a good measurement. In diffraction, though the radiation is scattered in all directions, in some ones, the diffracted rays are in phase. It means that they mutually reinforce each other. Bragg's Law, shown in **Equation 2**, where n is an integer, λ is the wavelength of the X-rays, d is the lattice period or distance between atoms, and θ is the angle of incidence, defines this phenomenon.

$$n \cdot \lambda[\text{\AA}] = 2 \cdot d[\text{\AA}] \cdot \sin(\theta[^\circ]) \quad \text{Equation 2.}$$

3.2.2. Optical Microscopy

Optical microscopy is based on the use of lenses that allow the obtention of magnified images and work by refracting light waves. This makes it a very useful instrument for first inspections at low magnifications.

With it, images are taken at different magnifications and then processed to quantify area porosity and pore size, providing a complete analysis. However, this type of analysis has a limitation that involves the obtention of result for a two-dimensional porosity instead of a third-dimensional one.

Before optical microscopy, it is very important to prepare the samples' surface. For this purpose, samples are firstly mounted in the LaboPress-3 mounting press from Struers at 350 bar and 180 °C for 4 minutes before cooling. Then, they are roughened in the LaboPol-25 grinding machine from the manufacturer Struers, which runs at 300 rpm. First, a higher grain size silica sandpaper is used, followed by lower ones that cause less surface scratching (220 mesh (68 μm) - 500 mesh (30.2 \pm 1.5 μm) - 1000 mesh (18.3 \pm 1 μm)). Finally, samples are polished in the Struers LaboPol-5 polishing machine. Firstly, a long cloth is used together with a water-based diamond suspension, and secondly, a chemical cloth is employed together

with an OPS solution. After 4 minutes at 300 rpm under 20 N, a completely shiny surface suitable for analysis is obtained.

It should be noted that for optical microscopy, non-conductive resin can be used in the mounting press. In contrast, for electron microscopy, conductive resin must be used. In this case, as the samples analysed by optical microscopy are the same as those analysed by electron microscopy, non-conductive resin was used (**Fig. 18**).

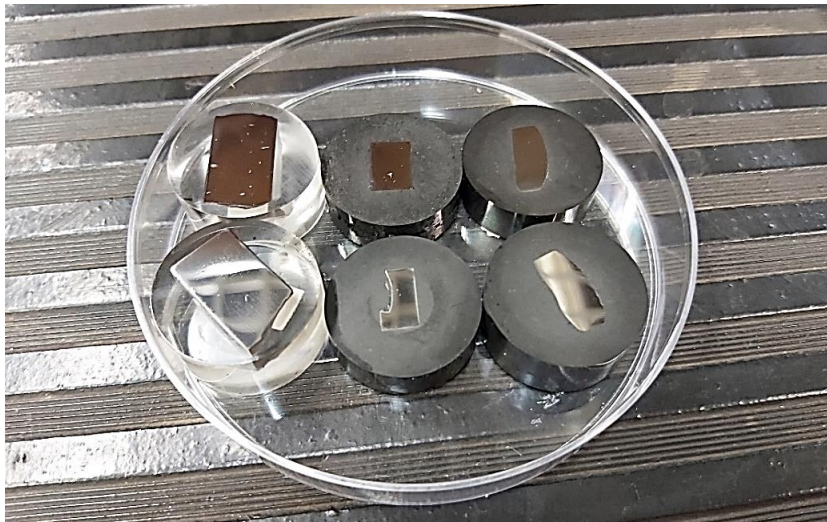


Fig. 18. Metallographic preparation of the samples with two types of resin: non-conductive and conductive.

3.2.3. Field - Emission Scanning Electron Microscopy

The Field-Emission Scanning Electron Microscope (FESEM) is an instrument capable of providing a wide range of information from the sample surface. The operation principle (**Fig. 19**) consists of scanning the surface of the samples with an electron beam obtained from a field emission gun. It provides high and low-energy electron beams that lets improve spatial resolution and work in very low potentials, which helps to avoid damage to electron beam-sensitive samples. These are 0.02 - 5 kV.

Secondary electrons (SE) are mainly used to move through the sample at low magnification in search of interest points, while backscattered electrons (ESB) provide higher contrast, allowing elements to be distinguished depending on their density. Finally, the energy dispersive X-ray spectroscopy (EDS) detector receives the scattered X-ray energy

characteristic of each chemical element, providing qualitative and quantitative analytical information of the sample surface.

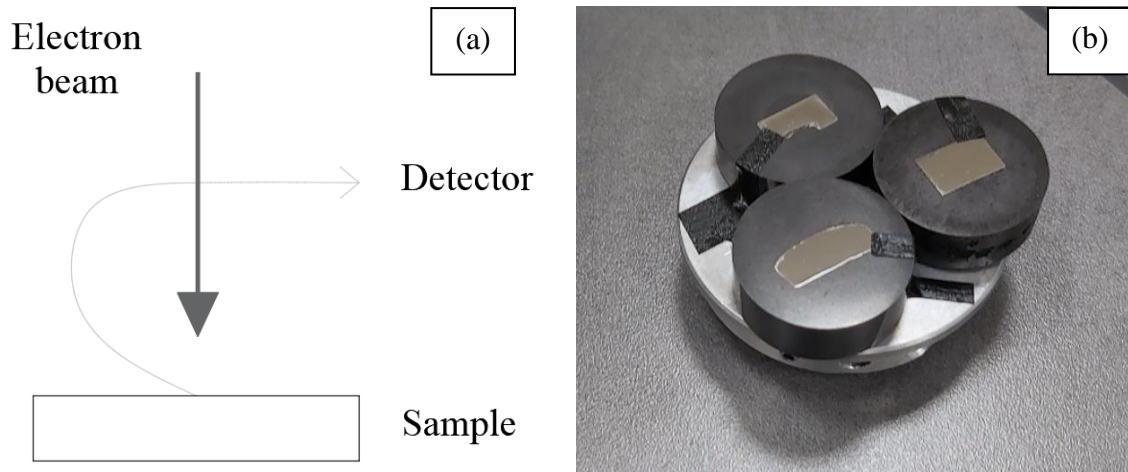


Fig. 19. (a) Sketch of the operation principle of the FESEM microscope and (b) sample placement in the sample holder.

Fig. 20 shows the equipment used for this purpose, which is the model ULTRA 55 from ZEISS. It consists of a SE detector, a ESB detector, an EDS detector, and a sample holder. Moreover, to treat the information provided, Aztec software is used.



Fig. 20. FESEM ZEISS ULTRA 55 (Servicio de Microscopía Electrónica of the UPV).

In addition to metallographically prepared samples, it is also used to produce fractograms from the fracture of samples (**Fig. 21**).

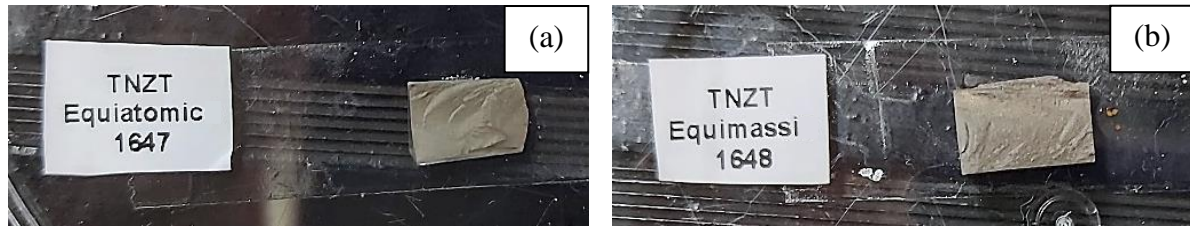


Fig. 21. Fractures of (a) equiatomic and (b) equimassic TNZT press and sinter samples.

3.2.4. Electron Backscatter Diffraction

The Electron Backscatter Diffraction (EBSD) technique allows the study of the crystalline orientation, which makes it possible to confirm the phases present in the alloys and to know the crystalline arrangement of the observed grains by means of Kikuchi bands (**Fig. 22**). In addition, this leads to the possibility of obtaining orientation relationships between crystallographic phases.

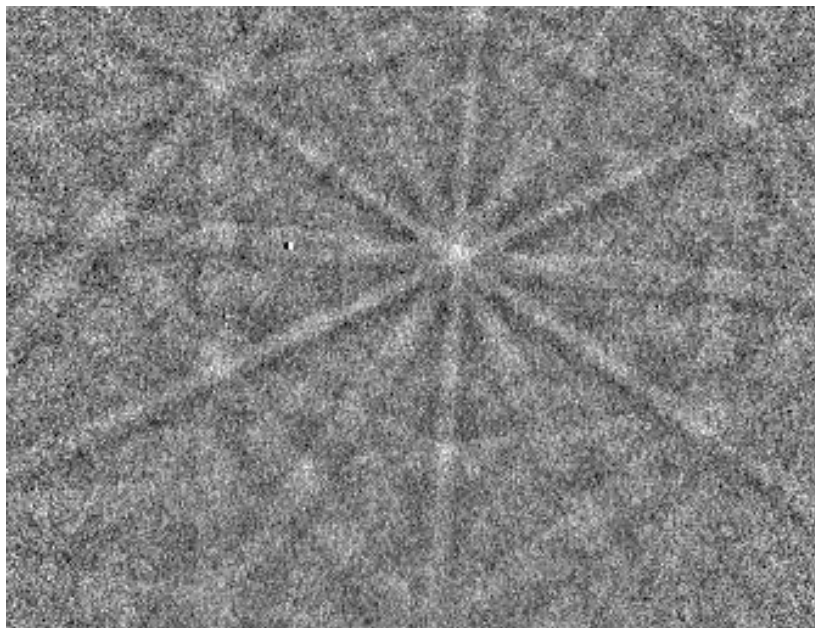


Fig. 22. Kikuchi bands obtained by EBSD.

As mentioned above, samples must be conductive, hence the need to have them mounted in conductive resin. In addition to the metallographic preparation previously done for optical microscopy, for EBSD it is needed to put the samples into the vibratory polishing machine of the Buhler manufacturer, model VibroMet 2, for 12 hours. Once the samples have been prepared, they are placed in a sample holder which is introduced into the equipment. In this

case, it is a focused gallium ion microscope (FIB) of the manufacturer ZEISS, model AURIGA Compact (**Fig. 23**) which working conditions are minimum 10 pixels per grain and a grain detection angle of 10° . For this technique, not only AZtec software is needed, but also AZtecCrystal.



Fig. 23. FIB ZEISS AURIGA Compact (Servicio de Microscopía Electrónica of the UPV).

Once inside, they are rotated 70° with respect to the vertical plane and the refracted electrons are absorbed by a phosphor display located 20 mm from the sample holder, as shown in **Fig. 24**.

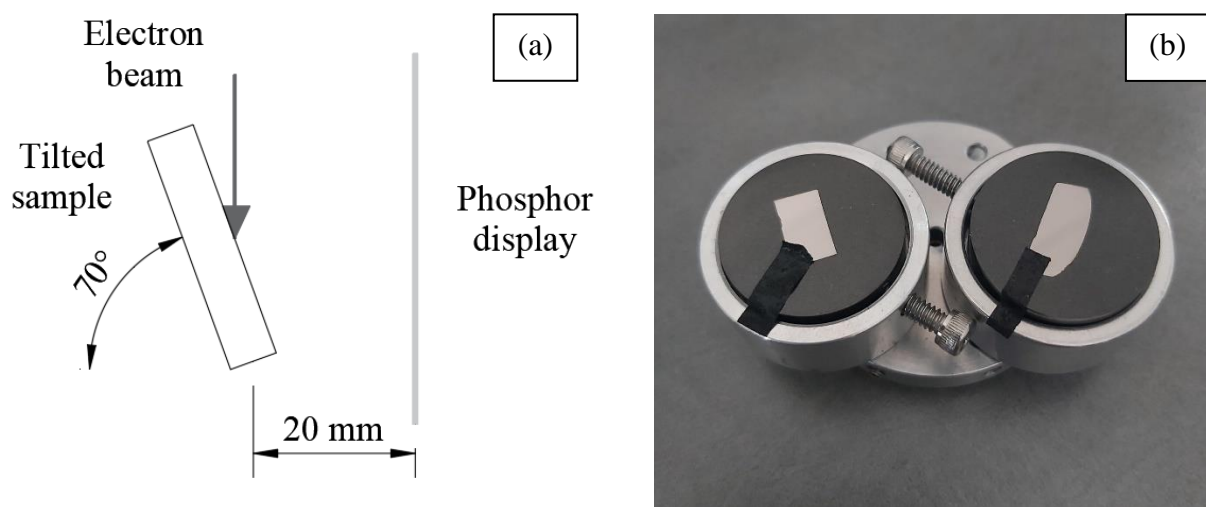


Fig. 24. (a) Sketch of the operation principle of the EBSD microscope and (b) sample placement in the sample holder.

3.2.5. Transmission Electron Microscopy

The Transmission Electron Microscope (TEM) of the JEOL manufacturer, model JEM 2100F, (**Fig. 25**) is an instrument that profits physic phenomena occurred when an electron beam collides with a sample, depending on its thickness and the type of atoms that form it, to analyse samples nanometrically and determine the crystalline microstructure of each phase by means of reciprocal space.



Fig. 25. TEM JEOL JEM 2100F (*Servicio de Microscopía Electrónica of the UPV*).

Samples must be sufficiently thin, since the image acquired depends on the ableness of the electrons to pass through the sample. Considering the operation principle of electron microscopy, illustrated in **Fig. 26**, the electron beam is scattered as it penetrates a thick sample, resulting in analyses with certain limitations. However, if a sufficiently thin sample is prepared, scattering does not occur. Consequently, high-precision analyses are achieved. Therefore, all sample preparation techniques aim to thin samples to thicknesses below 100 nm.

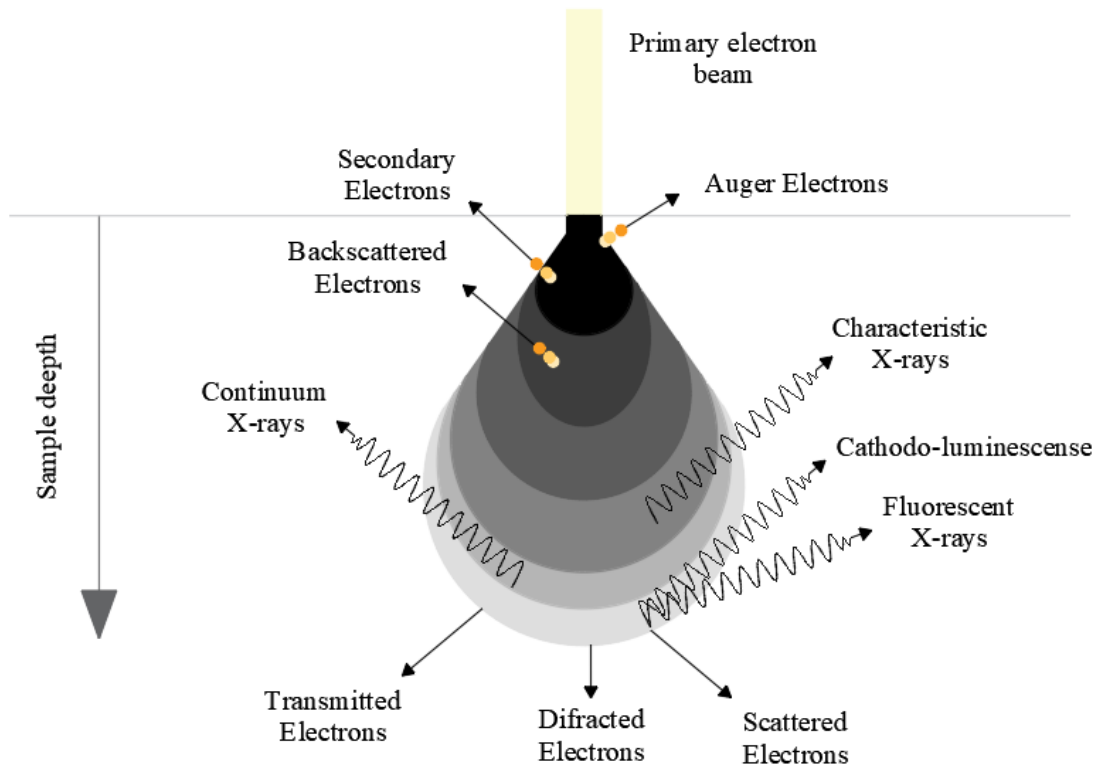


Fig. 26. *Electron Microscopy operation principle.*

To obtain such a lamella (**Fig. 27**), the FIB is used to select a very specific region due to its beam of Ga ions, which are much heavier than electrons, causing chemical bonds to be broken.

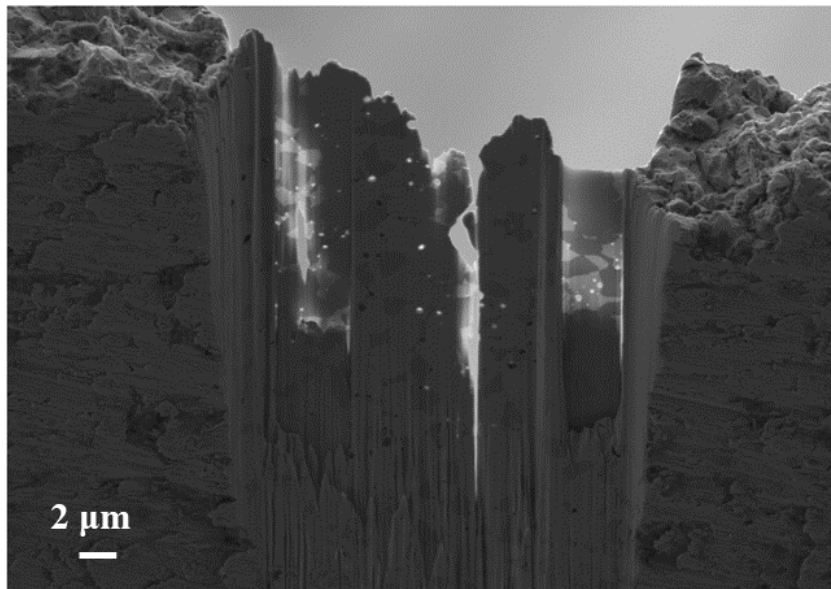


Fig. 27. *Lamella obtained by FIB for TEM.*

Due to the plasticity of the samples, it is very difficult to achieve a uniform thickness with ion milling, so some reliefs and bald spots are observed in the lamella. This also makes it difficult to diffract the electrons during TEM, which complicates the obtention of the diffraction pattern with which the phases present in the alloy can be structurally determined.

Despite these difficulties, once the test has been carried out, the horizontal, vertical, and diagonal distances between the diffraction points must be measured. With these measurements the distance between parallel planes is determined because the distance between points in reciprocal space is equal to the distance between planes of the same Miller indices in real space. **Fig. 28-30** show these measures where they are also compared with the distance obtained by XRD.

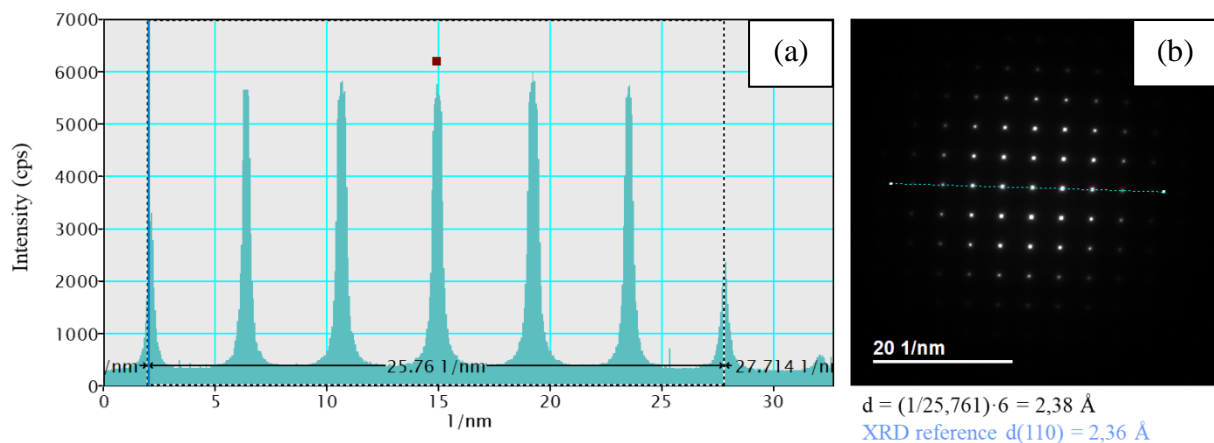


Fig. 28. (a) Horizontal distance measurement between (b) the diffraction points.

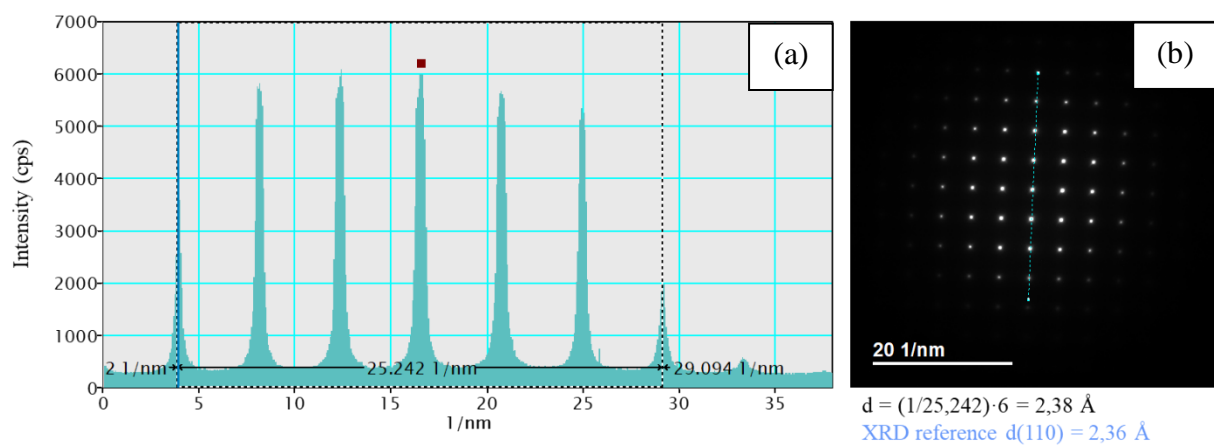


Fig. 29. (a) Vertical distance measurement between (b) the diffraction points.

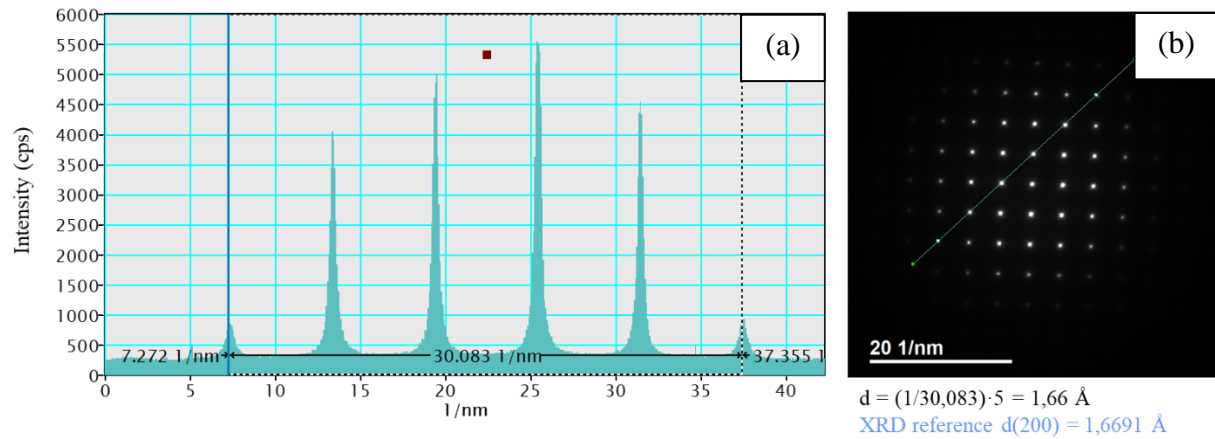
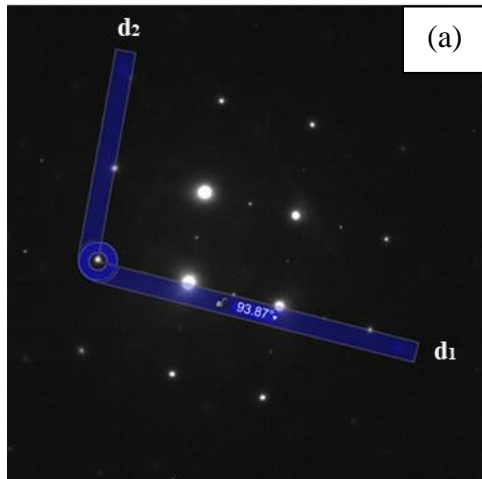


Fig. 30. (a) Diagonal distance measurement between (b) the diffraction points.

In addition, it is necessary to define the angle between planes in terms of the three different directions x , y , and z , so that all parameters are fully determined. In the same way, it is important to consider the extinction rules for crystallographic planes according to BCC and FCC cells (**Table 13**) in order to associate them with the $(h k l)$ plane. **Fig. 31-33** show how these measurements should be done.

Table 13. Extinction rules for crystallographic planes according to cell type.

(h k l)	BCC	FCC
(100)	-	-
(110)	X	-
(111)	-	X
(200)	X	X
(210)	-	-
(211)	X	-
(220)	X	X
(300)	-	X
(310)	X	-
(311)	-	X

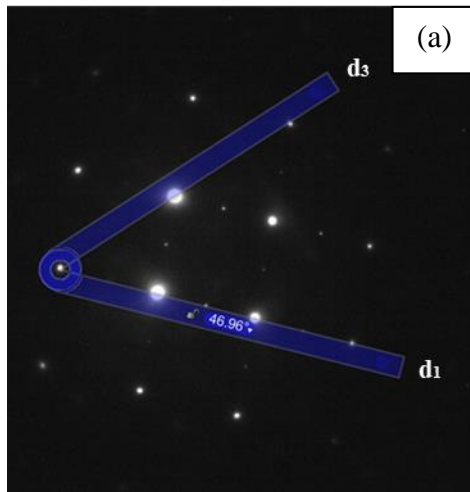


$d_1 = 1,41 \text{ \AA}$
 $d_2 = 1,40 \text{ \AA}$
 Angle $d_1:d_2 = 93,87^\circ$

(b)

	(hkl)#1	(hkl)#2	dhkl1	dhkl2	Angle(°)E(%)	Zone axis
V: [] (kV)	0,1,-3	3,-1,0	1,44	1,44	95,74	6,3
[] (Å)	3,-1,0	0,1,-3	1,44	1,44	95,74	6,3
L: [] (cm)	1,1,-3	3,-1,1	1,37	1,37	95,22	6,6
K: [] (cm.Å)	1,-3,-1	3,1,1	1,37	1,37	95,22	6,6
r1: [] (cm)	1,-3,1	3,1,-1	1,37	1,37	95,22	6,6
r2: [] (cm)	1,-3,-1	3,1,1	1,37	1,37	95,22	6,6
d1: [1,41] (Å)	3,-1,1	1,-3,1	1,37	1,37	95,22	6,6
d2: [1,4] (Å)	3,-1,1	1,-3,1	1,37	1,37	95,22	6,6
α: [93,87] (°)	1,1,3	3,-1,-1	1,37	1,37	95,22	6,6
	1,3,1	3,-1,-1	1,37	1,37	95,22	6,6

Fig. 31. (a) Measurement of the angle between d_1 and d_2 and (b) association to a crystallographic plane.

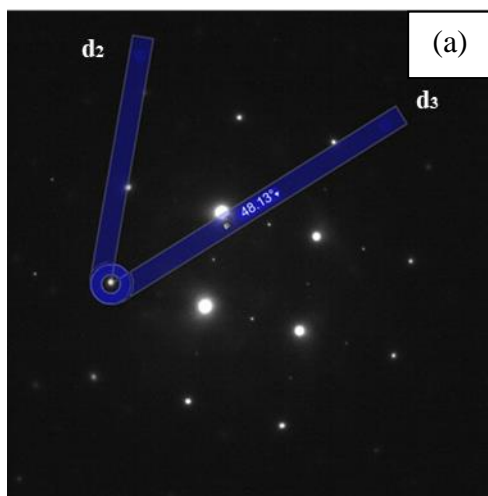


$d_1 = 1,41 \text{ \AA}$
 $d_3 = 1,03 \text{ \AA}$
 Angle $d_1:d_3 = 46,96^\circ$

(b)

	(hkl)#1	(hkl)#2	dhkl1	dhkl2	Angle(°)E(%)	Zone axis
V: [] (kV)	3,1,1	2,0,-4	1,37	1,02	47,61	5,8
[] (Å)	3,1,1	2,0,-4	1,37	1,02	47,61	5,8
L: [] (cm)	3,-1,-1	4,2,0	1,37	1,02	47,61	5,8
K: [] (cm.Å)	3,-1,-1	2,-4,0	1,37	1,02	47,61	5,8
r1: [] (cm)	1,-1,-3	0,2,-4	1,37	1,02	47,61	5,8
r2: [] (cm)	1,-3,1	4,-2,0	1,37	1,02	47,61	5,8
d1: [1,41] (Å)	1,-1,-3	4,0,-2	1,37	1,02	47,61	5,8
d2: [1,03] (Å)	3,-1,-1	4,0,2	1,37	1,02	47,61	5,8
α: [46,96] (°)	3,1,1	4,0,-2	1,37	1,02	47,61	5,8
	3,-1,-1	4,0,-2	1,37	1,02	47,61	5,8

Fig. 32. (a) Measurement of the angle between d_1 and d_3 and (b) association to a crystallographic plane.



$d_2 = 1,40 \text{ \AA}$
 $d_3 = 1,03 \text{ \AA}$
 Angle $d_2:d_3 = 48,18^\circ$

(b)

	(hkl)#1	(hkl)#2	dhkl1	dhkl2	Angle(°)E(%)	Zone axis
V: [] (kV)	3,1,-1	2,0,-4	1,37	1,02	47,61	4,9
[] (Å)	1,-1,-3	0,2,-4	1,37	1,02	47,61	4,9
L: [] (cm)	3,-1,1	4,0,-2	1,37	1,02	47,61	4,9
K: [] (cm.Å)	3,-1,1	2,-4,0	1,37	1,02	47,61	4,9
r1: [] (cm)	1,-3,-1	4,-2,0	1,37	1,02	47,61	4,9
r2: [] (cm)	3,-1,1	4,0,-2	1,37	1,02	47,61	4,9
d1: [1,4] (Å)	3,-1,-1	4,0,2	1,37	1,02	47,61	4,9
d2: [1,03] (Å)	3,-1,-1	2,-4,0	1,37	1,02	47,61	4,9
α: [48,18] (°)	1,-1,-3	4,0,-2	1,37	1,02	47,61	4,9
	1,1,-3	4,0,-2	1,37	1,02	47,61	4,9

Fig. 33. (a) Measurement of the angle between d_2 and d_3 and (b) association to a crystallographic plane.

3.3. MECHANICAL CHARACTERISATION

Secondly, for mechanical characterisation, different tests are carried out:

- Archimedes test.
- Determination of elastic modulus by ultrasounds.
- Hardness test.
- Microhardness test.
- 4-Point bending, micro-tensile, and micro-compression tests.
- Small-punch test.

3.3.1. Archimedes test

Archimedes test makes it possible to determine the porosity, distinguishing between closed and open, and, consequently, the densification obtained after carrying out both manufacturing processes.

For this purpose, the equipment shown in **Fig. 34** was used to measure the dry (D), submerged (S) and wet (M) mass of the samples. It is composed of a KERN 770 precision balance, a clamping structure, and counterweights.

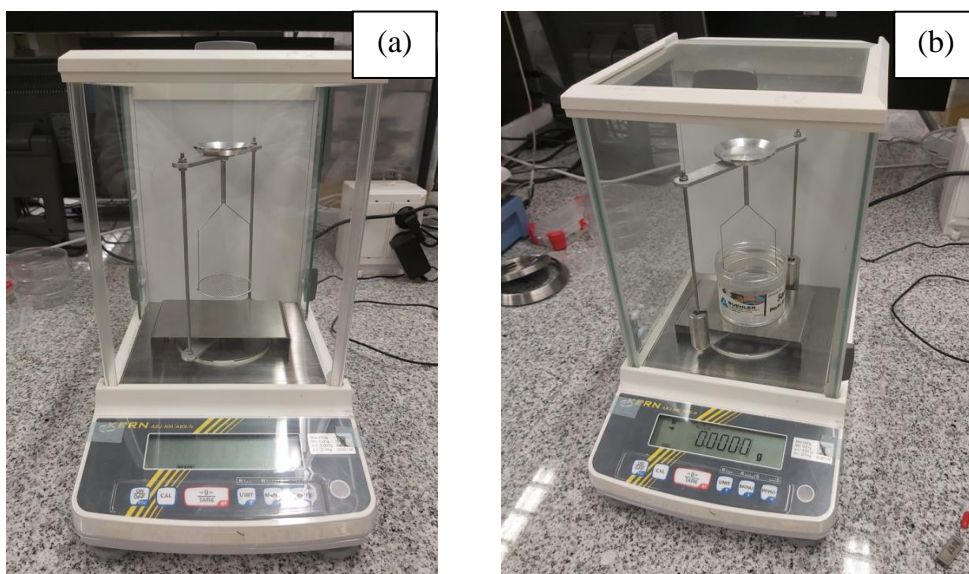


Fig. 34. Archimedes equipment (a) during and (b) after its assembly.

First, dry measurements (D) are performed. However, in order to perform them under proper immersion conditions, it is necessary to remove any air particle that may be present in the samples. To remove these particles, samples are placed in beakers with distilled water which are subjected to a vacuum process. After 20 minutes, the vacuum pump is stopped and the rest of the measurements, S and M, are performed. Finally, after data collection, samples are placed in an oven at 35 °C to remove all the liquid and leave them completely dry without altering the microstructure of the samples.

As follows from the following equations and taking into account that the density of water is 1 g/cm³, the intrinsic porosity of the alloys is determined from the measurements.

$$V_T[\text{cm}^3] = \frac{D[\text{g}]}{\rho_{\text{TNZT}}[\frac{\text{g}}{\text{cm}^3}]} \quad \text{Equation 3.}$$

$$V_{\text{EXT}}[\text{cm}^3] = S[\text{g}] - G[\text{g}] \quad \text{Equation 4.}$$

$$V_{\text{OP}}[\text{cm}^3] = M[\text{g}] - D[\text{g}] \quad \text{Equation 5.}$$

$$V_{\text{CP}}[\text{cm}^3] = V_{\text{EXT}}[\text{cm}^3] - V_T[\text{cm}^3] - V_{\text{OP}}[\text{cm}^3] \quad \text{Equation 6.}$$

$$P_O[\%] = \frac{V_{\text{OP}}}{V_{\text{EXT}}} \cdot 100 \quad \text{Equation 7.}$$

$$P_C[\%] = \frac{V_{\text{CP}}}{V_{\text{EXT}}} \cdot 100 \quad \text{Equation 8.}$$

$$P_T[\%] = P_O[\%] + P_C[\%] \quad \text{Equation 9.}$$

3.3.2. Determination of elastic modulus by ultrasounds

Ultrasonic non-destructive testing introduces high-frequency sound waves into a test object to obtain information about it without altering or damaging it in any way. Considering Poisson's coefficient 0.34 (typical value for all Ti alloys), wave speed, and density, elastic modulus can be calculated in **Equation 10**. There, ρ refers to the sample density, ν the Poisson's coefficient, and v the wave speed.

$$E = \rho[\text{g/cm}^3] \frac{V[\text{m/s}]^2 \cdot (1+\nu) \cdot (1-2\nu)}{\frac{1-\nu}{10^6}} \quad \text{Equation 10.}$$

When setting up the equipment Echograph 1090 from Karl Deutsch to be able to measure this speed, it is necessary to know the sample thickness. In addition, the surface on which carry out the test must be as flat and free of defect as possible.

3.3.3. Hardness test

For hardness test, the durometer used is the model HD9-45 from Centaur. This test consists of the application of a force of 15 N by means of a ball as an indenter which is applied between 10 and 15 seconds. After this time, the hardness measurement is provided by the equipment in HR15T. However, this type of measure is not common. Therefore, based on an approximation governed by **Equation 11**, the equivalent for Vickers hardness test (HV) is calculated.

$$HV = 0,049 \cdot HR15T^3 - 11,998 \cdot HR15T^2 + 985,460 \cdot HR15T - 26999 \quad \text{Equation 11.}$$

3.3.4. Microhardness test

For microhardness test, the methodology used is analogous to that of hardness. In this case, the Vickers test is directly performed. It provides a microhardness value which is governed by **Equation 12**, where F is the applied force, and D_i are the two diagonals printed on the sample after the test, which are observed thanks to the microscope.

$$HV = \frac{1.8544 \cdot F[\text{kg}]}{(D_1[\text{mm}] + D_2[\text{mm}])/2} \quad \text{Equation 12.}$$

The advantage of using this type of technique is that thanks to its application on a micrometric scale and the micrometres of the Shimadzu Vickers HMV-2 series micro-durometer, the hardness values can be determined more accurately. In addition, it includes a software called EasyTest that provides the value of the Vickers hardness calculated through the indenter mark.

3.3.5. 4-Point bending, micro-tensile, and micro-compression tests

In order to study the behaviour of the alloys under different stresses, different tests were carried out on the Shimadzu Autograph AG-100 KN Xplus universal testing machine (**Fig. 35**) by means of Trapezium X software. In addition, for each particular one specific tooling were needed.



Fig. 35. Shimadzu Autograph AG-100 KN Xplus universal testing machine.

Bending tests are the most commonly used to evaluate the behaviour of specimens subjected to shear and bending stresses. Specifically, 4-point bending test, shown in **Fig. 36**, has been performed for this case so the equations governing the stresses supported by the specimens, as well as the deformation suffered, are shown in **Equation 13** and **14**. Unmachined samples were used for this test.

$$\sigma[\text{MPa}] = \frac{0.75 \cdot F[\text{N}] \cdot L[\text{mm}]}{w[\text{mm}] \cdot t[\text{mm}]^2} \quad \text{Equation 13.}$$

$$\varepsilon[\text{mm/mm}] = \frac{4.36 \cdot \Delta l[\text{mm}] \cdot t[\text{mm}]}{L[\text{mm}]^2} \quad \text{Equation 14.}$$

Here, σ refers to the stress, F to the force, L to the average length between supports, w to the width, t to the thickness, and Δl to the extensimetry.

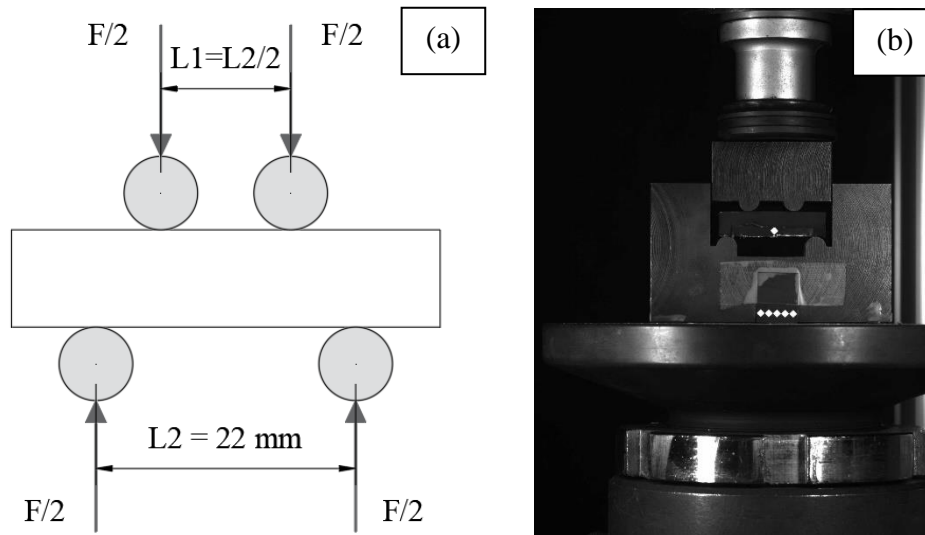


Fig. 36. Bending test (a) sketch and (b) procedure.

Fig. 37 shows, on the one hand, the morphology of the samples before the test and, on the other hand, the breakage produced after it.

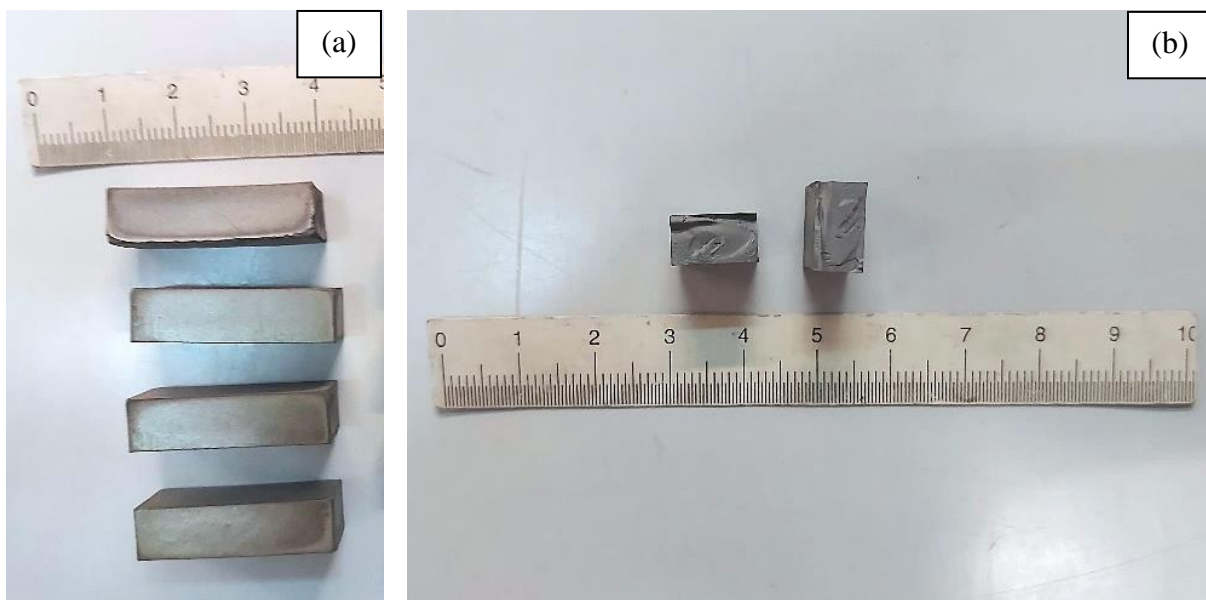


Fig. 37. Sample (a) before and (b) after the 4-point bending test.

Tensile tests are used to evaluate the behaviour of the material against uniaxial forces that stretch it. For the development of this test, it was necessary to shape the samples until the obtention of the dimensions shown in **Fig. 38 (a)** were obtained.

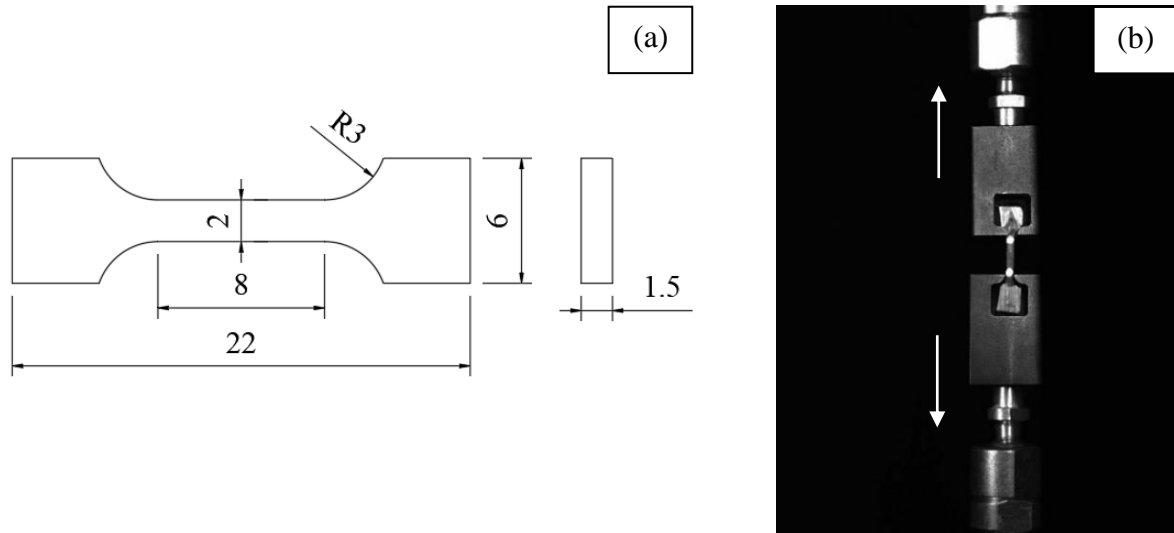


Fig. 38. (a) Samples geometry for micro-tensile test in mm and (b) micro-tensile test procedure.

Fig. 39 shows, on the one hand, the morphology of the samples before the test and, on the other hand, the breakage produced after it.

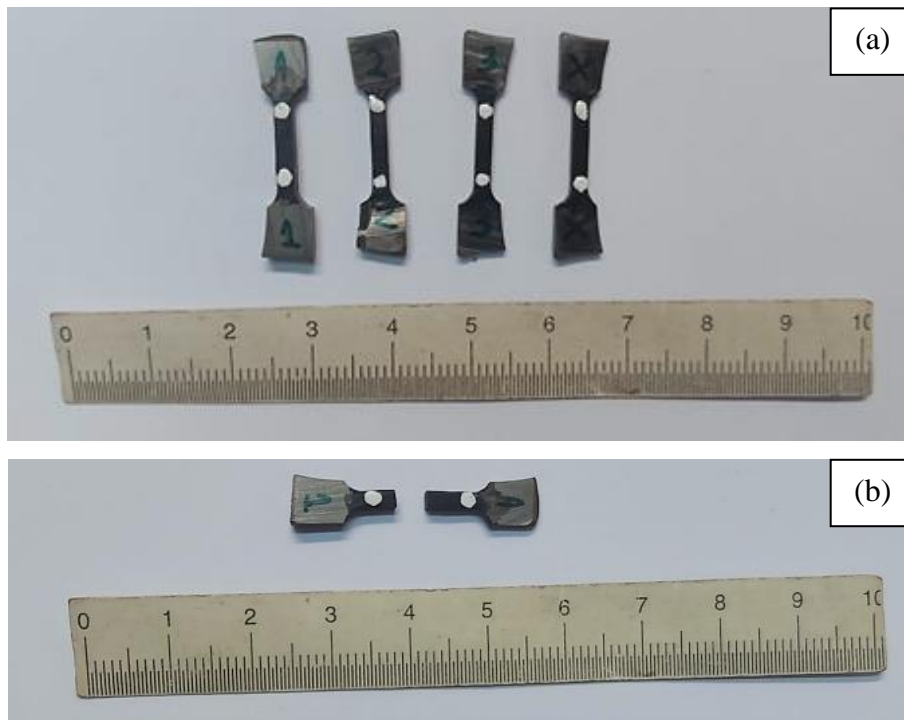


Fig. 39. Sample (a) before and (b) after the tensile test.

Compression tests allow the evaluation of the material behaviour against uniaxial forces compressing it. As in the previous case, it is necessary to cut the sample into different specimens whose shape is defined in **Fig. 40 (a)**.

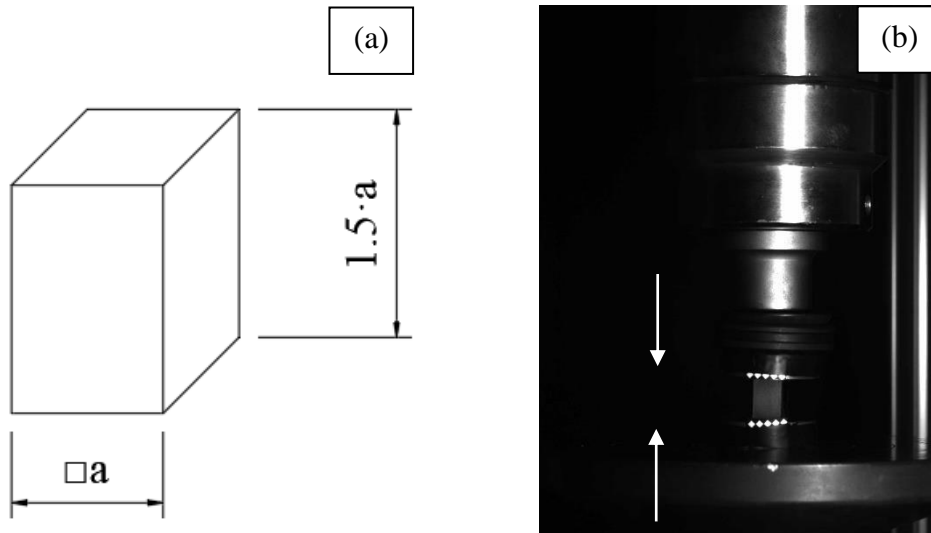


Fig. 40. (a) Samples geometry for micro-compression test in mm and (b) micro-compression test procedure.

Fig. 41 shows, on the one hand, the morphology of the samples before the test and, on the other hand, the breakage produced after it. It should be noted that all but one of the samples tested exploded.

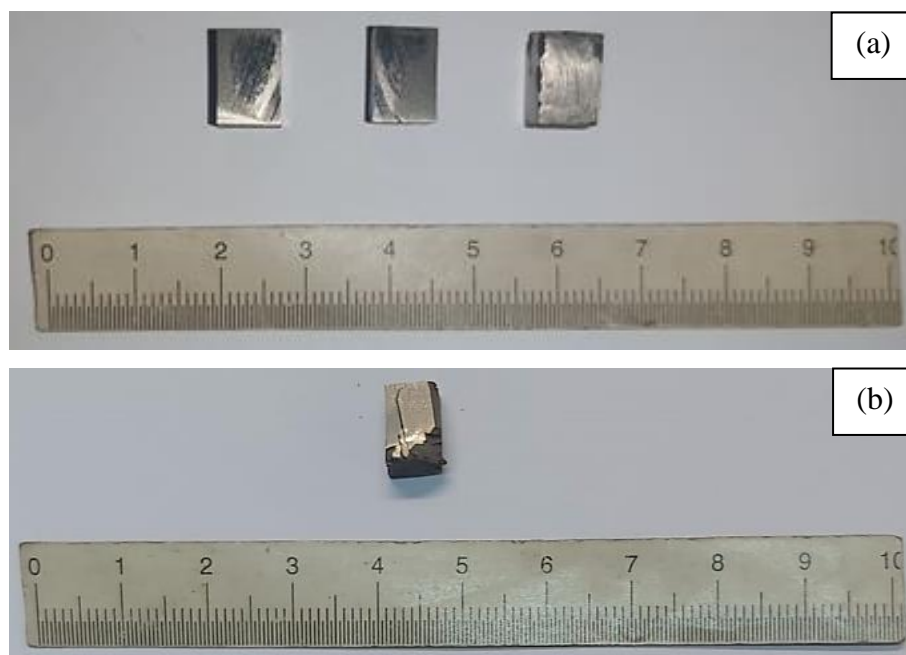


Fig. 41. Sample (a) before and (b) after the compression test.

Unlike 4-point bending test, micro-tensile and micro-compression test does not require a specific equation to determine the stresses supported by the specimens nor the deformation suffered. General equations shown in **Equation 15** and **16**, where A is the force application area, and h the height of the samples, determine these parameters.

$$\sigma[\text{Mpa}] = F[\text{N}]/A[\text{mm}^2] \quad \text{Equation 15.}$$

$$\varepsilon[\text{mm/mm}] = \Delta L[\text{mm}]/h[\text{mm}] \quad \text{Equation 16.}$$

3.3.6. Small punch test

Finally, small punch test allows the study of the material capacity without the need for a large material requirement, as the tested samples are only 0,5 mm thick. Nevertheless, it is typically used in forged materials.

The operative principle governing this test is simple and consists of applying a load to the specimen through a 15 mm diameter (**Fig. 43**). In contrast, the analysis of the results can be considered the most characteristic thing since stresses and strains are not calculated. Results are based on the maximum force applied, and the force associated to the first fracture appearance, with its associated displacement values.



Fig. 42. (a) Dimensions of the ball used during small punch test in mm and (b) small punch test procedure.

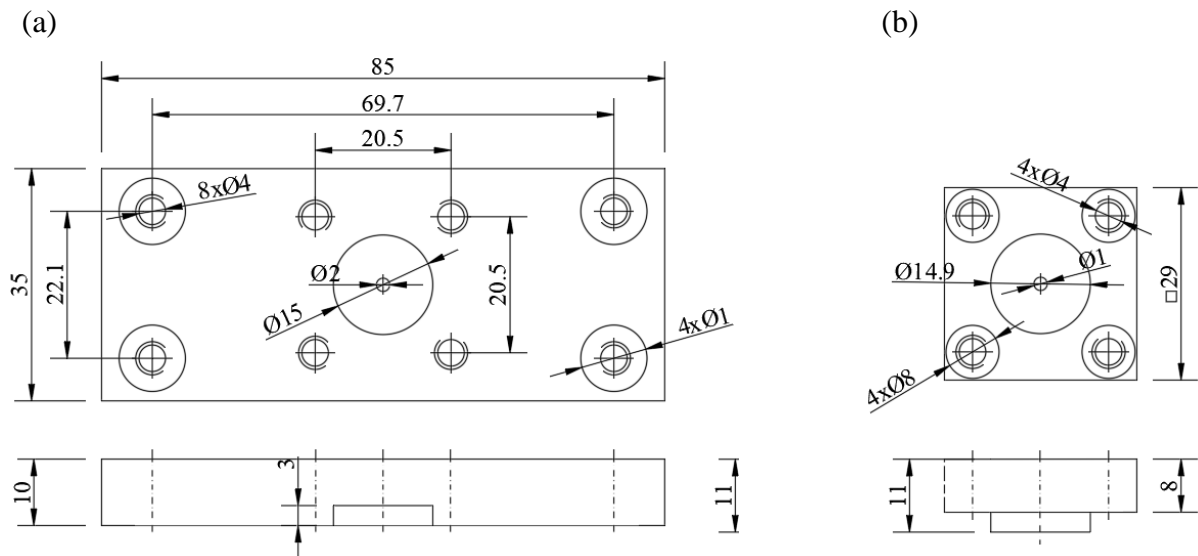


Fig. 43. Sketch of (c) the top and (d) the bottom of the small punch tooling in mm.

Fig. 44 shows, on the one hand, the morphology of the samples before the test and, on the other hand, the breakage produced after it.

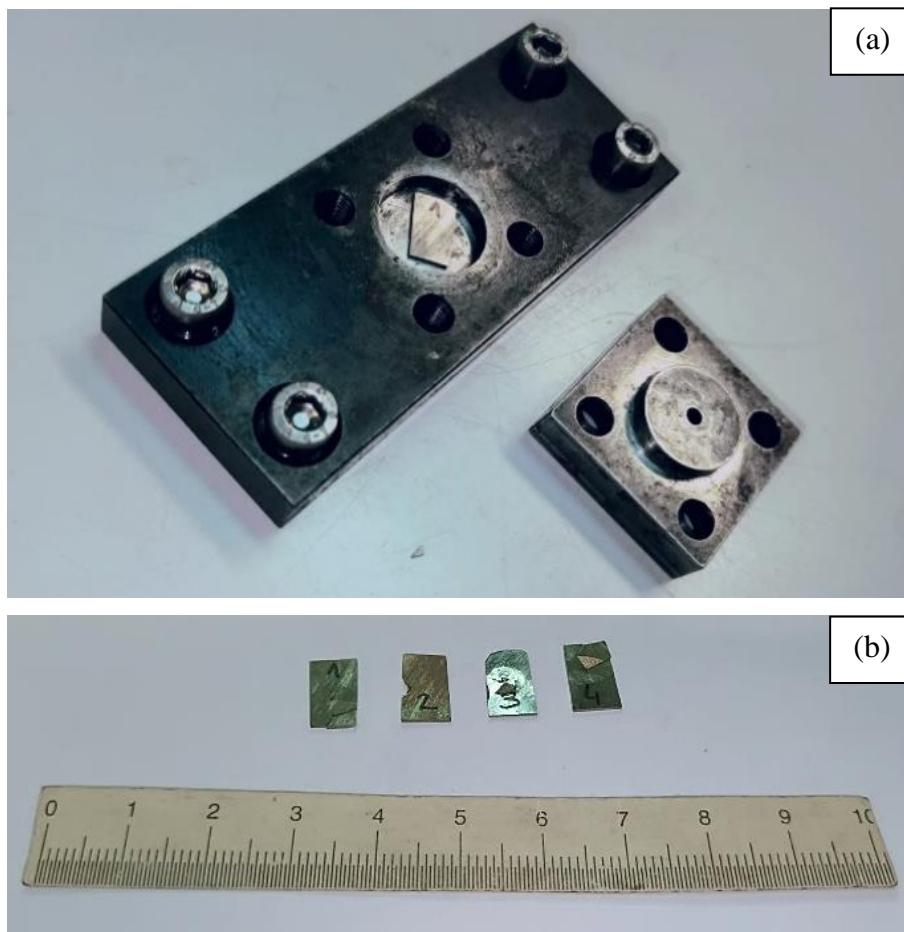


Fig. 44. Sample (a) before and (b) after the small punch test.

As detailed above, the data collected with Trapezium X software should be treated as shown in **Fig. 45**. Here, yellow, and green line represents the elastic and the plastic slope, respectively, blue line the first breakage, and the grey one the maximum supported force by the sample.

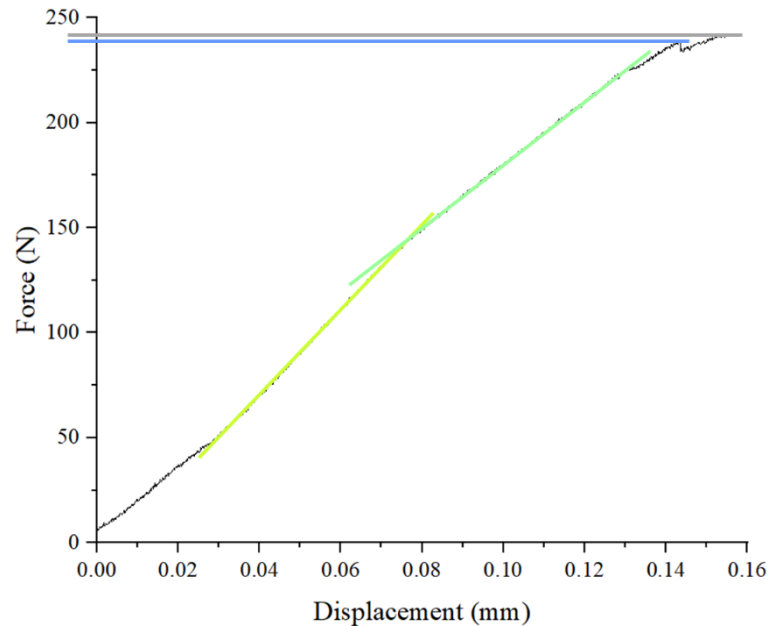


Fig. 45. Small-punch data treatment of the TNZT equiatomic mechanical alloying sample by powder metallurgy number 05 (EA-MA-PM_05) where yellow, and green line represents the elastic and the plastic slope, respectively, blue line the first breakage, and the grey one the maximum supported force by the sample.

3.4. CHEMICAL CHARACTERISATION

Finally, chemical characterisation is carried out using two techniques:

- Electrochemical corrosion.
- Determination of wettability.

3.4.1. Electrochemical corrosion

To accurately assess how electrochemical corrosion affects the developed alloys, potentiodynamic and electrochemical impedance spectrometry (EIS) tests have been performed using the Metrohm AUTOLAB AU51095 potentiostat together with NOVA

software. Afterword, results are treated by Mathematica and EIS Spectrum Analyser open software, version 1.0 from Bandarenka and Ragoisha (2013).

Potentiodynamic tests are divided into two distinct steps. First, the surface of the sample is cathodically cleaned by applying a potential of -1.15 V for 5 minutes. The aim of this first step of the potentiodynamic tests is the maximum reduction of the oxide layer which may have been formed on the electrode surface to avoid results being altered. Secondly, the open circuit potential (OPC) is measured for 6,000 seconds. This type of measurement is carried out with respect to a reference electrode when no current is flowing through the sample.

Potentiodynamic curves are obtained from this type of test and the morphology of results is illustrated in **Fig. 46**. There are two main domains corresponding to passivation and transpassivation. The first one is characterised by the appearance of an oxide layer that prevents the deterioration of the material. On the other hand, in the transpassivation domain, an increase in current density is observed as a cause of the beginning of the oxides dissolution that had previously formed. Thus, certain parameters are defined: i_{corr} referring to the corrosion current density, i_p as the passivation density, E_{corr} as the corrosion potential, E_p as the passivation potential, and E_b referring to the breakdown potential. Finally, it should be noted that Tafel curves are used to determine the corrosion parameters (i_{corr} , E_{corr}).

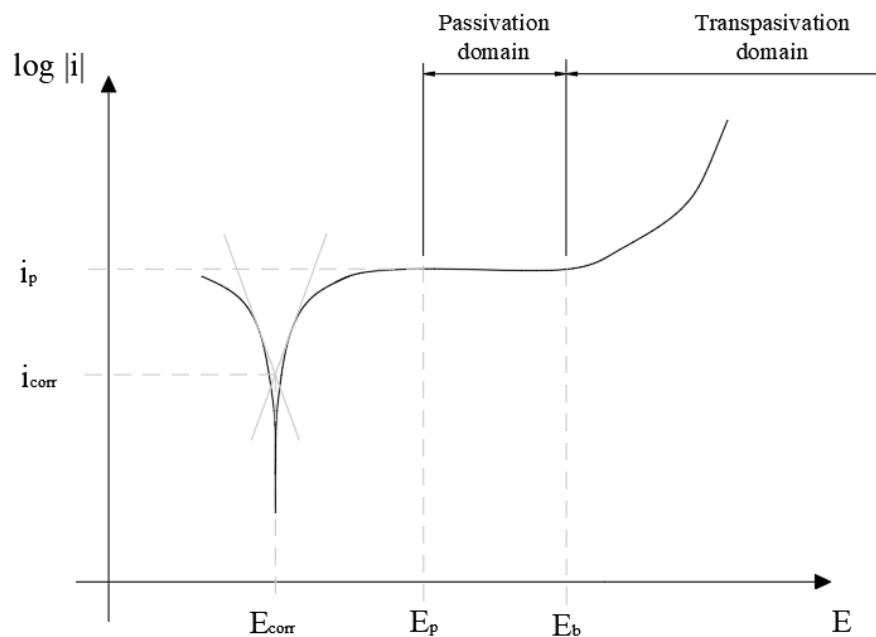


Fig. 46. Potentiodynamic polarisation curve.

With this current density and considering the alloy valence number (n), the atomic mass in g/mol, the exposed area in cm^2 , the Faraday constant, and the alloy density in g/cm^3 , the corrosion rate of the alloys is calculated as shown in **Equation 17**. In this case, the valence number is 4 and the exposed area is 0.785 cm^2 .

$$C_r[\mu\text{m}/\text{year}] = 3.272 \cdot 10^6 \left[\frac{\mu\text{m} \cdot \text{s}}{\text{year} \cdot \text{cm}} \right] \cdot \frac{i[\text{A}/\text{cm}^2] \cdot M[\text{g}/\text{mol}] \cdot A[\text{cm}^2]}{n \cdot F[\text{A} \cdot \text{s}/\text{mol}] \cdot \rho[\text{g}/\text{cm}^3]} \quad \text{Equation 17.}$$

On the other hand, the EIS allows the corrosive behaviour to be determined and parametrised. The principle of operation of this test is the application of a sinusoidal potential of 10 mV amplitude at different frequencies. Specifically, for this work, a frequency range of 5 mHz to 100 kHz was swept for one hour.

From this test, Nyquist and Bode diagrams are obtained to analyse the corrosion behaviour of the material by means of Equivalent Electrical Circuits (**Fig. 47**). The most common models for Ti alloys are the single-layer and the double-porous-layer circuit.

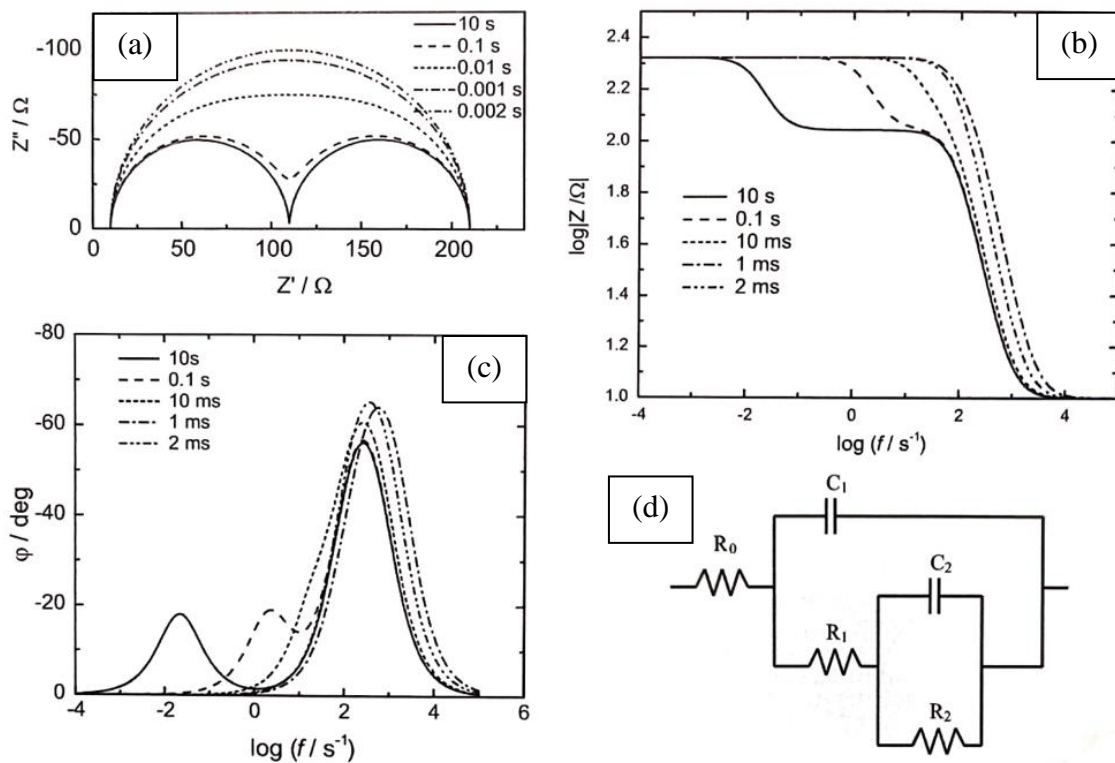


Fig. 47. (a) Complex plane and (b)(c) Bode plots for (d) a double-porous-layer circuit $R_0(R_1C_1)(R_2C_2)$ where R_0 represent the electrolyte resistance, R_1C_1 the compact layer, and R_2C_2 the porous one (Lasia, 2014).

As can be seen in **Fig. 48**, the value of the double-layer capacitance will depend on many factors, such as electrode potential, temperature, types and concentrations of ions, and oxide layers, among others.

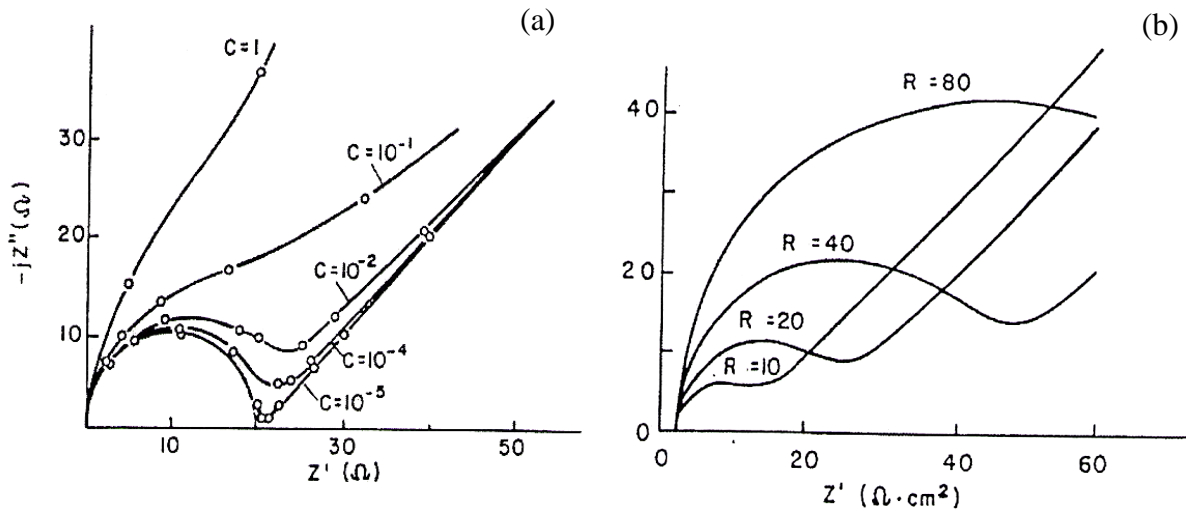


Fig. 48. Effect of (a) capacitance and (b) resistance in the complex impedance plane by means of Nyquist plots (Martín & Bautista, 2014).

To evaluate corrosion resistance of the alloys in biological media, a modified Ringer's-Hartmann's solution based on NaCl, KCl, CaCl₂, and lactate, with a pH between 6 and 7.2, has been used as electrolyte. Beforehand, it must be properly cleaned not to alter the test results. This is done with a 50% acetone-alcohol solution in which the sample to be analysed is introduced and passed through the ultrasonic cleaning equipment for 15 minutes.

The corrosion equipment is then assembled (**Fig. 49**). It consists of an AgCl electrode, a Pt counter electrode, a thermocouple, a corrosion cell, a lamp to stabilise the temperature at 37°C simulating that of the body, and a processor for data acquisition. The cell has this particular morphology because it was designed to allow tribocorrosion testing.

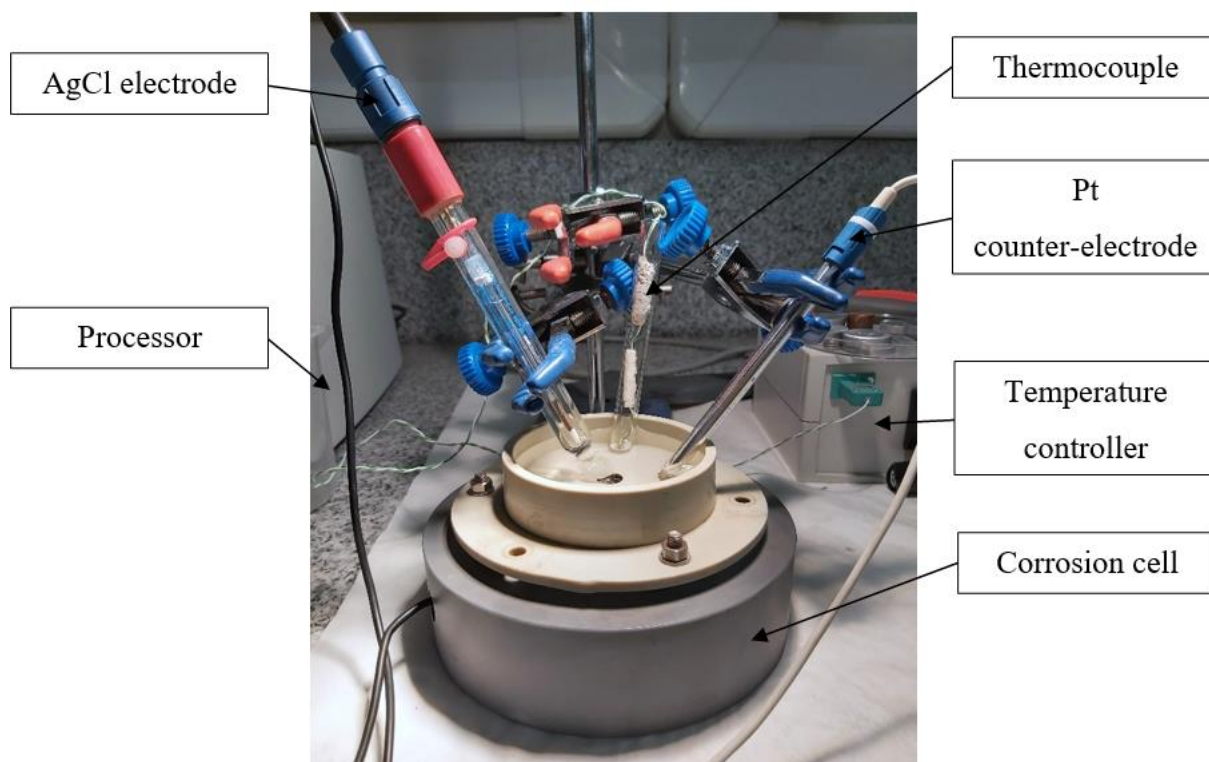


Fig. 49. *Electrochemical corrosion equipment.*

3.4.2. Wettability and contact angle

Wettability is a chemical property that determines the ability of a liquid to spread over a material. In fact, it is also related to the surface tension of that material. Namely if that angle is less than 90° the material is hydrophilic whereas if it is more, it is hydrophobic. Moreover, surface tension is higher in cases where the material is hydrophobic. This surface tension is a characteristic value of the interaction between the surface of a condensed phase with the surrounding environment. However, this term refers to liquids. In the case of solids, it can be understood as the surface energy and is a decisive factor for the coating or adhesion capacity of a material, which is especially important in the biological environment. Furthermore, unlike surface tension, the surface free energy of a solid is referenced to any liquid, so when it is high, the solid is usually easily wetted by any liquid.

To estimate the surface energy values of solids, it is possible to do by measuring the contact angles with a DSA25S KRÜSS Drop Shape Analyzer (**Fig. 50**) which, using polar and non-polar test liquids, provides the values of these properties. The two contact liquids used were

distilled water, to measure the dispersive component of the surface energy, and diiodomethane, to measure the polar one.

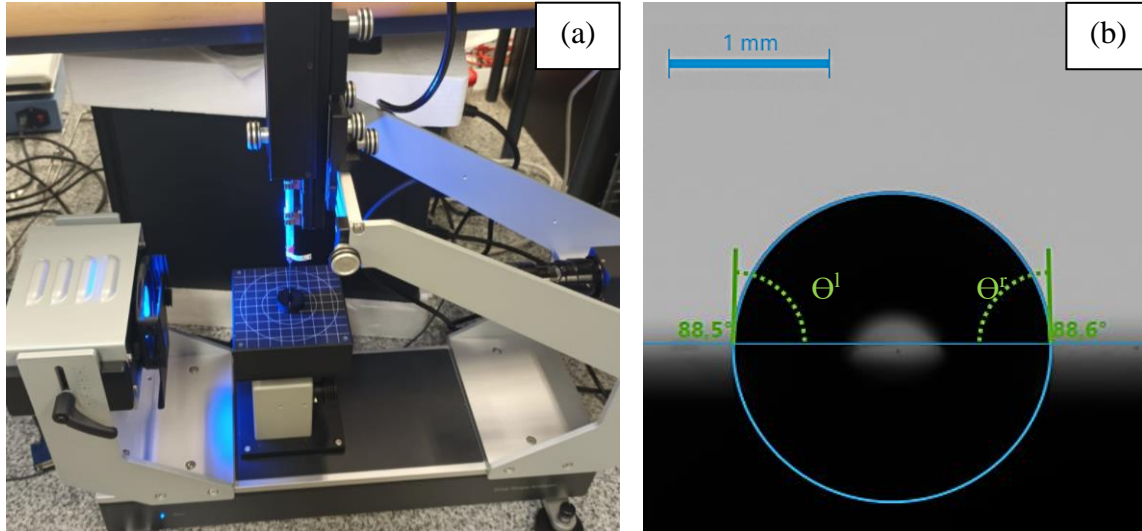


Fig. 50. (a) DSA25S KRÜSS Drop Shape Analyzer and (b) results obtained for the TNZT equiatomic mechanical alloying sample by powder metallurgy and casting, where Θ^l represents the contact angle measured on the left side and Θ^d that measured on the right one.

This equipment has a specific software that with the Owens-Wendt-Rabel-Kälble (OWRK) method allows relating the contact angle (Θ) to the surface tension values (γ). In particular, this method distinguishes between two specific types of interactions, dispersive (γ^d) and polar (γ^p) surface tension. All these parameters are related according to the mathematical expressions given in **Equations 17-19**.

$$\gamma[\text{mN/m}] = \gamma^d[\text{mN/m}] + \gamma^p[\text{mN/m}] \quad \text{Equation 18.}$$

$$\gamma_{SL}[\text{mN/m}] = \gamma_S[\text{mN/m}] + \gamma_L[\text{mN/m}] - 2 \cdot (\gamma_L^d \cdot \gamma_S^d)^{1/2} - 2 \cdot (\gamma_L^p \cdot \gamma_S^p)^{1/2} \quad \text{Equation 19.}$$

$$\gamma_S = \gamma_{LS} + \gamma_L \cdot \cos(\Theta[\text{rad}]) \quad \text{Equation 20.}$$

The liquids used to quantify the contact angle were chosen based on their different polarity. **Table 14** shows the surface tensions (γ_L) of the measuring liquids, as well as their dispersive (γ_L^d) and polar (γ_L^p) components.

Table 14. Distilled water and diiodomethane surface tension properties.

Liquid	γ_L (mN/m)	γ_L^d (mN/m)	γ_L^p (mN/m)
Distilled water	72.3	18.7	53.6
Diiodomethane	50.8	50.8	0

Finally, **Fig. 51** shows sample drops of liquid placed on the surface of the completely prepared and cleaned sample.

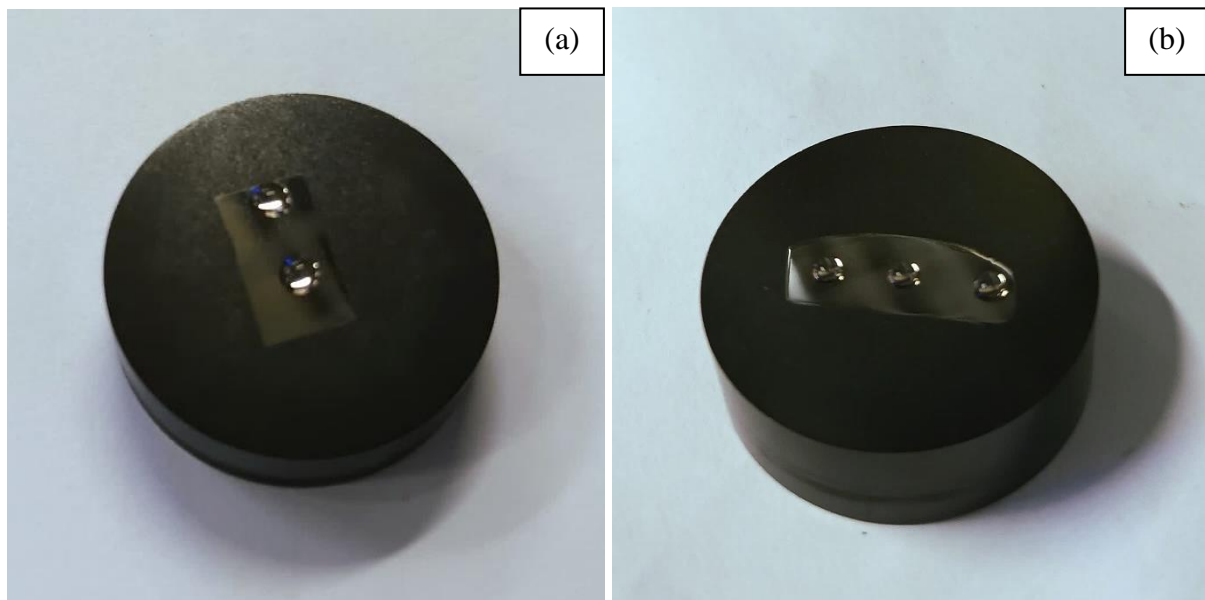
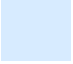





Fig. 51. Wettability procedure for TNZT mechanical alloying samples (a) by powder metallurgy and (b) by powder metallurgy and casting.

4. RESULTS

This chapter presents all the results obtained with the methods explained in the previous chapter. From now on, a colour legend has been defined for each type of alloy studied. This is shown in **Table 15**.

Table 15. *TNzT MEAs legend.*

Item	Allusion
	Equiatomic mechanical alloying by powder metallurgy (EA MA PM)
	Equimassic mechanical alloying by powder metallurgy (EM MA PM)
	Equiatomic mechanical alloying by powder metallurgy and casting (EA MA C)
	Equimassic mechanical alloying by powder metallurgy and casting (EM MA C)

4.1. POWDER OBTENTION BY MECHANICAL ALLOYING

After MA of the elemental mixture of powders, some powder vials were extracted and cross-sectioned. The homogeneity of the obtained alloy was studied by electron microscopy and the particle size distribution was also determined.

First, **Fig. 52** shows FESEM results at different magnifications. It can be seen that there is a percentage of fine particles in both cases, being it higher for the equiatomic alloy. Regarding particle morphology, in general, they have a more regular shape than the starting powders. Nevertheless, this is not always the case since there are some larger particles that cannot be considered equiaxial.

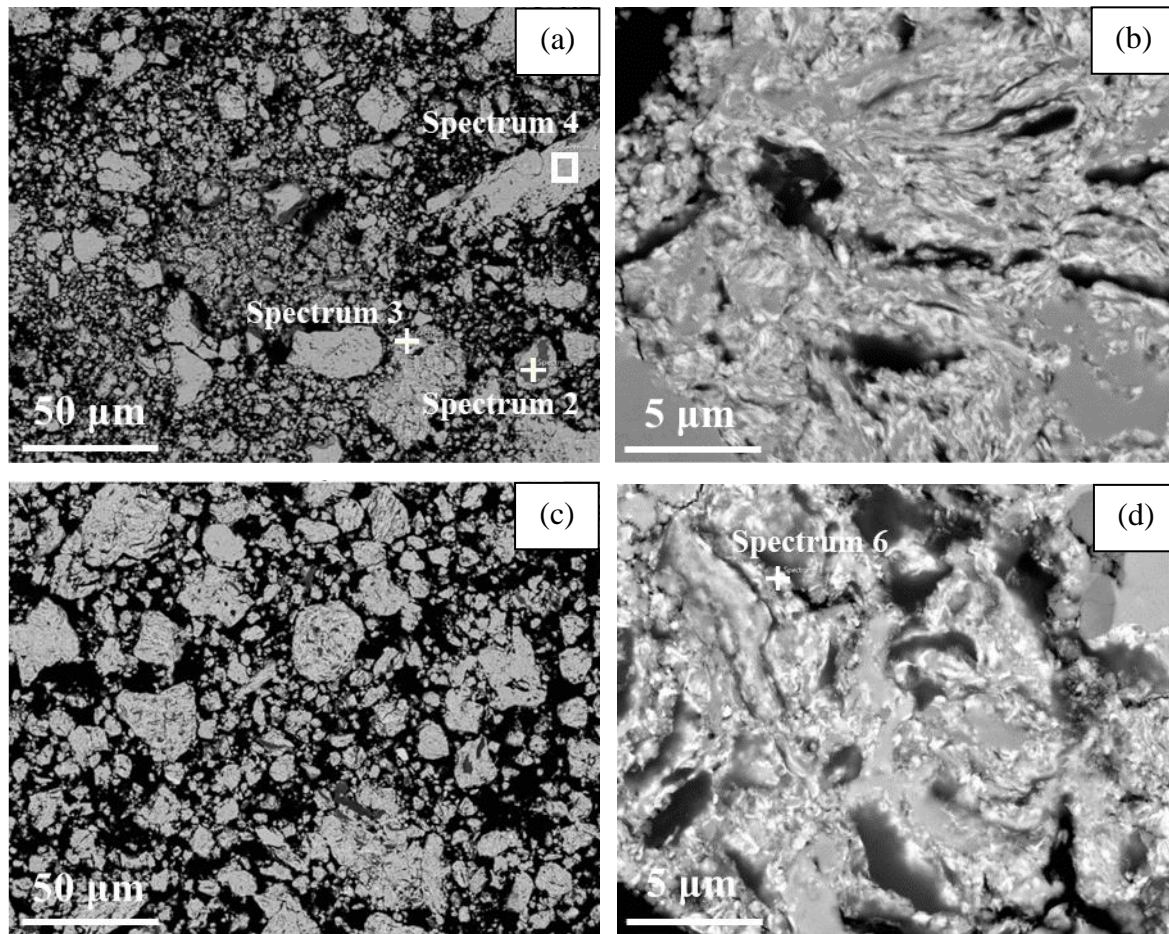


Fig. 52. Cross section of the equiatomic TNZT mechanically alloyed powder by (a) SE, and (b) BSE, and the equimassic TNZT mechanically alloyed powder by (c) SE, (d) BSE.

As for the compositions, **Fig. 52 (b)** and **(d)** show different colour composition corresponding to different elements within the same particle. This involves that after the grinding of the starting element particles, new, completely homogeneous particles have not been formed, which means that the elemental mixture of powders has not been fully alloyed.

To check this, different EDS were carried out at several points. The key is the analysis of the darkest and lightest areas, as well as a general mapping. In this way, the specific composition of some particle areas is determined approximately, as well as globally. The results of these analyses are detailed in **Table 16** and **Table 17**.

Table 16. Compositional analysis of the equiatomic TNZT mechanically alloyed powder from the spectra illustrated in Fig. 52 (a) and the mappings of Fig. 52 (a) and (b).

Element	At. %				
	Map (a)	Spectrum 2 (a)	Spectrum 3 (a)	Spectrum 4 (a)	Map (b)
Ti	28.3	33.6	50.8	27.9	27.1
Nb	23.8	24.1	16.1	24.9	26.2
Zr	23.4	20.9	18.7	23.5	23.2
Ta	24.5	21.4	14.4	23.7	23.5

Table 17. Compositional analysis of the equimassic TNZT mechanically alloyed powder from the mapping of Fig. 52 (c) and the spectrum illustrated in Fig. 52 (d).

Element	Wt. %	
	Map (c)	Spectrum 6 (d)
Ti	27.5	18.5
Nb	24.7	10.2
Zr	24.7	33.8
Ta	23.1	37.5

These analyses support the lack of alloying of the equiatomic and equimassic powders since in some areas the composition of a single element is twice as high as the others.

Secondly, the particle size distribution of the powders was measured. **Fig. 53** shows that, opposite to what was expected after MA in the planetary mill, powders have a larger effective size than the raw materials. It is explained by the agglomeration of particles during the MA process. Furthermore, in line with the FESEM images, the equimassic powder has a larger particle size than the equiatomic one.

In particular, it is noted that for the equiatomic case, the largest volume of particles corresponds to a size smaller than 100 microns. For the equimassic case, although there were

particles smaller than 100 microns, most of them were in the range between 100 and 1000 microns.

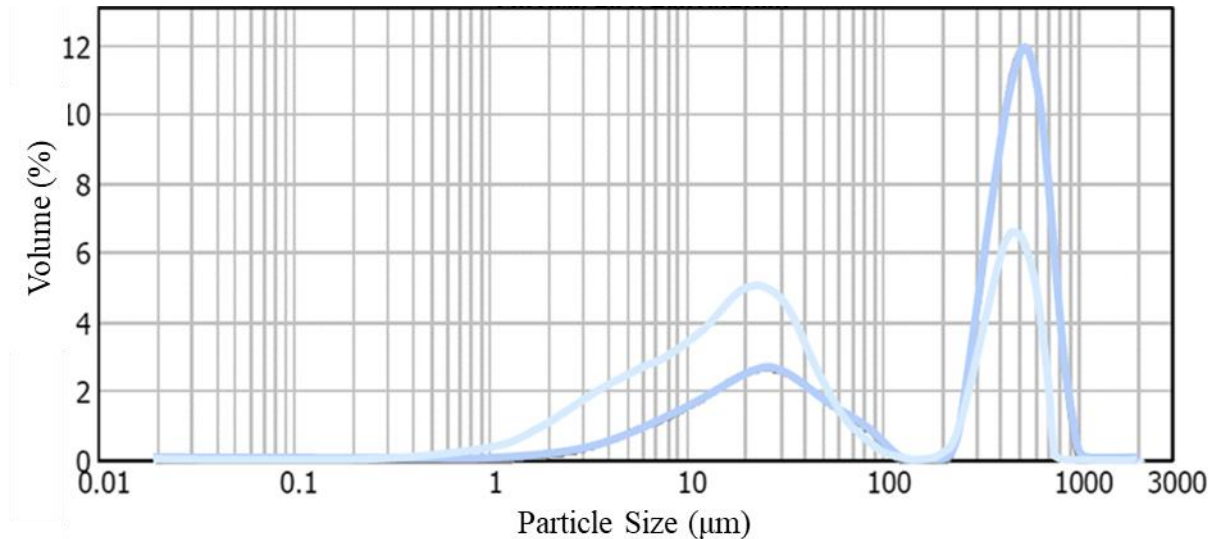


Fig. 53. TNZT alloyed powder particle size distribution for (■) equiatomic and (■) equimass composition.

To conclude the analysis of the alloyed powder, XRD was carried out, obtaining the diffractogram shown in **Fig. 54**. From here, a nomenclature associated with cell structure rather than chemical composition has been chosen to make it easier to analyse.

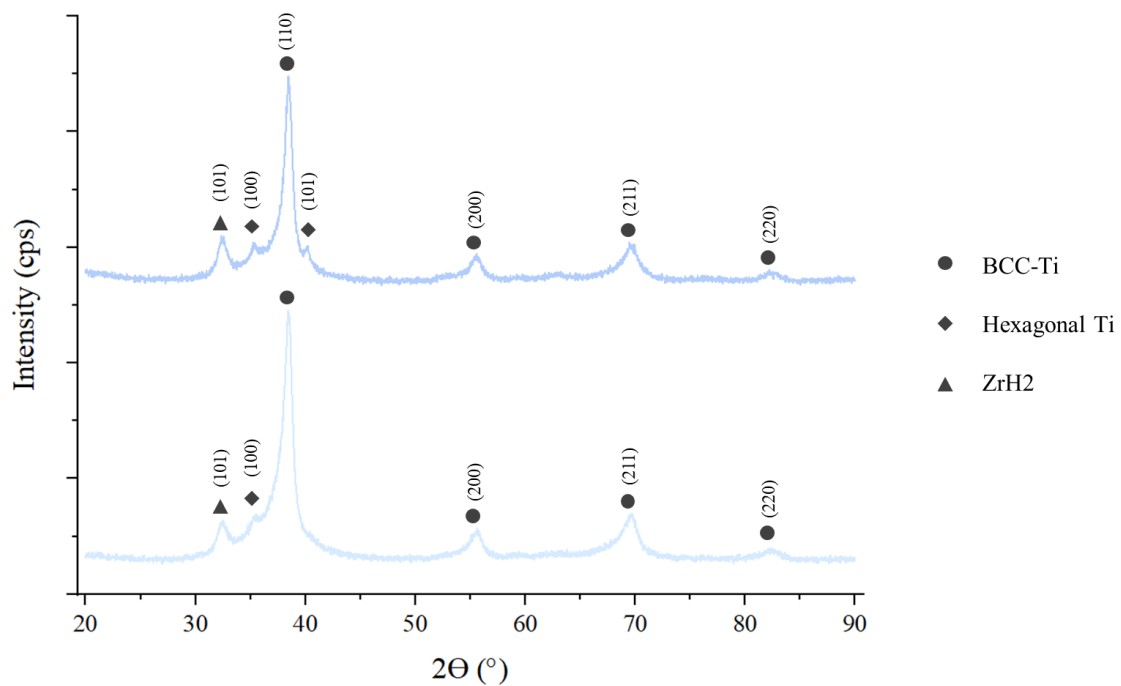


Fig. 54. TNZT alloyed powders XRD that shows crystallographic planes for each diffraction pick according to the distinct phases detailed.

During sintering, grain formation was gone together with a shrinkage of the volume of the samples, which resulted in a reduction of the porosity percentage. To evaluate these shrinkages, measurements of the dimensions of the samples were taken and results shown in **Fig. 55** were obtained.

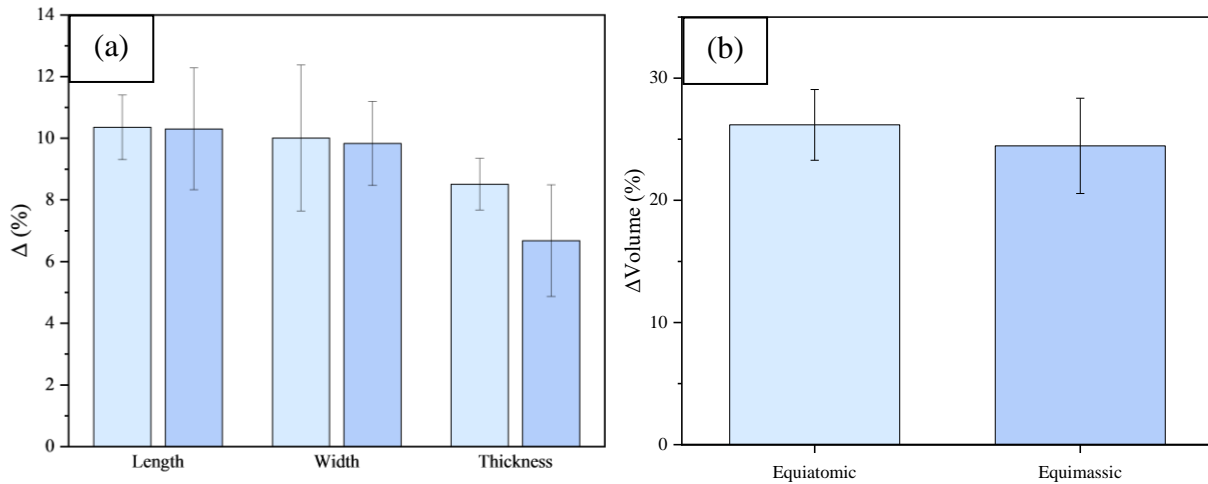


Fig. 55. TNZT samples shrinkage after sintering for (□) equiatomic and (■) equimassic mechanical alloying by powder metallurgy: (a) length, width, and thickness, (b) volume.

Table 18 shows the values associated with **Fig. 55**.

Table 18. TNZT samples shrinkage after sintering for equiatomic and equimassic mechanical alloying by powder metallurgy.

Shrinkage type	Equiatomic	\pm Error	Equimassic	\pm Error
Length	10.358	1.044	10.304	1.973
Width	10.007	2.368	9.831	1.362
Thickness	8.510	0.837	6.679	1.809
Volume	26.176	2.898	24.461	3.899

In the case of the equiatomic samples, porosity was reduced a 30%, together with volumetric shrinkage of just over 30%. While, in the case of the equimassic samples, porosity was reduced a 26% after volumetric shrinkage of slightly less than 25%.

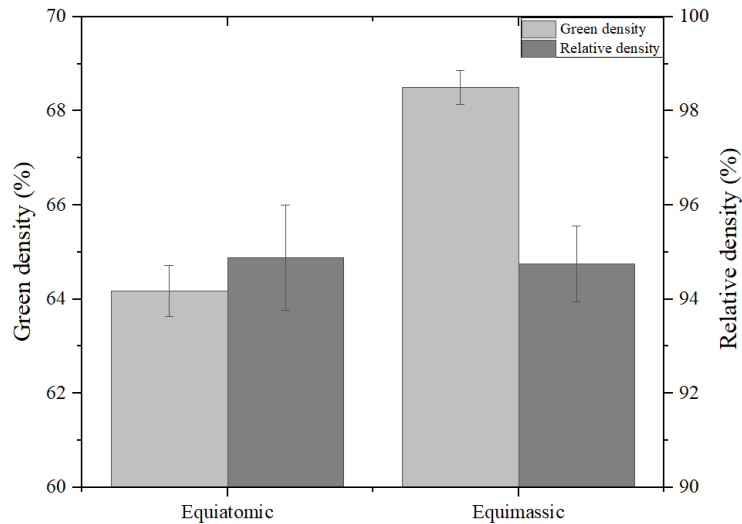


Fig. 56. Comparison between equiatomic and equimassic TNZT mechanical alloying samples density before and after sintering.

Table 19 shows the values associated with **Fig. 56**.

Table 19. Comparison between equiatomic and equimassic TNZT mechanical alloying samples density before and after sintering.

Alloy	Green density (%)	± Error	Relative density (%)	± Error
Equiatomic	64.177	0.539	94.880	1.120
Equimassic	68.502	0.358	94.756	0.810

4.2. MICROSTRUCTURAL CHARACTERISATION

First, the porosity of the alloys was studied using the Archimedes test and the analysis of optical microscopy images, in order to count the porosity per surface area. Subsequently, it was important to determine the existence of different phases within the crystalline matrix. For this purpose, surface etching was carried out using Kroll's reagent, which is the most popular metallographic etchant for titanium alloys, and electron microscopy. Thirdly, EDS analysis of each phase was carried out to determine the elemental composition of each one. Subsequently, XRD analyses were carried out to define the crystalline microstructure of the phases found. The crystallographic orientation of the crystalline microstructures was then studied by EBSD analysis, which also corroborated the previously defined microstructures.

Finally, the alloys were analysed in TEM. The aim was to confirm the chemical composition of each phase due to the high precision associated with this type of electron microscopy in addition to confirm the microstructure observed by XRD for each phase.

4.2.1. Porosity

The results obtained for the alloys porosity show an influence of the emplacement of the samples in the sintering furnace. Samples were introduced in parallel using two trays. This way, the argon flow attacked them head-on, as shown in **Fig. 57**, so the extreme located samples are the first to be encountered by the gas and are the most porous. Those in the centre are then protected by the turbulence created by the head-on collision. With it, it can be concluded the need to use diffusers that allow a homogeneous distribution of Ar.

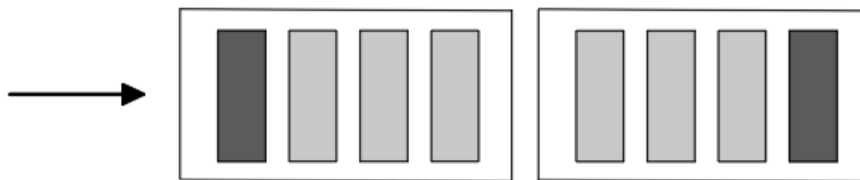


Fig. 57. Influence of sample positioning during the sintering process on porosity.

Despite this fact, it could be determined that the cast alloys have a lower porosity than those obtained simply by powder metallurgy. In turn, the equimassic alloys seem to have a lower porosity. In the case of casting, the results are clear. However, in the case of powder metallurgy, although the average porosity is higher for the equimassic case, the variation of the results shows that there are cases where this porosity is higher in the equimassic alloy.

Image processing confirms the trend between the porosity of as-casting and conventional powder metallurgy samples. However, some differences were found in the trend between the alloys according to their chemical composition. In this regard, in the case of casting, the equiatomic alloy shows a higher porosity than the equimassic alloy. However, opposite results were obtained for conventional powder metallurgy.

According to the porosity classification obtained by Archimedes, **Table 20**, where P_{OP} refers to open porosity, P_{CL} to closed porosity, and P_T to the total one, shows that equimassic samples have a significantly lower porosity than equiatomic samples. Considering that the

image processing takes into account the closed porosity and not the total porosity as in Archimedes, the results obtained are consistent.

Table 20. Open, closed, and total porosity (P_{OP} , P_{CL} , P_T) corresponding to equiatomic and equimassic TNZT mechanical alloying samples by powder metallurgy (EA MA PM, EM MA PM).

Alloy	Sample	$P_{OP}(\%)$	$P_{CL}(\%)$	$P_T(\%)$
EA MA PM	1,644	2.493	4.300	6.793
	1,645	0.575	4.085	4.660
	1,646	0.557	4.033	4.590
	1,647	0.173	4.264	4.437
EA MA PM	1,648	2.183	2.675	4.858
	1,649	1.976	2.924	4.900
	1,650	2.122	2.647	4.769
	1,651	4.560	1.889	6.449

The representation of the results obtained is shown in **Fig. 58**.

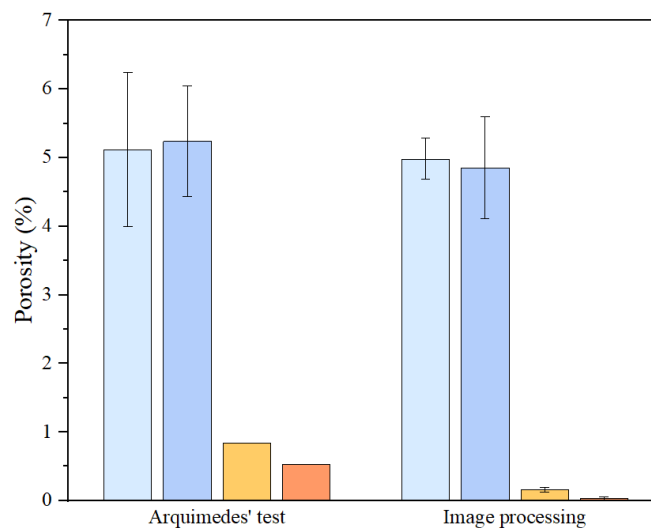


Fig. 58. Relatively porosity comparison between (light blue) equiatomic and (medium blue) equimassic TNZT mechanical alloying by powder metallurgy, and (yellow) equiatomic and (orange) equimassic TNZT mechanical alloying by powder metallurgy and casting.

Table 21 shows the values associated with **Fig. 58**.

Table 21. Relative density and relative porosity comparison between equiatomic and equimassic TNZT mechanical alloying by powder metallurgy (EA MA PM, EM MA PM), and equiatomic and equimassic TNZT mechanical alloying by powder metallurgy and casting (EA MA C, EM MA C).

Alloy	Arquimedes relative porosity (%)	Image processing relative porosity (%)	Difference (%)
EA MA PM	5.120 ± 1.120	4.981 ± 0.300	2.708
EM MA PM	5.240 ± 0.810	4.852 ± 0.740	7.398
EA MA C	$0.840 \pm 0.000^*$	0.164 ± 0.035	80.516
EM MA C	$0.530 \pm 0.000^*$	0.034 ± 0.022	93.585

(*) There is only one rough sample.

Visually, the porosity distribution for the different alloys is as shown in **Fig. 59**.

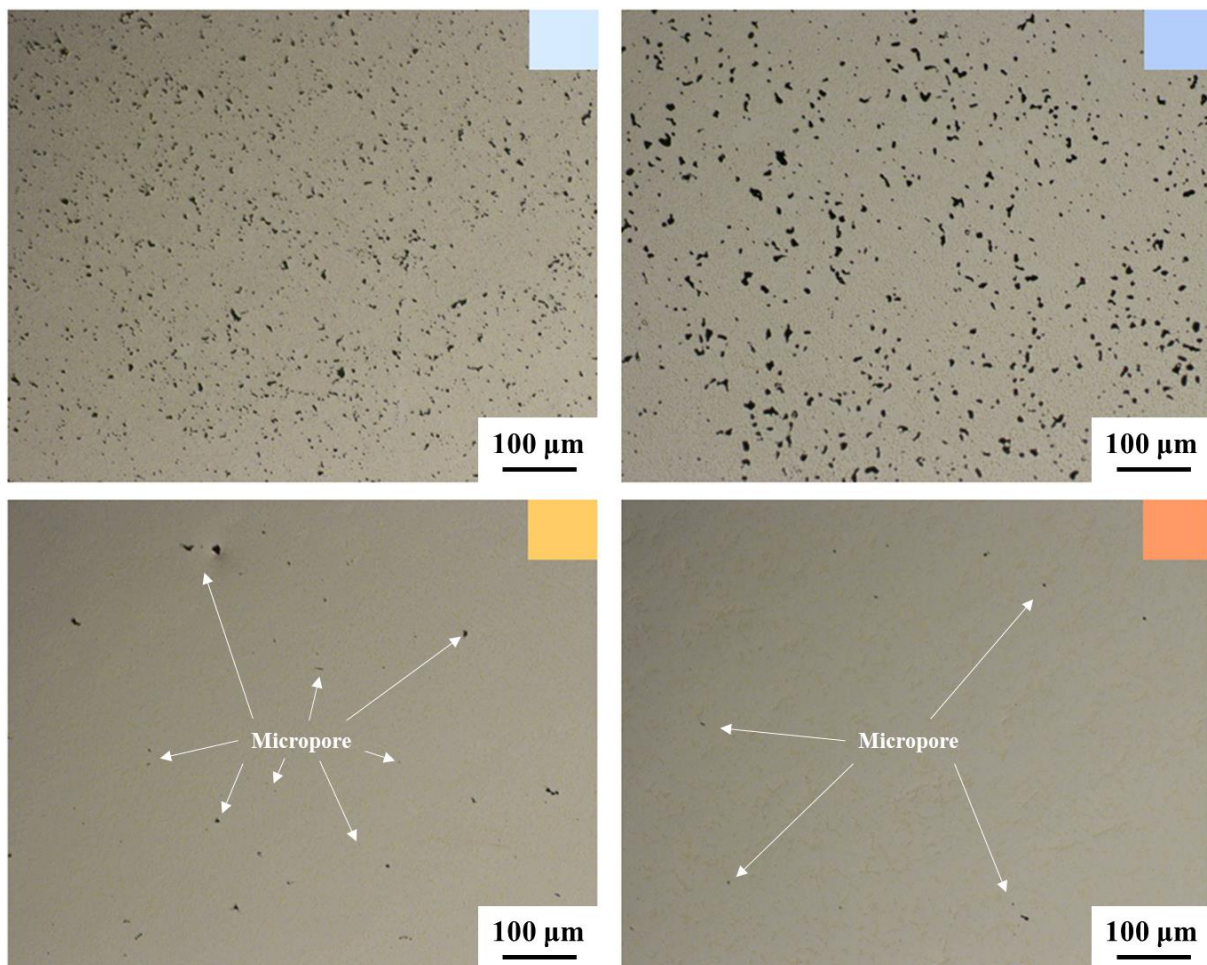


Fig. 59. Porosity distribution for (light blue) equiatomic and (dark blue) equimassic TNZT mechanical alloying by powder metallurgy, and (light orange) equiatomic and (dark orange) equimassic TNZT mechanical alloying by powder metallurgy and casting.

From the results mentioned above, the large variability of the data concerning the porosity of the casting samples stands out. But it can be explained by the following fact. During the cutting of the casting samples, the formation of a macropore was observed in the central area of the sample, as shown in **Fig. 60**. It has been produced undoubtedly by a large gas bubble that could not come to the sample surface during the casting process.



Fig. 60. *Macropore in the TNZT casting sample.*

4.2.2. Crystallographic phase distribution

In order to observe the phases, a chemical etching was performed. As shown in **Fig. 61**, two phases with dark and light grey contrast were observed.

However, special attention must be paid to the engraved images because, in addition to the presence of pores that can create confusion, depending on the engraving time, burnt areas can be obtained due to an excessive exposure time.

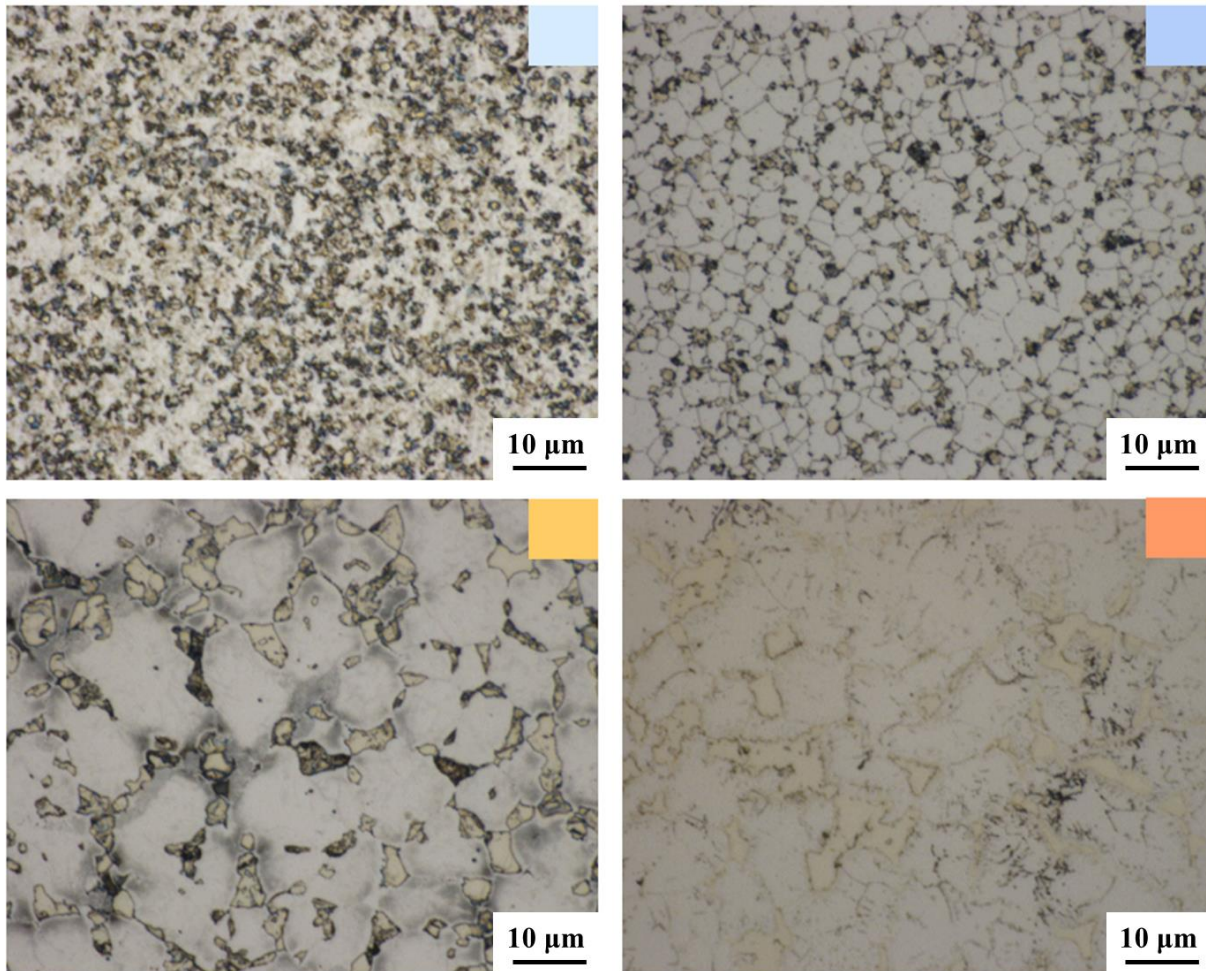


Fig. 61. Acid etching for (light blue) equiatomic and (blue) equimassic TNZT mechanical alloying by powder metallurgy, and (yellow) equiatomic and (orange) equimassic TNZT mechanical alloying by powder metallurgy and casting.

4.2.3. Chemical distribution throughout the phases

Once the number of existing phases had been determined, it was necessary to define the chemical composition of each one. As explained above, special care must be taken with conventional powder metallurgy samples, as they are more porous than the casting ones and this porosity could be mistaken for one of the phases. This is due to the grey scale image obtained by FESEM. Therefore, it is clear that the two phases mentioned are the light and the dark areas.

As for the alloys obtained by conventional powder metallurgy, observing the results of the mapping analyses, the scarce diffusion of Zr and Ta in both cases, equiatomic and equimassic, stands out. In the equiatomic case (**Fig. 62**), Ti and Nb are more evenly distributed in both

phases. While in the equimassic case (**Fig. 63**), Ti is less distributed in the analysis area as it is accompanied by Ta, and Nb is homogeneously distributed in both phases.

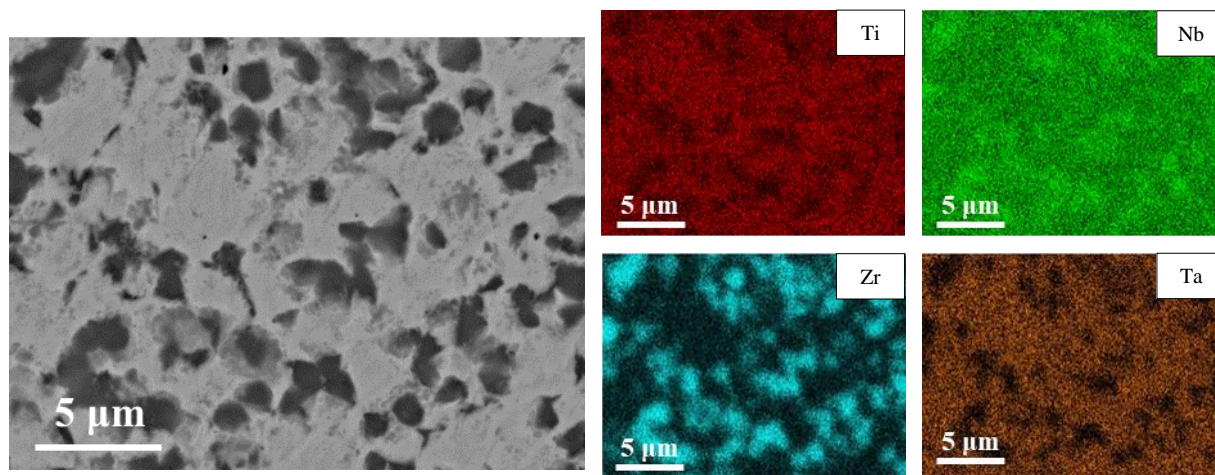


Fig. 62. Element mapping by FESEM for equiatomic TNZT mechanical alloying by powder metallurgy.

Table 22 shows the values associated with **Fig. 62** analysis.

Table 22. Analysis of the overall composition and light and dark areas of the element mapping by FESEM for equiatomic TNZT mechanical alloying sample by powder metallurgy.

Element	Overall		Light areas		Dark areas	
	Wt. (%)	At.(%)	Wt. (%)	At.(%)	Wt. (%)	At.(%)
Ti	11.1	23.6	12.7	28.2	7.0	13.2
Nb	19.4	21.3	24.8	28.4	5.7	5.6
Zr	28.8	32.2	11.3	13.2	76.4	75.8
Ta	40.6	21.3	51.2	30.2	10.9	5.5

From the general mapping of the alloy, a somewhat different atomic composition than theoretically expected has been obtained. In particular, the amount of Zr has been increased, which supports the low diffusion of this element. However, by analysing only a small area, it is not possible to extrapolate this general composition to the whole alloy. Nevertheless, the difference between the compositional percentage of Zr and Ta according to the type of analysed area, light or dark, is quite huge. As expected, the area where the amount of Ta is

clearer than that whose composition in Zr is higher and it is related to the unit weight of elements, with Ta being heavier than Zr. This compositional trend is also found in the following alloy.

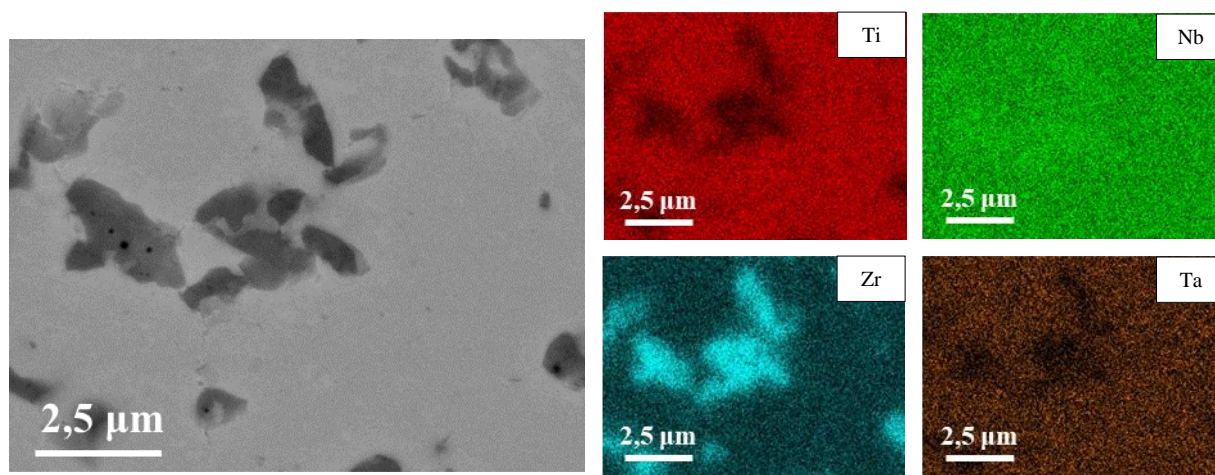


Fig. 63. Element mapping by FESEM for equimassic TNZT mechanical alloying by powder metallurgy.

Table 23 shows the values associated with **Fig. 63** analysis.

Table 23. Analysis of the overall composition and light and dark areas of the element mapping by FESEM for equimassic TNZT mechanical alloy sample by powder metallurgy.

Element	Overall		Light areas		Dark areas	
	Wt. (%)	At.(%)	Wt. (%)	At.(%)	Wt. (%)	At.(%)
Ti	25.5	44.4	28.2	48.7	13.1	23.2
Nb	24.6	22.1	28.1	24.9	7.5	6.9
Zr	23.4	21.4	14.3	13.0	70.3	65.6
Ta	26.4	12.2	29.4	13.4	9.0	4.3

As for the casting samples, for both cases, Ta decreases practically to zero when the amount of Zr increases, which translates, along the same lines as for the mechanically alloyed alloys, in that Ta does not diffuse with Zr. Ti and Nb, on the other hand, oscillate around a value and are homogeneously distributed. Below, **Fig. 64** shows this particular analysis for the equiatomic sample.

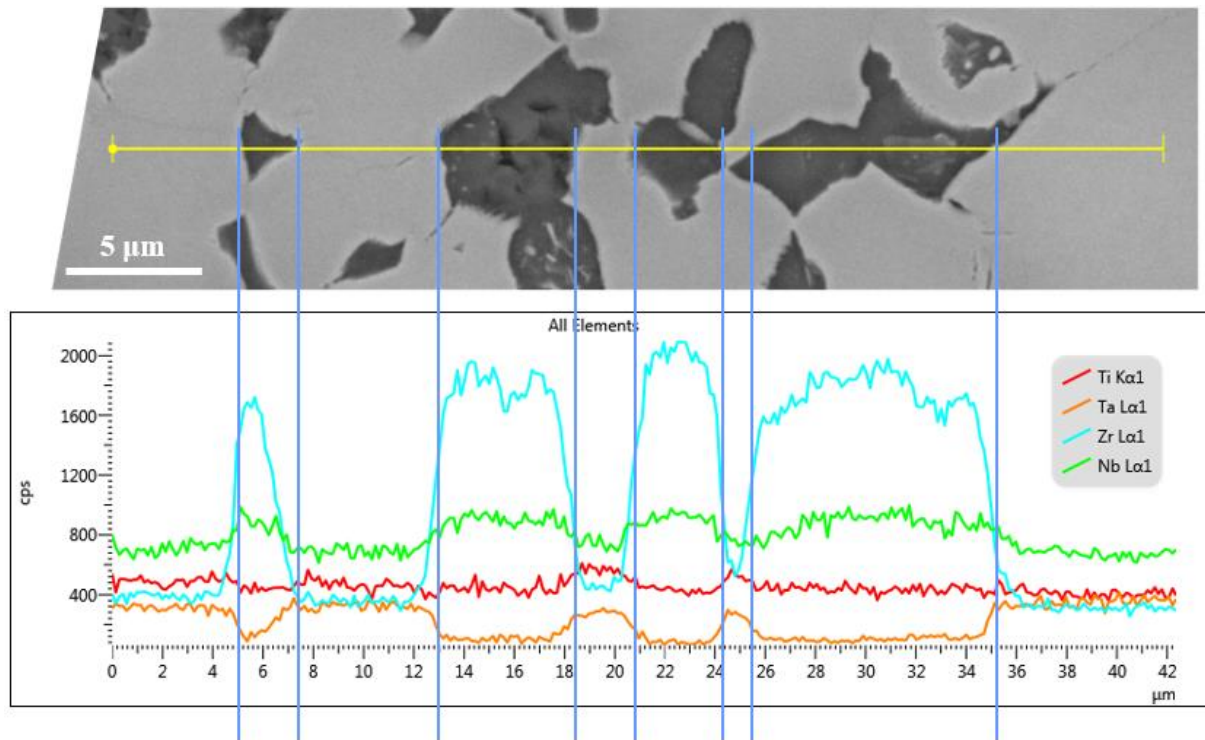


Fig. 64. Element line scanning by FESEM for equiatomic TNZT mechanical alloying by powder metallurgy and casting.

Table 24 shows the values associated with **Fig. 64** qualitatively, as the analyses are not carried out in a specific area, but all sweeps are executed on the yellow line.

Table 24. Analysis of the overall composition and light and dark areas of the element line scanning by FESEM for equiatomic TNZT mechanical alloying by powder metallurgy and casting.

Element	Overall		Light areas		Dark areas	
	Wt. (%)	At.(%)	Wt. (%)	At.(%)	Wt. (%)	At.(%)
Ti	11.4	24.2	12.0	26.8	12.8	23.7
Nb	18.8	20.6	25.2	29.0	8.7	8.3
Zr	29.2	32.5	12.1	14.2	60.8	59.3
Ta	40.5	22.7	50.7	30.0	17.7	8.7

The line mapping done for this case consolidates the results obtained for the other type of manufacturing process. As in the equimassic case shown in **Fig. 65**.

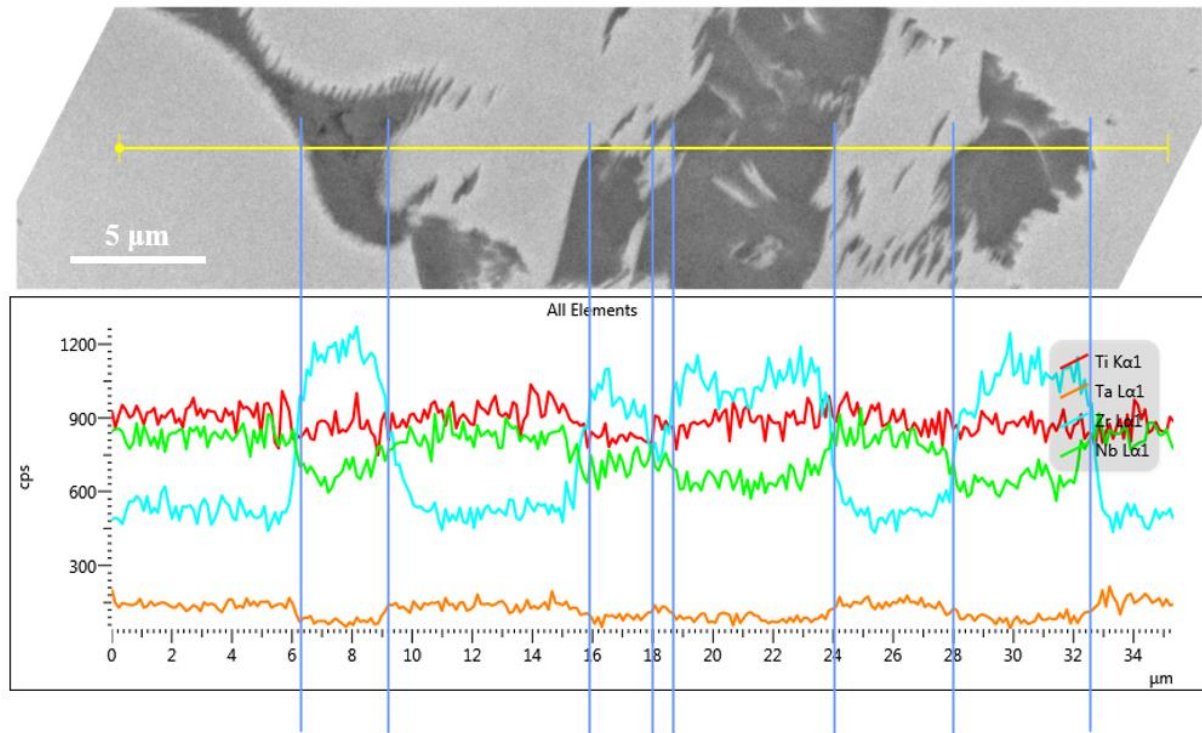


Fig. 65. Element line scanning by FESEM for equimassic TNZT mechanical alloying by powder metallurgy and casting.

Table 25 shows the values associated with Fig. 65 qualitatively, as the analyses are not carried out in a specific area, but all sweeps are executed on the yellow line.

Table 25. Analysis of the overall composition and light and dark areas of the element line scanning by FESEM for equimassic TNZT mechanical alloying by powder metallurgy and casting.

Element	Overall		Light areas		Dark areas	
	Wt. (%)	At.(%)	Wt. (%)	At.(%)	Wt. (%)	At.(%)
Ti	26.5	45.3	22.9	42.1	28.5	47.6
Nb	24.2	21.4	28	26.5	26.4	22.7
Zr	24.6	22.1	15.7	15.2	22.7	19.9
Ta	24.8	11.2	33.4	16.2	22.4	9.9

To sum up, it is clear that the light areas have a higher amount of Ta and the dark ones a higher amount of Zr.

4.2.4. Crystalline structure

By means of X-ray diffraction it was possible to determine the crystalline microstructure belonging to the two phases studied. After analysing the data collected, it was determined that there were two different structures. On the one hand, a BCC similar to that of Ti (β -Ti) (same space group and lattice parameters) together with Nb and Ta, which is the predominant one, and, on the other hand, an FCC associated with Zr (again same space group and lattice parameters). Thus, the light areas seen in the FESEM correspond to BCC-Ti and the darker ones to FCC-Zr.

Fig. 66 shows the representation of the diffractogram obtained for the different alloys, where the microstructure and the crystallographic plane associated to each peak is also detailed.

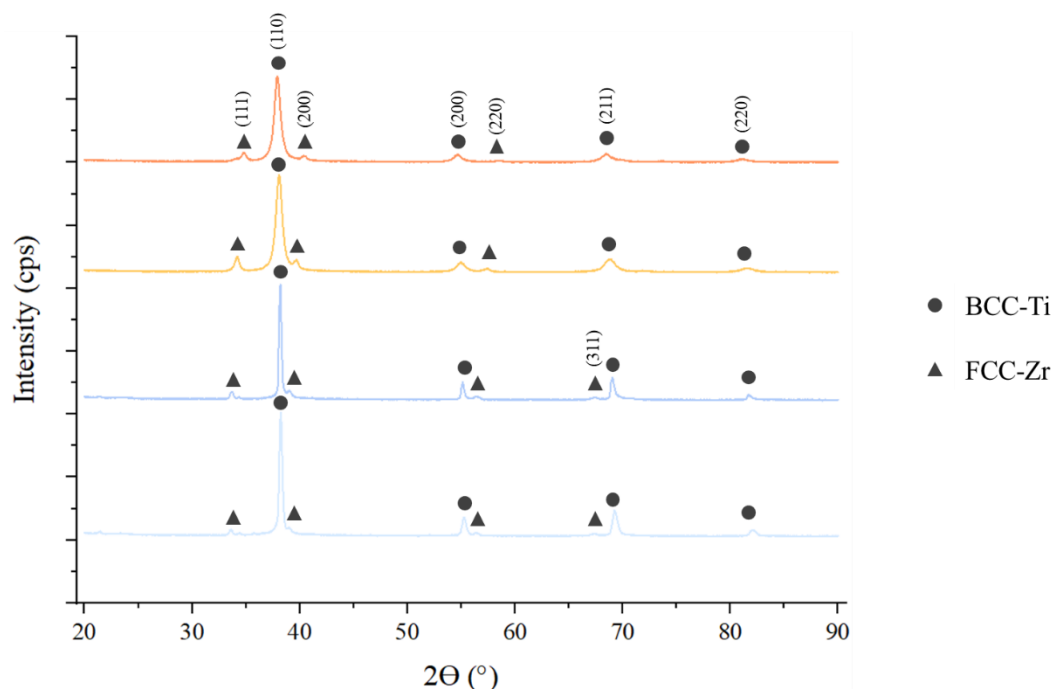


Fig. 66. (■) Equiatomic and (■) equimassic TNZT mechanical alloying by powder metallurgy, and (■) equiatomic and (■) equimassic TNZT mechanical alloying by powder metallurgy and casting XRD that shows crystallographic planes for each diffraction pick according to the distinct phases detailed.

Subsequently, by means of EBSD, the feasibility of the results obtained in X-ray diffraction was studied. **Fig. 67** shows the results obtained, which consolidate the existence of both phases mentioned, as well as their distribution along the samples. In addition, the width of the peaks shows different grain sizes for each alloy, what can be proved in the band contrast figures. In this sense, larger grain sizes are typical of casting, and, in turn, these are larger in equimassic compositions.

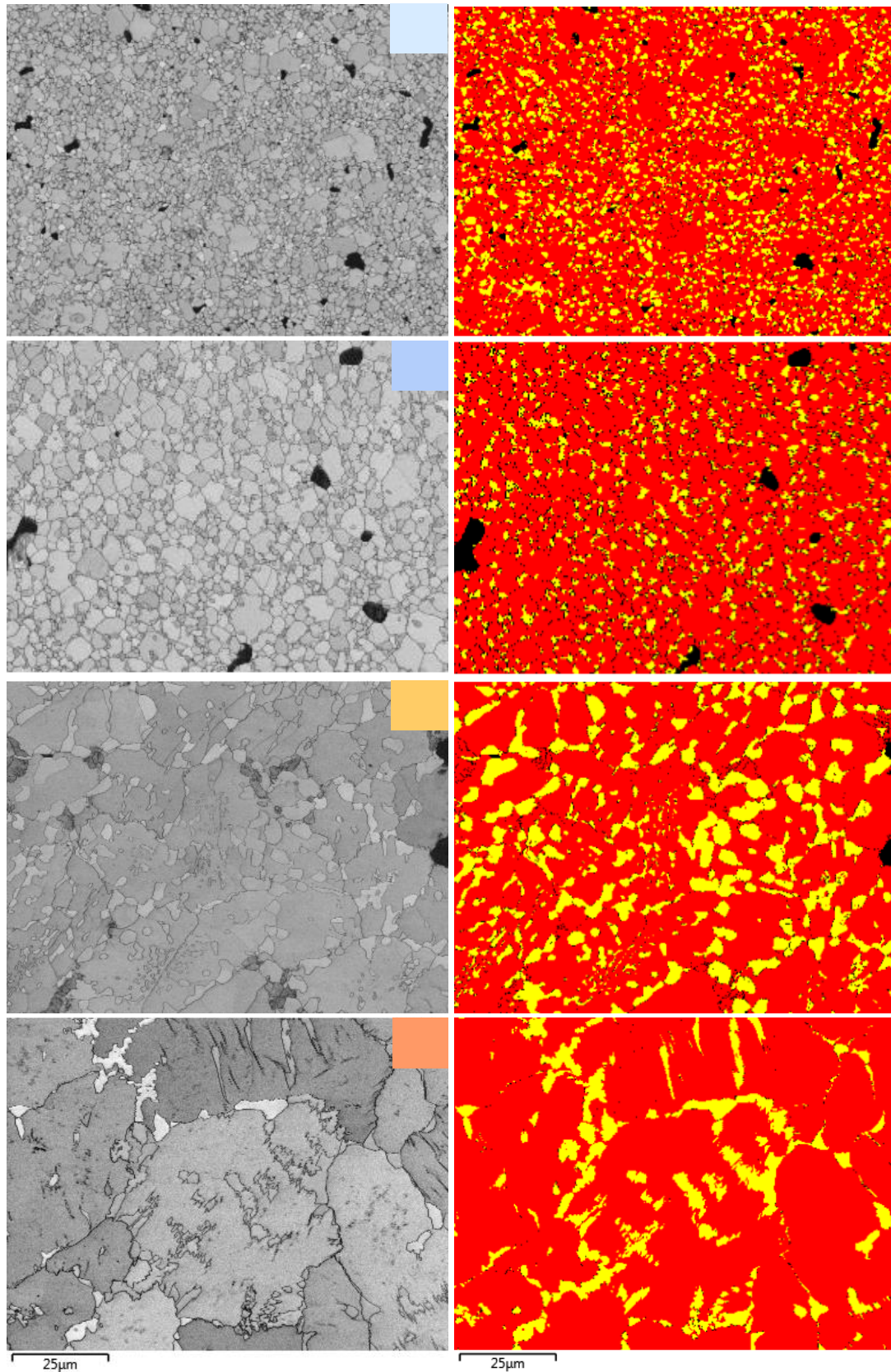


Fig. 67. Band and crystallographic phase contrast by EBSD with the same magnification for (■) equiatomic and (■) equimassive TNZT mechanical alloying by powder metallurgy, and (■) equiatomic and (■) equimassive TNZT mechanical alloying by powder metallurgy and casting, where red represents BCC and yellow FCC.

These differences in grain size are further reflected in **Table 26**, where there are two types of averages, the standard and the weighted area. The first one represents the average when the maximum grain size is dominated by the diameter of the grains that exist in greater number. On the other hand, in the second type the maximum grain size is dominated by the diameter of the largest grains.

Table 26. TNZT MEAs grain size values corresponding to equiatomic and equimassic TNZT mechanical alloying by powder metallurgy, and equiatomic and equimassic TNZT mechanical alloying by powder metallurgy and casting.

Alloy	Min (μm)	Max (μm)	Standard mean (μm)	Area-weighted mean (μm)	Standard deviation (μm)
EA MA PM	1.1*	7.9	1.9	3.0	0.9
EM MA PM	1.4	10.6	3.0	4.6	1.5
EA MA C	1.1*	41.1	3.7	20.5	4.6
EM MA C	1.1*	51.2	5.2	32.9	8.0

* Pixel size.

Using both procedures, XRD and EBSD, the percentage of both phases is similar, as shown in **Table 27**. Nevertheless, XRD shows a volumetric percentage of a biggest area of analysis while EBSD uses a 2D analysis of a smaller area and can therefore be considered less accurate. Specially, if the grain size is larger, as the number of grains analysed is smaller.

Table 27. TNZT MEAs comparison of the microstructure type percentage for XRD and EBSD for equiatomic and equimassic TNZT mechanical alloying by powder metallurgy, and equiatomic and equimassic TNZT mechanical alloying by powder metallurgy and casting.

Alloy	XRD		EBSD	
	%BCC	%FCC	%BCC	%FCC
EA MA PM	74.60	25.40	80.15	19.85
EM MA PM	85.45	14.55	86.07	13.93
EA MA C	87.86	12.14	76.67	23.33
EM MA C	94.32	5.68	86.81	13.18

As mentioned above, in order to corroborate the existence of these two phases, it has been necessary to resort to TEM. Thus, despite its great difficulty, it turns out to be a key tool for the complete identification of the alloy's microstructure.

After selecting several analysis zones, EDS is performed on them and, subsequently, each of the detected phases is analysed in detail. **Fig. 68** shows the element mapping for the EA MA PM sample, where one of the phases is observed to be rich in Ti, Nb and Ta, while the other one is rich in Zr.

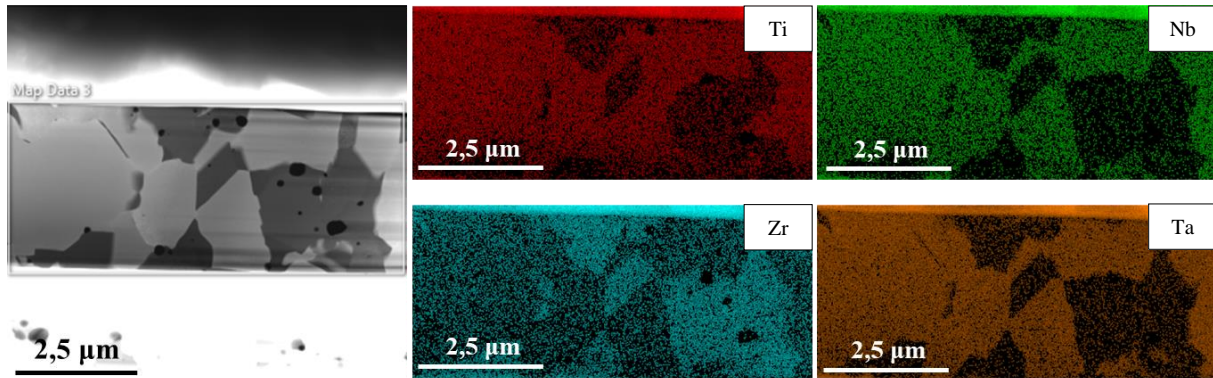


Fig. 68. Element mapping by TEM for equiatomic TNZT mechanical alloying by powder metallurgy.

In addition, electron diffraction was performed on each of these phases. For the Ti-Nb-Ta rich phase a BCC cell is found (**Fig. 69**) while for the Zr-rich phase a FCC pattern is obtained (**Fig. 70**).

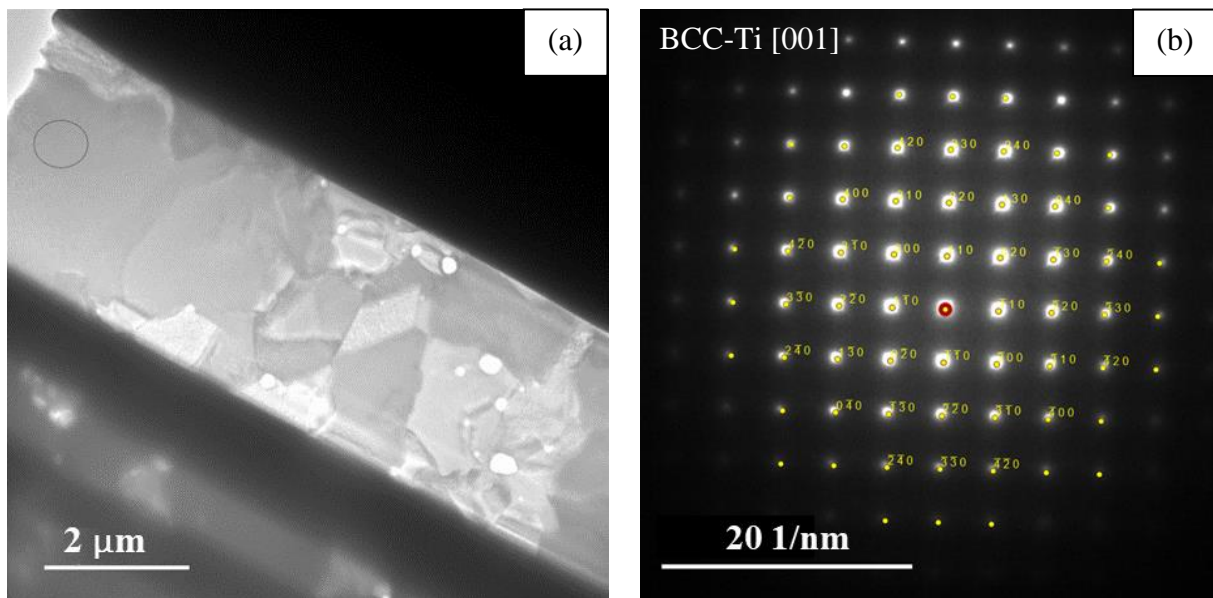


Fig. 69. Electron diffraction of a Ti-Nb-Ta-rich TNZT zone that confirms the presence of a BCC microstructure in the equiatomic TNZT mechanical alloying by powder metallurgy, [001] zone axis: (a) selected area diffraction (SAD), (b) diffraction pattern.

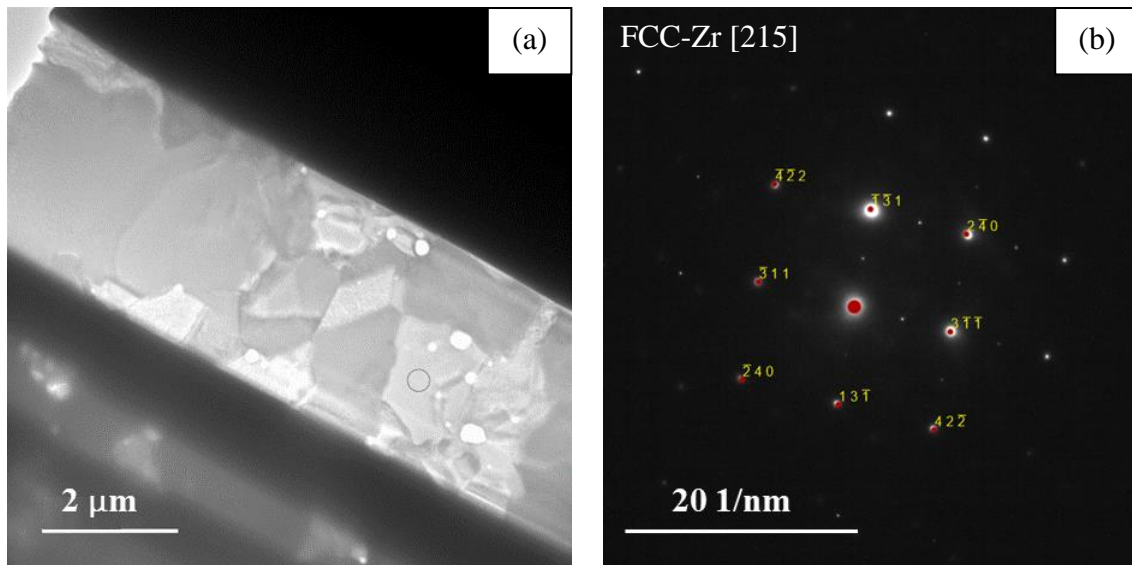


Fig. 70. Electron diffraction of a Zr-rich TNZT zone Zr that confirms the presence of a FCC microstructure in the equiatomic TNZT mechanical alloying by powder metallurgy, [215] zone axis: (a) selected area diffraction (SAD), (b) diffraction pattern.

In both cases, the selected area diffraction is referenced by a grey circle. The same was done for the melting samples. In the specific case of the equiatomic alloy, two different areas were studied. Here, the existence of both phases and their relationship to their chemical composition could also be verified.

Ti-Nb-Ta-rich phase was studied in **Fig. 71**, while Zr-rich phase was analysed in **Fig. 73**. Thereby, BCC (**Fig. 72**) and FCC (**Fig. 74**) pattern were respectively identified.

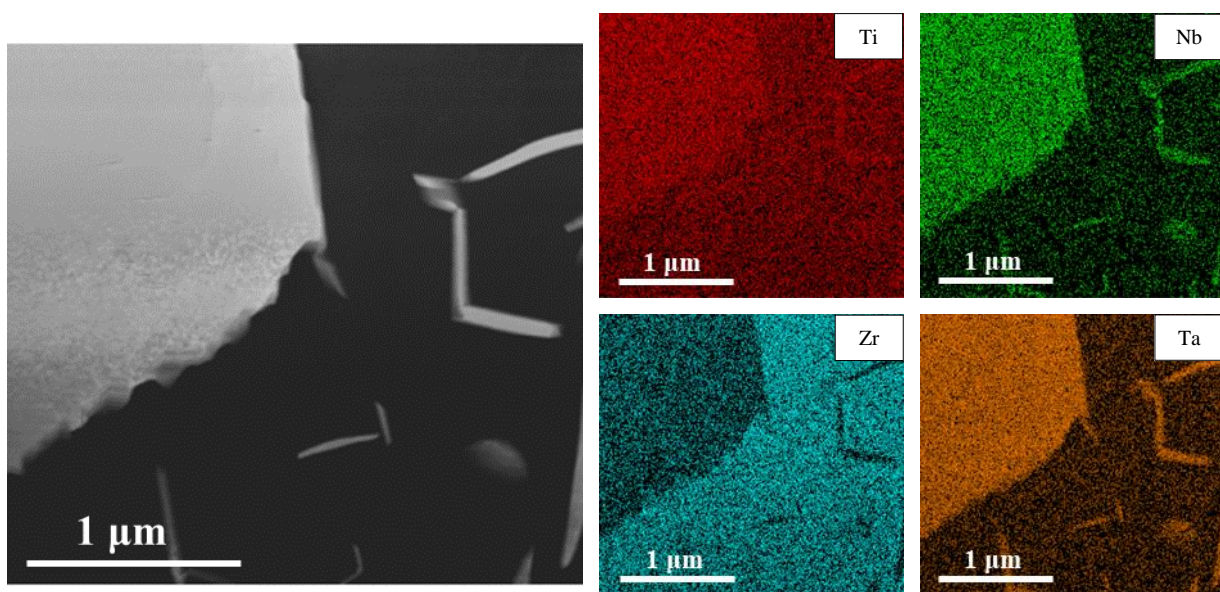


Fig. 71. Element mapping by TEM for equiatomic TNZT mechanical alloying by powder metallurgy and casting (zone I).

As can be seen, the first SAD has a higher concentration of Ti, Nb, and Ta. When observing its diffraction pattern, a grid of dots forming perpendicular lines can be appreciated. This is indeed the main characteristic of a BCC pattern.

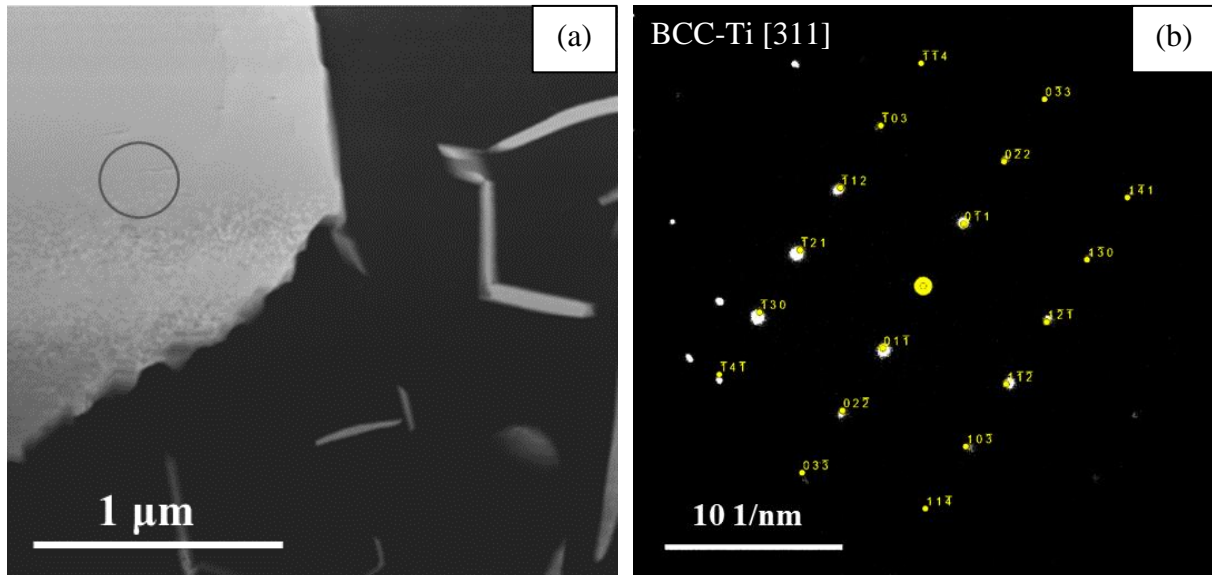


Fig. 72. Electron diffraction of a Ti-Nb-Ta-rich TNZT zone that confirms the presence of a BCC microstructure in the equiatomic TNZT mechanical alloying by powder metallurgy and casting, [311] zone axis: (a) selected area diffraction (SAD), (b) diffraction pattern.

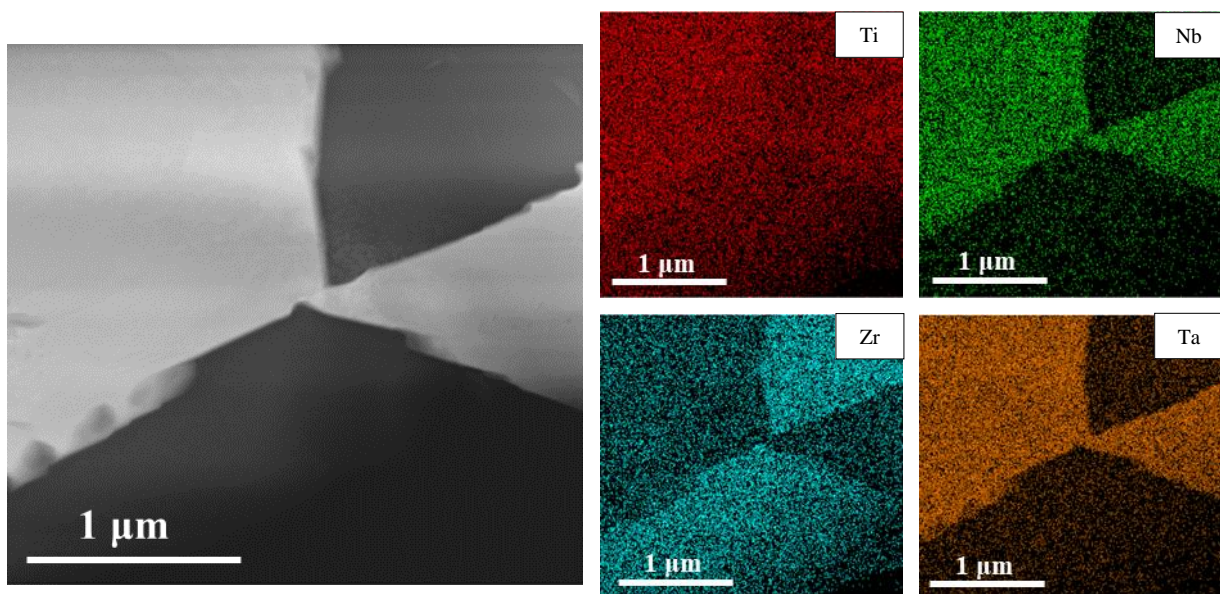


Fig. 73. Element mapping by TEM for equiatomic TNZT mechanical alloying by powder metallurgy and casting (zone 2).

At the second SAD, there is much concentration of Zr and the FCC pattern, in contrast to the BCC one, is composed by dots forming concentric hexagons around the same point.

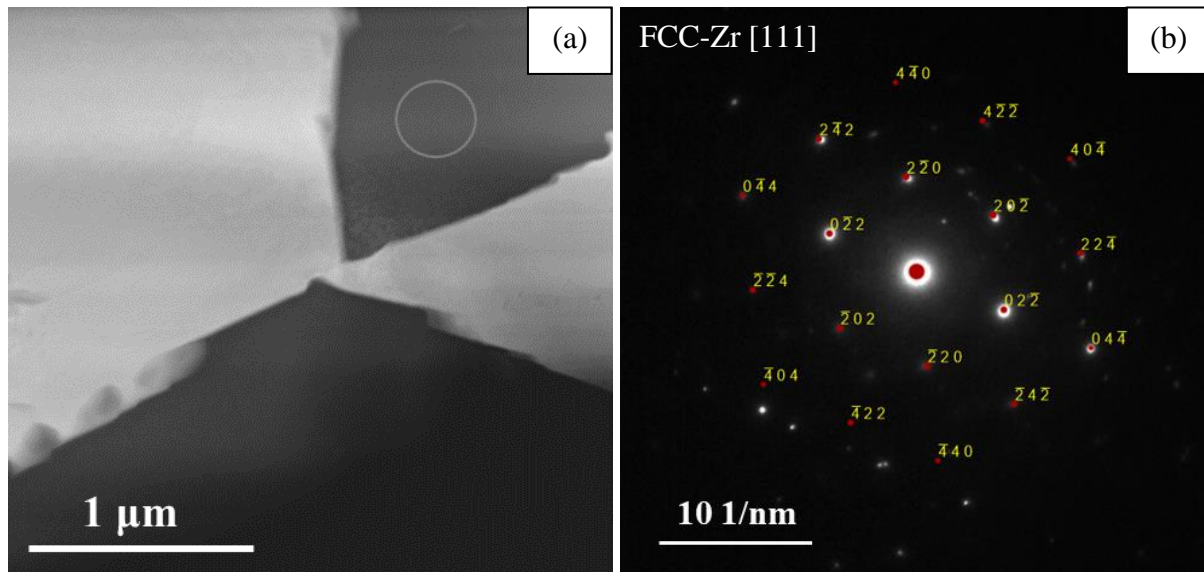


Fig. 74. Electron diffraction of a Zr-rich TNZT zone Zr that confirms the presence of a FCC microstructure in the equiatomic TNZT mechanical alloying by powder metallurgy and casting, $[111]$ zone axis: (a) selected area diffraction (SAD), (b) diffraction pattern.

Based on the above, Ti-Nb-Ta-rich BCC and Zr-rich FCC phases were both fully identified, chemically and structurally.

4.2.5. Crystallographic orientation

As for the crystallographic orientation of the grains, **Fig. 75** shows the inverse polar figures in the Z-direction, where no predominant texture is observed in the materials. Specifically for casting samples, where grain size is much higher than in those only manufactured by conventional powder metallurgy, the number of grains analysed in the area is not much and it is hard to determine the orientation behaviour of the hole alloy. Nevertheless, since the colour of the IPF-Z is such different, this lack of texture can be established.

Furthermore, in the melted samples some small grains were formed within the larger ones, which is the result of the limitation associated with melting due to the disparity of melting temperatures. These have the characteristic that all those within the same grain have the same colouring, which means that they have the same crystalline orientation. Looking at **Fig. 67**, it can be seen that these small grains have an FCC structure while the surrounding grain has a BCC structure. It is conventionally known as a crystallographic orientation relationship (OR).

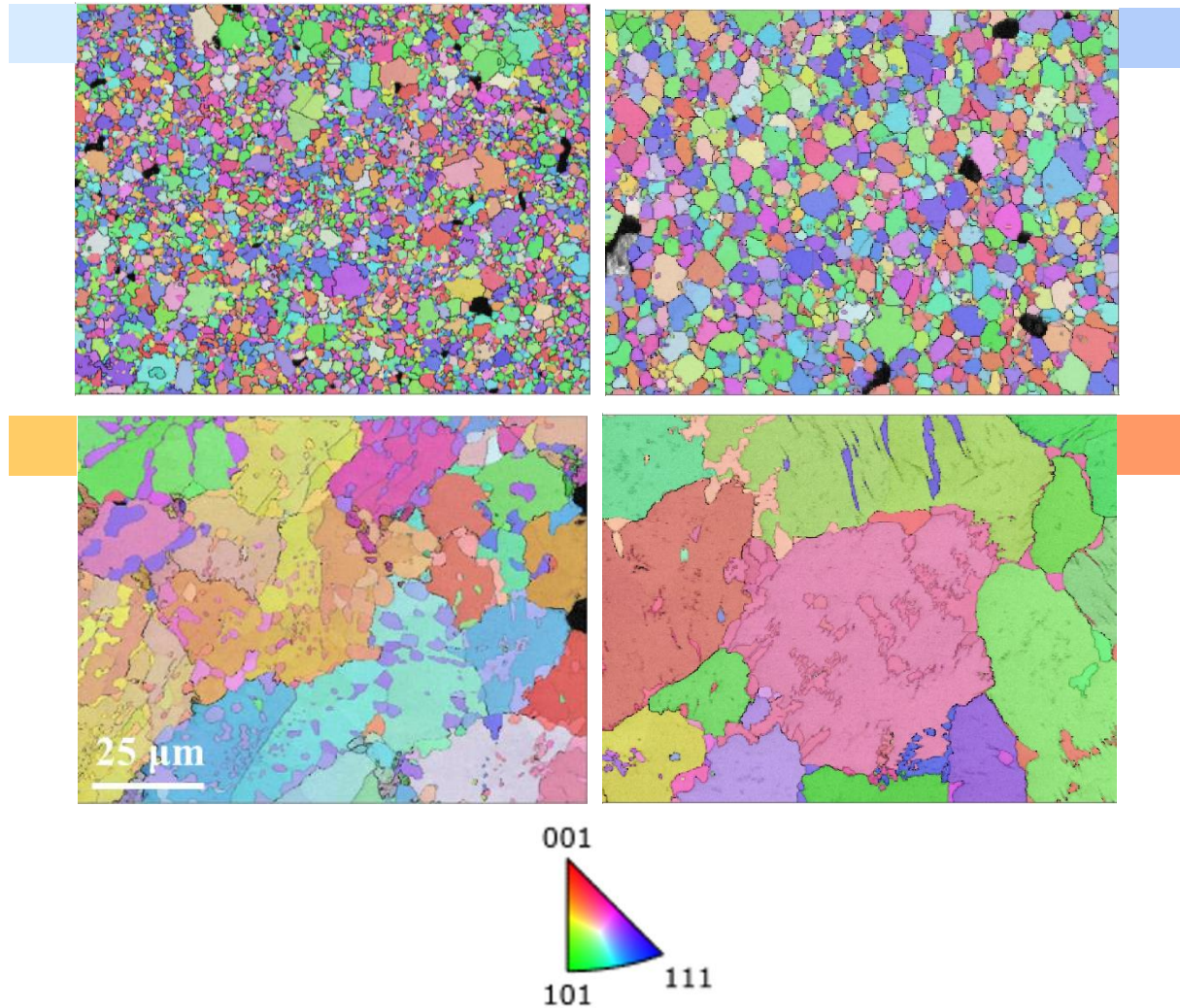


Fig. 75. Inverse polar figures with same magnification of the crystalline orientation in the *z*-direction (IPF-Z) for (□) equitomic and (□) equimassic TNZT mechanical alloying by powder metallurgy, and (□) equitomic and (□) equimassic TNZT mechanical alloying by powder metallurgy and casting.

This OR between the FCC and BCC phases is defined by the Pitsch ratio, detailed in **Table 28**. In addition, **Fig. 76** shows, in red, the grain boundaries that fulfil this relationship.

Table 28. Pitsch crystallographic orientation relationship (OR).

OR	BCC		FCC	
	Plane	Direction	Plane	Direction
Pitsch	{010}	<101>	{101}	<111>

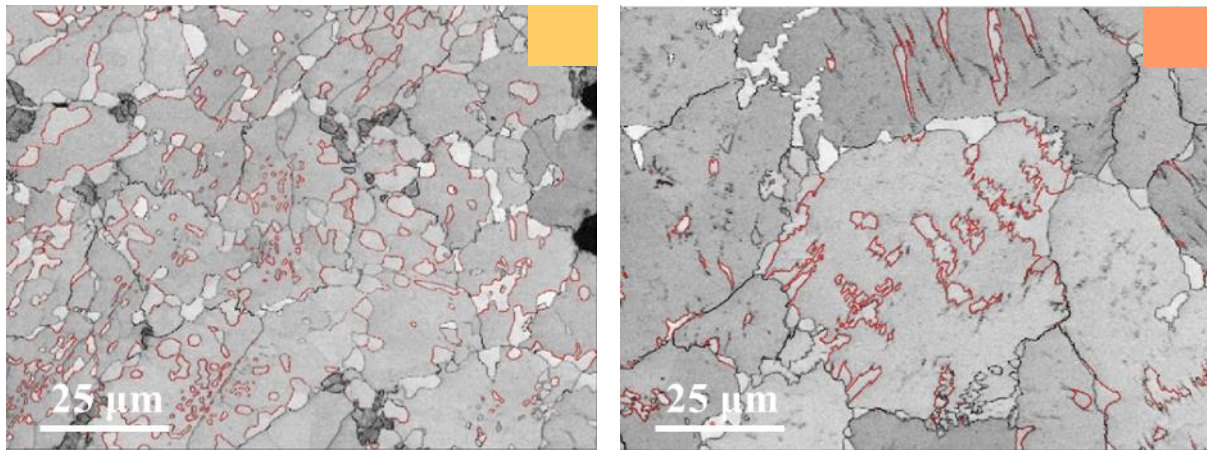


Fig. 76. Pitsch crystallographic orientation relationship for (■) equiatomic and (■) equimassic TNZT mechanical alloying by powder metallurgy and casting.

After completing the microstructural characterisation of the alloys, the influence of the phases found is studied on the mechanical behaviour of the alloys, firstly, and on the chemical behaviour, secondly.

4.3. MECHANICAL CHARACTERISATION

Depending on the amount of sample obtained for each alloy and the brittleness of these ones, mechanical characterisation was carried out using hardness, microhardness, 4-point bending, micro-tensile, micro-compression, and small-punch tests. Thus, there are some tests that could not be carried out for all the alloys, as detailed in **Table 29**.

Table 29. Tests for TNZT MEA mechanical characterisation: (a) hardness, (b) microhardness, (c) determination of elastic modulus by ultrasounds, (d) 4-point bending, (e) micro-tensile (f) micro-compression, and (g) small punch. Specifically, for equiatomic and equimassic mechanical alloying by powder metallurgy (EA MA PM, EM MA PM), and equiatomic and equimassic mechanical alloying by powder metallurgy and casting (EA MA C, EM MA C).

Alloy	(a)	(b)	(c)	(d)	(e)	(f)	(g)
EA MA PM	■	■	■	■	■	■	■
EM MA PM	■	■	■	■	■	■	■
EA MA C	■	■	■	■	■	■	■
EM MA C	■	■	■	■	■	■	■

4.3.1. Hardness

In terms of hardness, casting samples have the highest values. However, in mechanical alloying by powder metallurgy, the equimassic alloy has a higher hardness than the equiatomic one. In casting, the opposite is true, and it is the equimassic alloy has the higher value. This can be seen in **Fig. 77**.

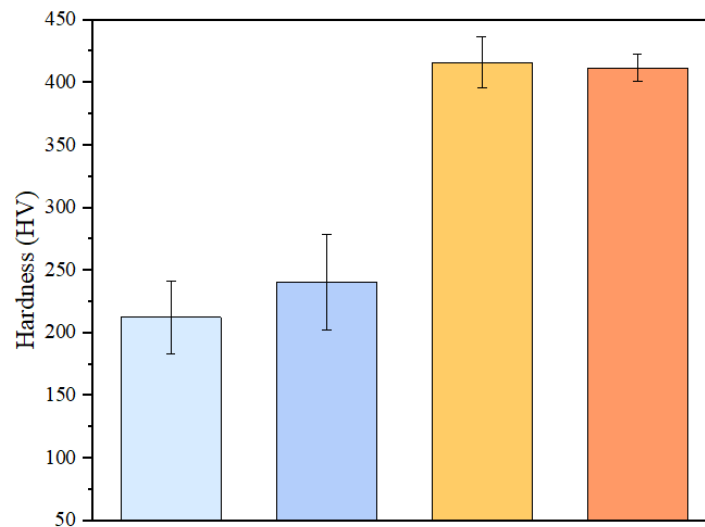


Fig. 77. Hardness results for (light blue) equiatomic and (medium blue) equimassic TNZT mechanical alloying by powder metallurgy, and (yellow) equiatomic and (orange) equimassic TNZT mechanical alloying by powder metallurgy and casting.

Table 30 shows the values associated with **Fig. 77**.

Table 30. Hardness results for equiatomic and equimassic TNZT mechanical alloying by powder metallurgy (EA MA PM, EM MA PM), and equiatomic and equimassic TNZT mechanical alloying by powder metallurgy and casting (EA MA C, EM MA C).

Alloy	Hardness (HV)	± Error
EA MA PM	212.500	29.340
EM MA PM	240.570	38.500
EA MA C	416.053	20.558
EM MA C	411.672	11.045

In this way, not only has the hardness of the alloys been measured in broad strokes, where porosity is most likely to be found, but with microhardness measurements, more rigorous results could be obtained.

4.3.2. Microhardness

On the other hand, microhardness gives much higher values than hardness (**Fig. 78**). However, it confirms the trend observed earlier in the hardness tests.

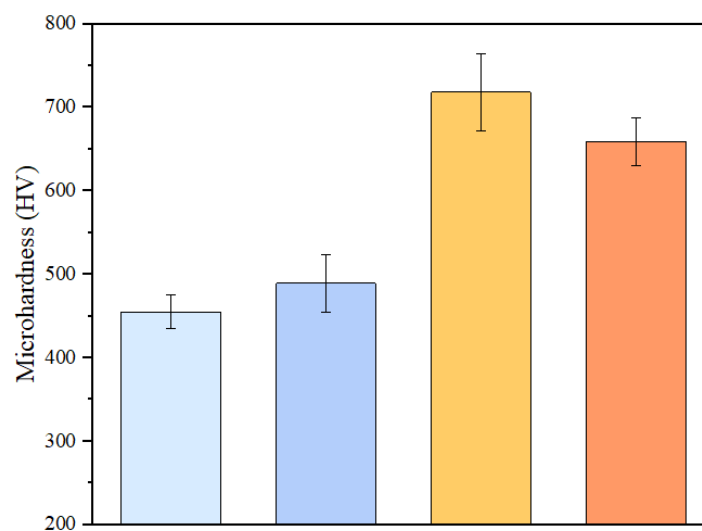


Fig. 78. Microhardness results for (light blue) equiatomic and (medium blue) equimassic TNZT mechanical alloying by powder metallurgy, and (yellow) equiatomic and (orange) equimassic TNZT mechanical alloying by powder metallurgy and casting.

Table 31 shows the values associated with **Fig. 78**.

Table 31. Microhardness results for equiatomic and equimassic TNZT mechanical alloying by powder metallurgy (EA MA PM, EM MA PM), and equiatomic and equimassic TNZT mechanical alloying by powder metallurgy and casting (EA MA C, EM MA C).

Alloy	Microhardness (HV)	± Error
EA MA PM	455.180	20.680
EM MA PM	489.080	35.010
EA MA C	718.360	46.140
EM MA C	658.920	28.430

In addition to hardness or microhardness, other parameters such as the elastic modulus, which can be determined by different techniques, are very important in a mechanical characterisation.

4.3.3. Determination of elastic modulus by ultrasounds

The determination of the elastic modulus by ultrasounds is influenced not only by the alloy elements, but also by the microstructure, among other aspects. Thus, the elastic modulus for the study alloys is shown in **Fig. 79**, where no clear trend is discernible.

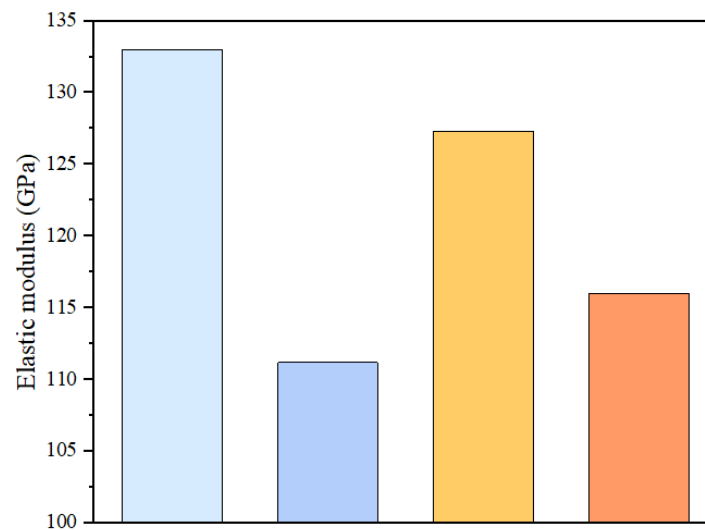


Fig. 79. Elastic modulus results for (□) equiatomic and (□) equimassic TNZT mechanical alloying by powder metallurgy, and (□) equiatomic and (□) equimassic TNZT mechanical alloying by powder metallurgy and casting.

Table 32 shows the values associated with **Fig. 79**.

Table 32. Elastic modulus of TNZT MEA for equiatomic and equimassic mechanical alloying by powder metallurgy (EA MA PM, EM MA PM), and equiatomic and equimassic mechanical alloying by powder metallurgy and casting (EA MA C, EM MA C).

Alloy	PM	C
EA MA	133.006	127.293
EM MA	111.174	115.983

4.3.4. 4-Point bending, micro-tensile, and micro-compression tests

4-point bending, micro-tensile, and micro-compression tests were found to provide information about the behaviour of the samples under different stresses, which is illustrated in **Fig. 80**.

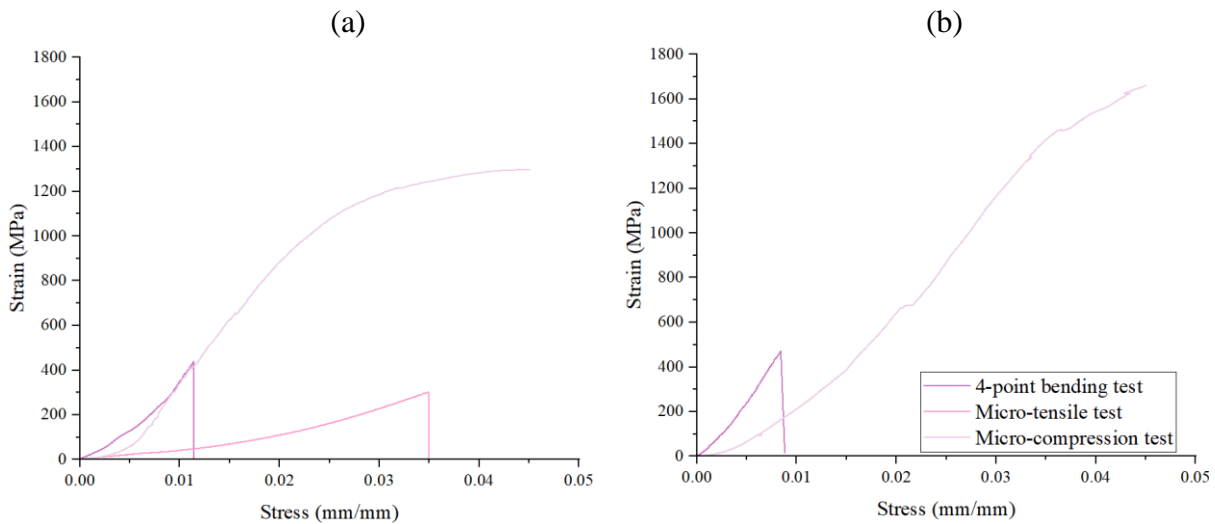


Fig. 80. (a) Equiatomic and (b) equimassic TNZT mechanical alloying behaviour by powder metallurgy.

Specifically, for 4-point bending test, results are given by **Table 33**. For the case of micro-tensile test, **Table 34** collects the results. However, the EM MA PM sample was broken during milling operation, demonstrating its poor machinability.

Table 33. 4-Point bending test results for equiatomic and equimassic TNZT mechanical alloying by powder metallurgy (EA MA PM, EM MA PM).

Alloy	4-Point bending elastic modulus	Ultimate strength	Elongation capability
EA MA PM	44.375 ± 4.183	458.337 ± 26.500	0.933 ± 0.004
EM MA PM	66.399 ± 0.881	544.098 ± 137.812	0.728 ± 0.020

Table 34. Micro-tensile test results for equiatomic and equimassic TNZT mechanical alloying by powder metallurgy (EA MA PM, EM MA PM).

Alloy	Micro-tensile elastic modulus	Ultimate strength	Elongation capability
EA MA PM	8.743 ± 3.489	294.154 ± 10.880	0.402 ± 0.173
EM MA PM	-	-	-

Finally, **Table 35** exhibits the results of the micro-compression test.

Table 35. *Micro-compression test results for equiatomic and equimassic TNZT mechanical alloying by powder metallurgy (EA MA PM, EM MA PM).*

Alloy	Micro-compression elastic modulus	Ultimate strength ^(*)	Elongation
EA MA PM	41.845 ± 25.234	1,053.939 ± 346.951	-
EM MA PM	50.233 ± 10.150	1,320.656 ± 396.376	-

^(*) *Note.* Technically, there ultimate strength is not found for micro-compression because of the tooling deformation. However, strength values stabilised during that time so it can be considered that way.

During it, some problems appeared. In this regard, during the test of the first specimen, a large ductile behaviour together with a huge elongation was observed. In the end, it was decided to suspend the test as the fracture did not occur. It should be noted that in the case of the micro-compression tests, it was not possible to determine the elongation produced during the test because, due to the high hardness of the specimens, the tooling was deformed. In addition, as mentioned above in chapter **3.3.5. 4-Point bending, micro-tensile, and micro-compression tests**, only one sample did not explode. And as a consequence, it was not possible to measure the height after the test to calculate the elongation provided. **Fig. 81** is the shape of the tooling after testing.

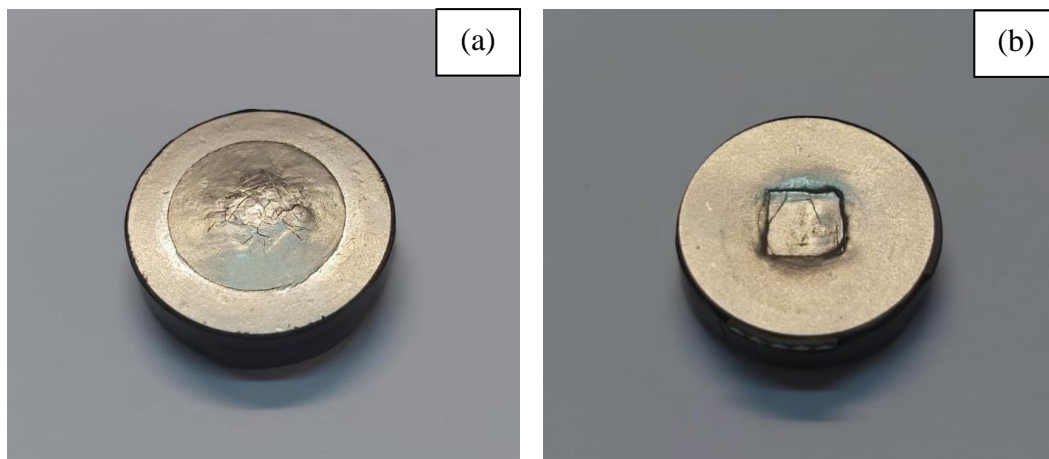
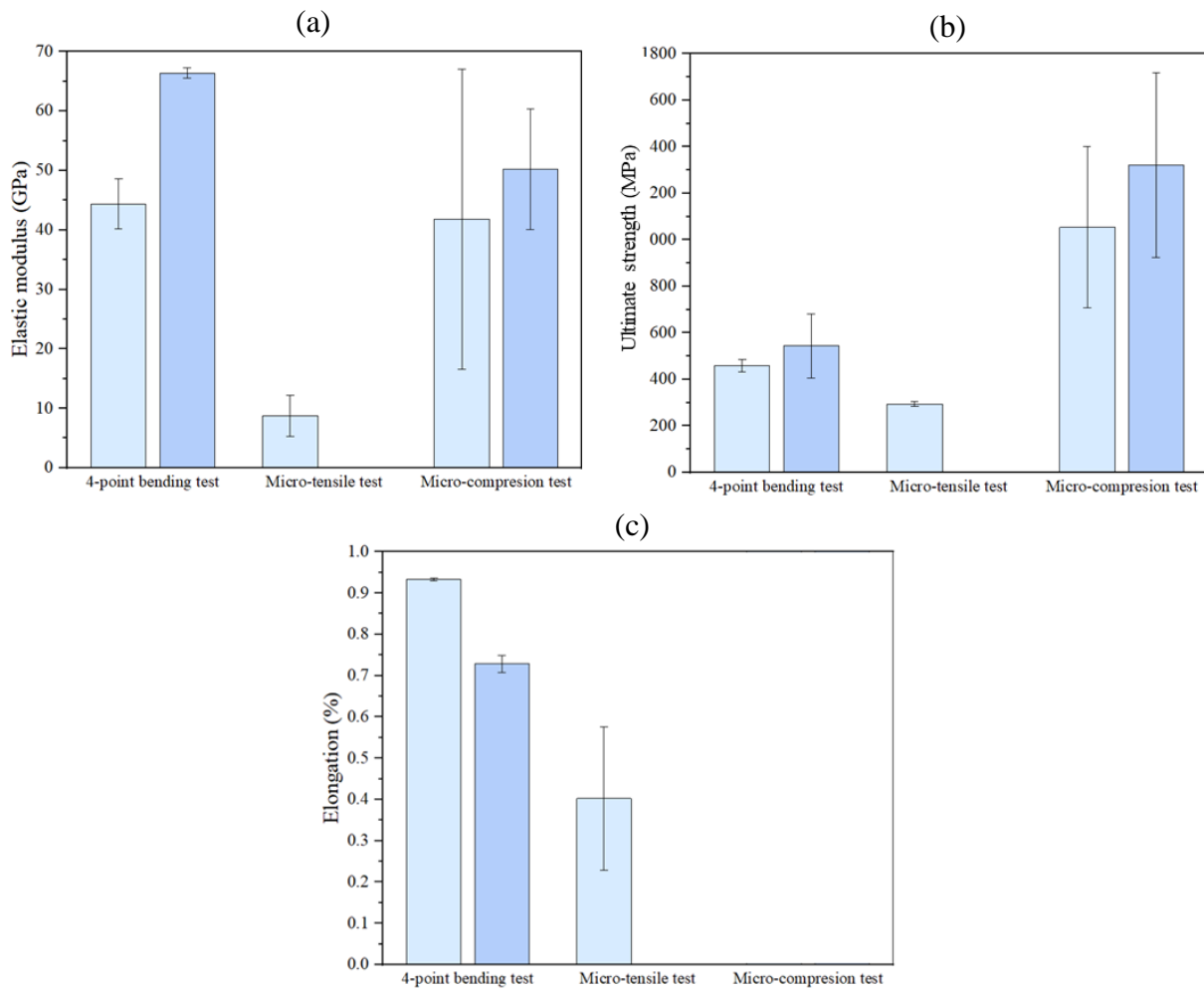


Fig. 81. *Micro-compression tooling deformation after testing: (a) top and (b) bottom.*

To end with, all the results are put together in a joint graph, so that a general notion of these alloys behaviour can be reached, in the absence of small punch test realisation.



Note. There is no equimassive sample for micro-tensile testing because of its fragility and lack of machinability, it broke. In addition, it was not possible to measure the elongation provided by micro-compression test because, except for one, the samples exploded.

Fig. 82. Comparison between principal test parameters for (□) equiatomic and (■) equimassive TNZT mechanical alloying by powder metallurgy: (a) elastic modulus, (b) ultimate strength, and (c) elongation.

4.3.5. Small-punch test

After data treatment as explained in **Fig. 45**, small-punch most important parameters results are collected in **Table 36**. In addition, to be willing to understand that results, they are represented in **Fig. 83**.

From the results presented, the great variability associated with them stands out, as no pattern was observed in the behaviour of the samples during the tests. Indeed, some showed a fully elastic slope, while others also presented a plastic slope.

Table 36. Small punch results for equiatomic and equimassic TNZT mechanical alloying by powder metallurgy (EA MA PM, EM MA PM), and equiatomic and equimassic TNZT mechanical alloying by powder metallurgy and casting (EA MA C, EM MA C).

Alloy	Elastic slope (N/mm)	Plastic slope (N/mm)	Maximum force (N)	First breakage (N)
EA MA PM	2,643.448 ± 1,704.577	1,742.203 ± 1,541.203	251.873 ± 158.797	221.609 ± 124.948
EM MA PM	2,477.085 ± 1,329.758	634.100 ± 322.539	247.637 ± 76.095	203.944 ± 80.006
EA MA C	2,450.060 ± 746.077	1,525.050 ± 203.859	283.130 ± 160.951	114.000 ± 19.812
EM MA C	1,115.188 ± 366.441	315.735 ± 239.264	125.465 ± 63.614	100.696 ± 68.211

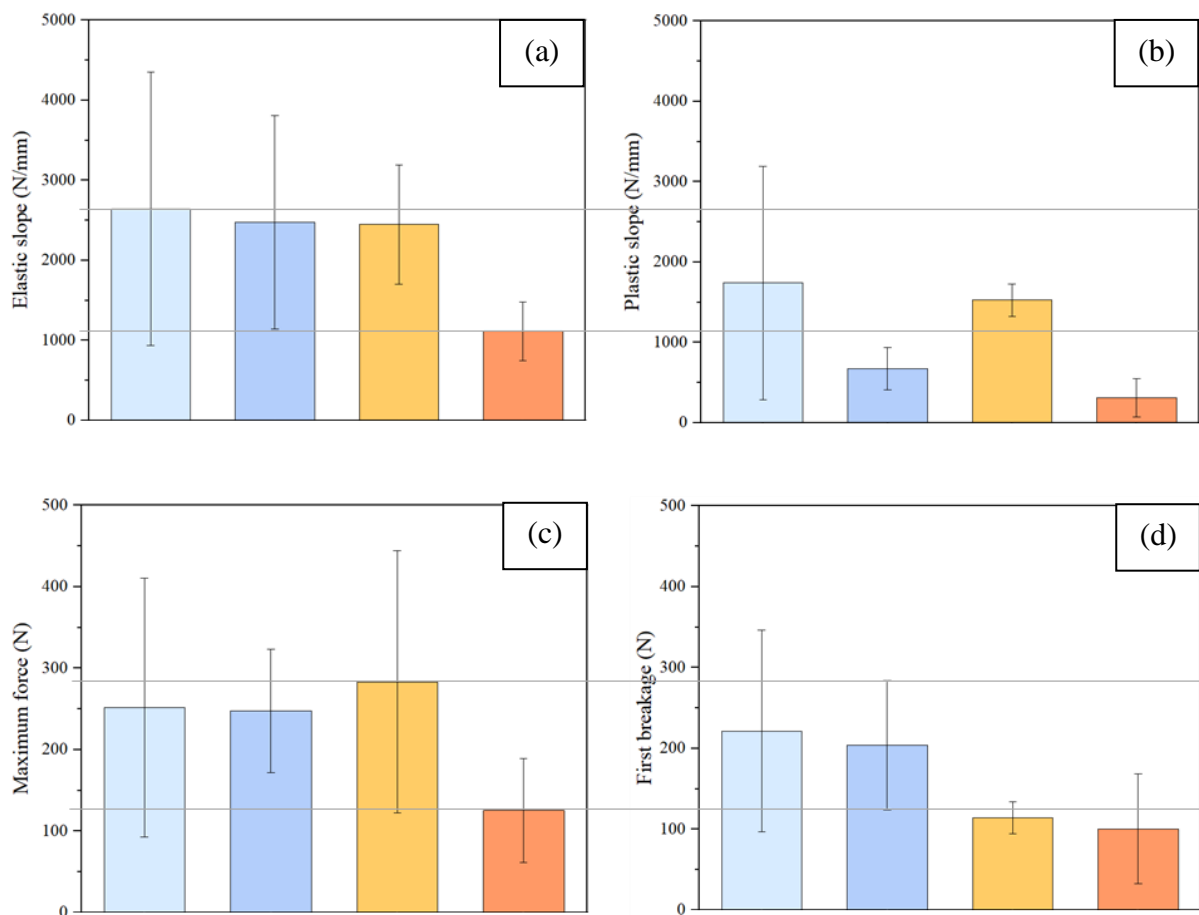


Fig. 83. Small-punch results for (□) equiatomic and (■) equimassic TNZT mechanical alloying by powder metallurgy, and (■) equiatomic and (■) equimassic TNZT mechanical alloying by powder metallurgy and casting: (a) elastic slope, (b) plastic slope, (c) maximum force, and (d) first breakage. Grey lines delimited the maximum and minimum values corresponding to the elastic slope and the maximum force.

4.3.6. Fractography analysis

As it can be seen, these alloys show brittle behaviour, which is confirmed after analysis of the fractures in bending tests (**Fig. 84**).

In the equiatomic sample fracture, both large and small cleavage fracture zones are observed. However, in the equimassic sample fracture, despite the predominance of cleavage fracture, ductility cones are observed, which may be associated with a particular phase.

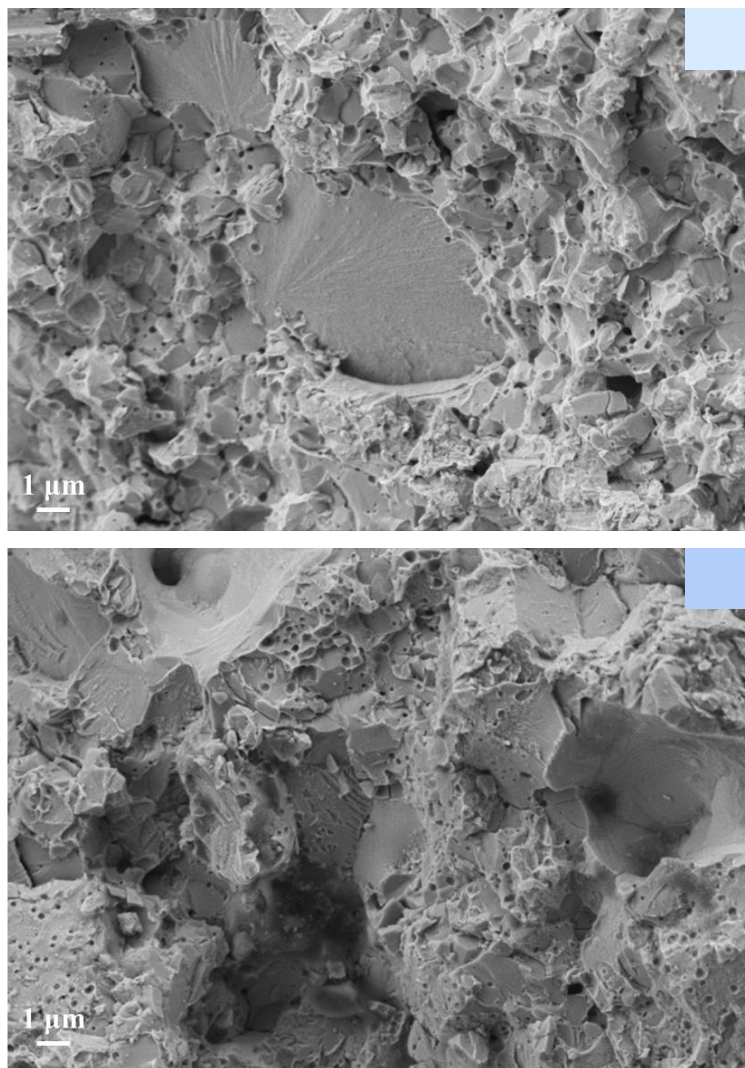


Fig. 84. Fractography after the 4-point bending test for (□) equiatomic and (■) equimassic TNZT mechanical alloying by powder metallurgy.

Once the mechanical characterisation has been completed, all that remains is to characterise the alloys in terms of their chemical behaviour.

4.4. CHEMICAL CHARACTERISATION

4.4.1. Corrosion resistance

The following potentiodynamic curves were obtained from the corrosion tests, which show a behaviour not very different among the alloys. Nevertheless, the OCP value of the equiatomic cast iron alloy stands out, which is approximately 45% lower than the rest.

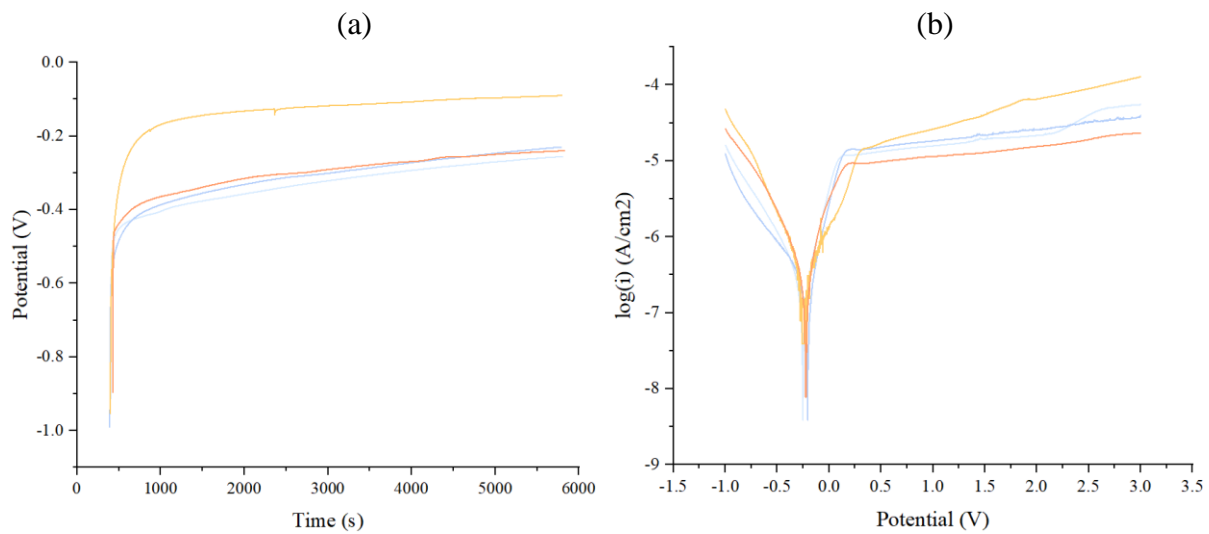


Fig. 85. (a) OCP graphs as a function of time and (b) potentiodynamic polarisation curves for (□) equiatomic and (■) equimassic TNZT mechanical alloying by powder metallurgy, and (□) equiatomic and (■) equimassic TNZT mechanical alloying by powder metallurgy and casting. Grey lines delimited the maximum and minimum values corresponding to the elastic slope and the maximum force.

Table 37 and **Table 38** shows the precisely values associated with **Fig. 85**.

Table 37. Corrosion parameters for equiatomic and equimassic TNZT mechanical alloying by powder metallurgy (EA MA PM, EM MA PM), and equiatomic and equimassic TNZT mechanical alloying by powder metallurgy and casting (EA MA C, EM MA C).

Alloy	OCP (V)	E_{corr} (V)	i_{corr} ($\mu\text{A}/\text{cm}^2$)	C_r ($\mu\text{m}/\text{year}$)
EA MA PM	-0.283 ± 0.038	-0.286 ± 0.025	0.083 ± 0.011	7.808 ± 1.011
EM MA PM	-0.208 ± 0.103	-0.239 ± 0.073	0.052 ± 0.038	4.957 ± 3.598
EA MA C	-0.131 ± 0.037	-0.279 ± 0.039	0.081 ± 0.029	7.650 ± 2.709
EM MA C	-0.226 ± 0.031	-0.226 ± 0.003	0.092 ± 0.028	8.741 ± 2.688

Table 38. Passive layer parameters for equiatomic and equimassic TNZT mechanical alloying by powder metallurgy (EA MA PM, EM MA PM), and equiatomic and equimassic TNZT mechanical alloying by powder metallurgy and casting (EA MA C, EM MA C).

Alloy	ΔE_p (V)	E_b (V)	R_p ($k\Omega/cm^2$)
EA MA PM	2.391 ± 0.081	1.772 ± 0.500	307.924 ± 43.264
EM MA PM	> 2.500	-	282.451 ± 58.686
EA MA C	> 2.500	-	345.977 ± 152.537
EM MA C	> 2.500	-	296.734 ± 110.796

Similarly, the EIS results are shown in two different graphs. On the one hand, the Nyquist plot, where the ratio of the real and imaginary parts of the impedance (Z') is shown (**Fig. 86**). On the other hand, the Bode plot through the impedance modulus (Z') and the phase angle (-phase) versus frequency (**Fig. 87**).

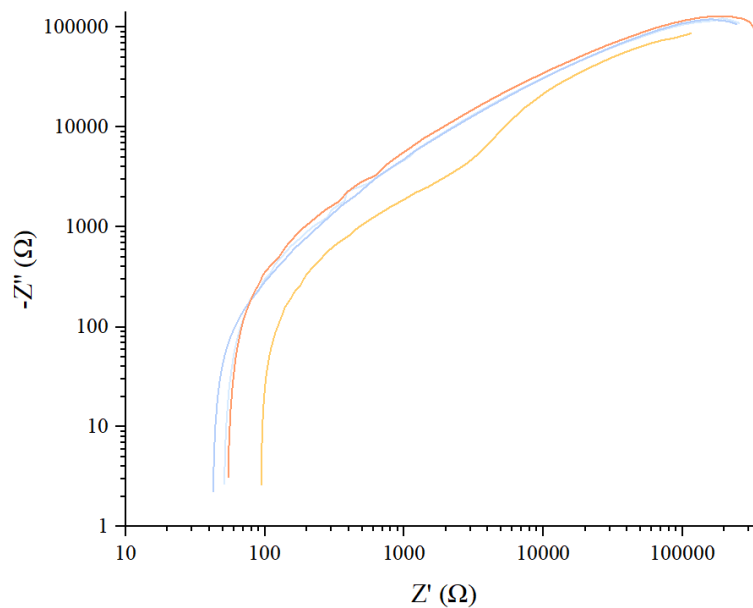


Fig. 86. Nyquist plots for (light blue) equiatomic and (dark blue) equimassic TNZT mechanical alloying by powder metallurgy, and (yellow) equiatomic and (orange) equimassic TNZT mechanical alloying by powder metallurgy and casting.

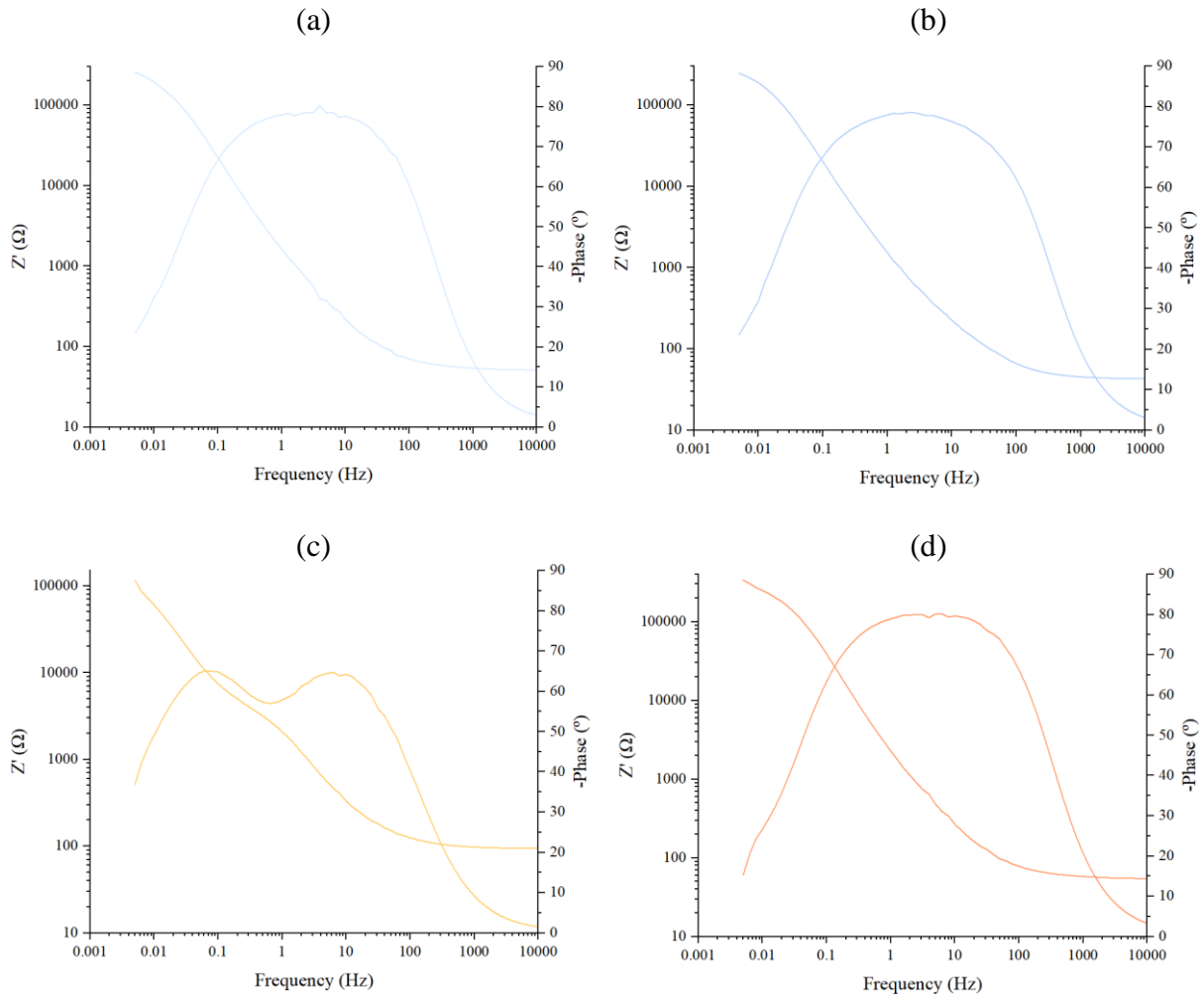


Fig. 87. Bode plots for (a) equiatomic and (b) equimassic TNZT mechanical alloying by powder metallurgy, and (c) equiatomic and (d) equimassic TNZT mechanical alloying by powder metallurgy and casting.

Finally, the single-layer circuit (**Fig. 88**) is the one that best simulates the behaviour of the alloys. It is composed of three elements, a series resistance and parallel resistance (R_s and R), and capacitor (C) which simulates the capacitive behaviour of the corrosion.

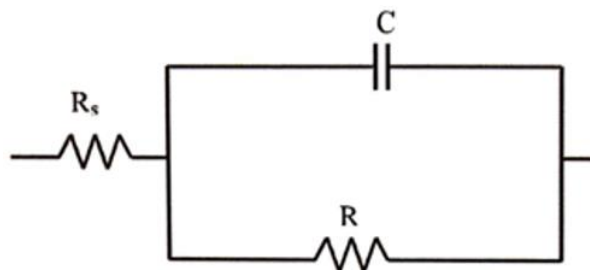


Fig. 88. Single-layer EEC used for fitting the experimental data, where R_s represents the electrolyte resistance and RC the compact layer (Lasia, 2014).

These parameters values are detailed in **Table 39**. In addition, others such as the capacitance exponent (n) and the coefficient of determination (χ^2). The first one indicates whether the EEC is capacitive or inductive, whereas the latter indicates the reliability of the measurement.

Table 39. EEC parameters theoretical approach to the experimental behaviour of the equiatomic and equimassic TNZT mechanical alloying by powder metallurgy (EA MA PM, EM MA PM), and equiatomic and equimassic TNZT mechanical alloying by powder metallurgy and casting (EA MA C, EM MA C).

Alloy	R_s ($\Omega \cdot \text{cm}^2$)	R ($\text{k}\Omega \cdot \text{cm}^2$)	C ($\mu\text{F} \cdot \text{cm}^2$)	n	χ^2
EA MA PM	41.36 ± 1.15	260.25 ± 15.27	30.86 ± 0.52	0.862 ± 0.004	0.003 ± 0.001
EM MA PM	39.40 ± 0.72	242.57 ± 8.84	36.13 ± 0.41	0.873 ± 0.003	0.002 ± 0.002
EA MA C	67.27 ± 4.41	298.88 ± 68.62	68.98 ± 2.06	0.742 ± 0.008	0.009 ± 0.0002
EM MA C	54.23 ± 3.12	266.90 ± 4.44	16.97 ± 0.34	0.830 ± 0.004	0.004 ± 0.003

Regarding the fitting, it seems to be a good approximation due to the n values, that are at least higher than 0.7 and χ^2 values that are lower than 0.01. This means that effectively, samples have a capacitive behaviour, and the simple-layer circuits represents it so well.

4.4.2. Wettability

After carrying out some tests, results are analysed and collected in **Table 40**.

Table 40. Wettability parameters and surface energy for equiatomic and equimassic TNZT mechanical alloying by powder metallurgy (EA MA PM, EM MA PM), and equiatomic and equimassic TNZT mechanical alloying by powder metallurgy and casting (EA MA C, EM MA C).

Alloy	Θ_w ($^\circ$)	Θ_{d-m} ($^\circ$)	γ_L (mN/m)	γ_L^d (mN/m)	γ_L^p (mN/m)
EA MA PM	67.21 ± 1.32	43.15 ± 2.68	48.29 ± 2.21	37.99 ± 1.41	10.30 ± 0.8
EM MA PM	51.04 ± 2.29	45.90 ± 0.87	56.53 ± 1.86	36.53 ± 0.47	20.01 ± 1.39
EA MA C	89.81 ± 2.77	45.62 ± 1.34	38.57 ± 1.39	36.68 ± 0.72	1.90 ± 0.66
EM MA C	54.76 ± 1.90	51.81 ± 0.26	52.45 ± 1.32	33.26 ± 0.15	19.19 ± 1.17

Additionally, to better understand them, they are embodied in **Fig. 89**, together with some important references such as the boundary condition (90°), or the surface free energy of both liquids employed.

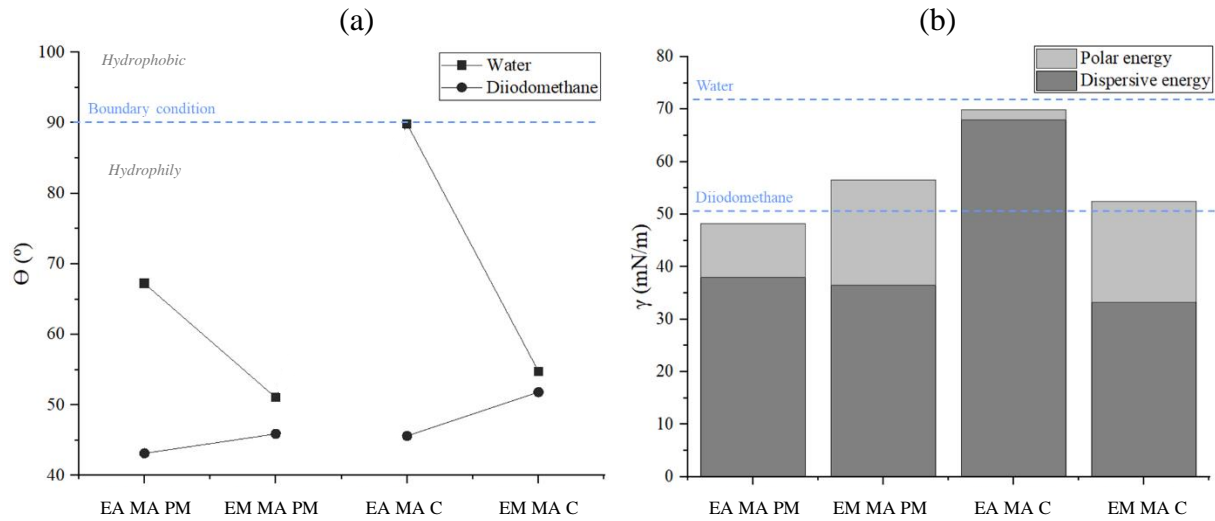


Fig. 89. (a) Contact angle and (b) surface free energy results for equiatomic and equimassic TNZT mechanical alloying by powder metallurgy (EA MA PM, EM MA PM), and equiatomic and equimassic TNZT mechanical alloying by powder metallurgy and casting (EA MA C, EM MA C).

5. EXPERIMENTAL DISCUSSION

The development of HEAs and MEAs with different chemical compositions has led to a wider family of alloys. Most TNZT alloys studies deal with casting manufacturing processes (Hori, Nagase, Todai, Matsugaki, & Nakano, 2019; Rossi, Ventura, Milián, Escuder, & Amigó Borrás, 2022; Hua et al., 2021). In addition, heat treatments (Niinomi, 2003; Nag, Banerjee, & Fraser, 2009; Li et al., 2014; or Wang et al., 2019; Banerjee, Nag, Stechschulte, & Fraser, 2004) are usually applied to promote different strengthening mechanisms. However, there is a tendency to study PM as a method of obtaining alloys, using in particular MA process (Derz, Matula, & Dercz, 2016).

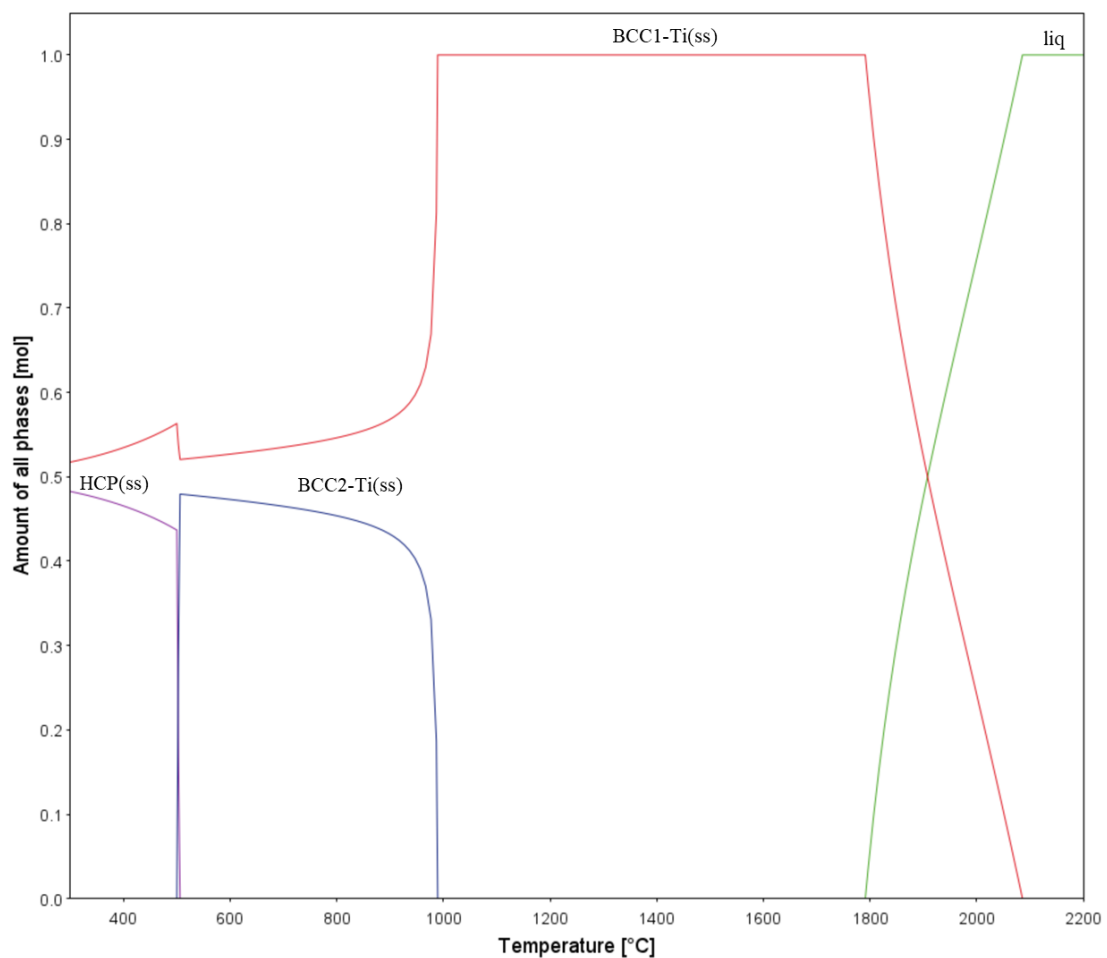


Fig. 90. Thermodynamic simulations of the cooling-phase diagram for equiatomic TNZT MEAs made by Thermo-Calc software AB, version 2022a and TCHEA3: High Entropy Alloy v3.1 database.

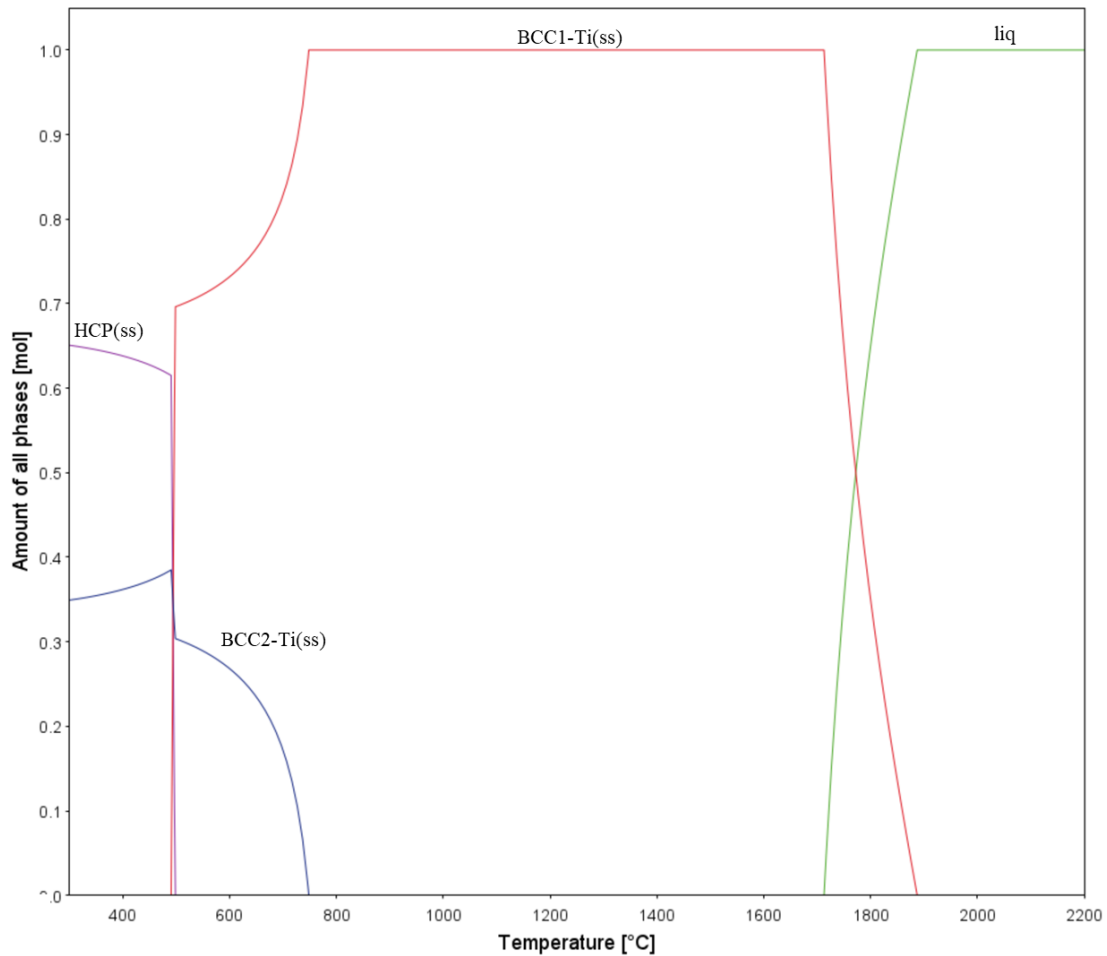


Fig. 91. Thermodynamic simulations of the cooling-phase diagram for equimassic TNZT MEAs by Thermo-Calc software AB, version 2022a and TCHEA3: High Entropy Alloy v3.1 database.

According to the cooling-phase diagrams in **Fig. 90** and **Fig. 91**, the formation of two solid solutions whose structure was associated to the BCC-Ti was expected, since all the elements that compose the alloy are β -stabilisers. However, an FCC phase associated with Zr, and a BCC related with the rest of the elements (Ti-Nb-Ta) were obtained. This fact is so remarkable as this is not the case for other studied TNZT alloys. In the case of the alloys reported by Cuevas, Aguilar, Medinac, Béjarc, & Oseguera (2019), there is a cubic phase formed mostly by Ti, Nb, and Ta while Zr has a different hexagonal structure. Likewise, Brailovski et al. (2011) and Li, Ma, Xiong, Qu, & Li (2022) also obtained a β -Ti phase, in addition to α and α' -martensite Ti phases. However, in the latter, alloys were developed by MA without introducing a PCA to avoid powder contamination.

It is important to outstand that the different phases have been defined from its cell pattern instead of its chemical composition. The aim is to achieve a better understanding of what is happening along the microstructure of the alloys.

Thus, FCC-Zr might be caused as a side effect of the MA process. In this sense, 1% of stearic acid as PCA was added to that mixing in the stainless-steel jars. They may have served as a precursor for the formation of Zr-carbide after deformation caused for the MA. After analysing the phase diagrams shown in **Fig. 92** and **Fig. 93**, and comparing them with **Fig. 67** and **Table 27**, Zr-carbide seems not to be the reason for the FCC-Zr phase formation. There, a high percentage of FCC-Zr is determined, about 5 to 25% in contrast to the added 1%, what may provide a very low carbon percent to the alloy. Although this acid may have promoted the Zr to be transformed in this way, it is not an amount that determines the formation of the possible Zr-carbide.

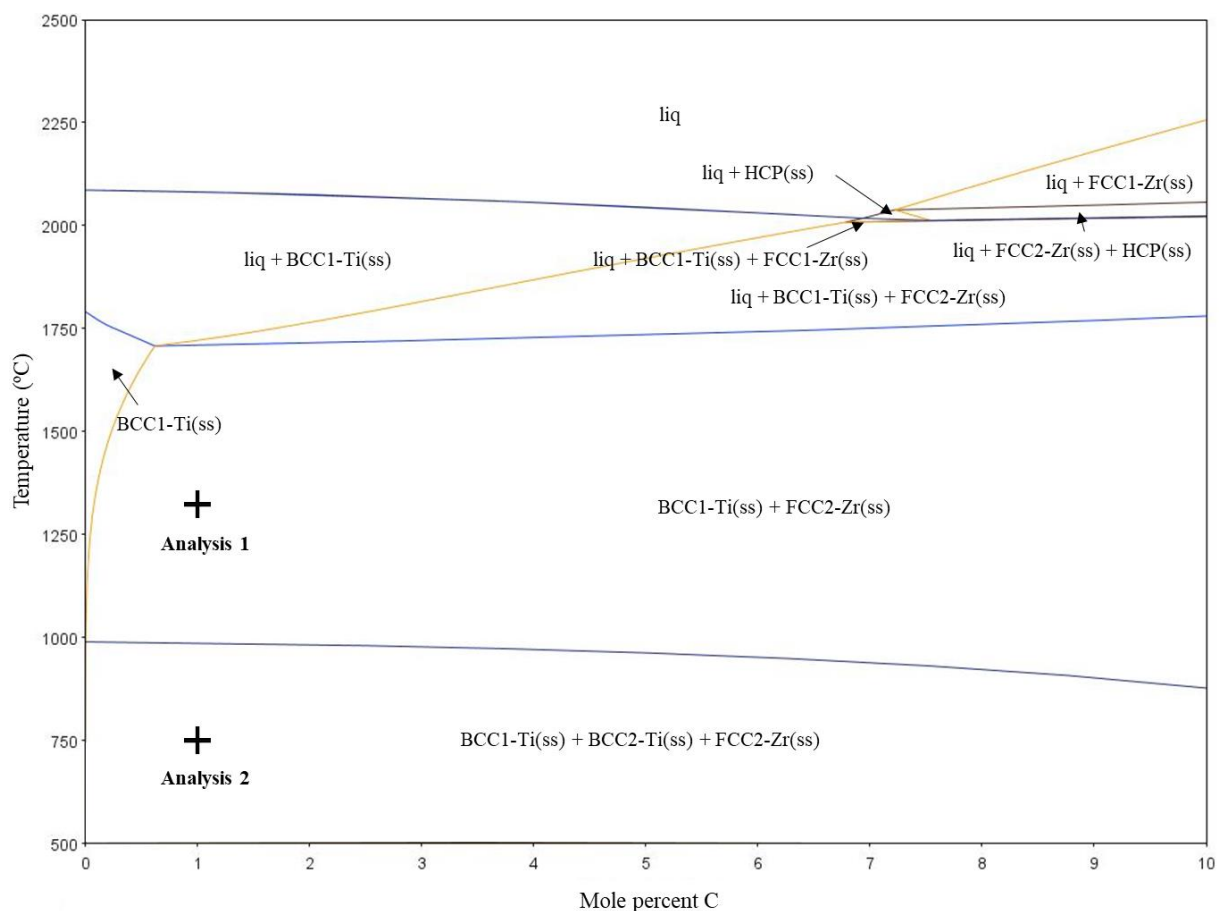


Fig. 92. Thermodynamic simulations of the C influence on the equiatomic TNZT MEAs phase diagram MEA by Thermo-Calc software AB, version 2022a and TCHEA5: High Entropy Alloy v5.0 database.

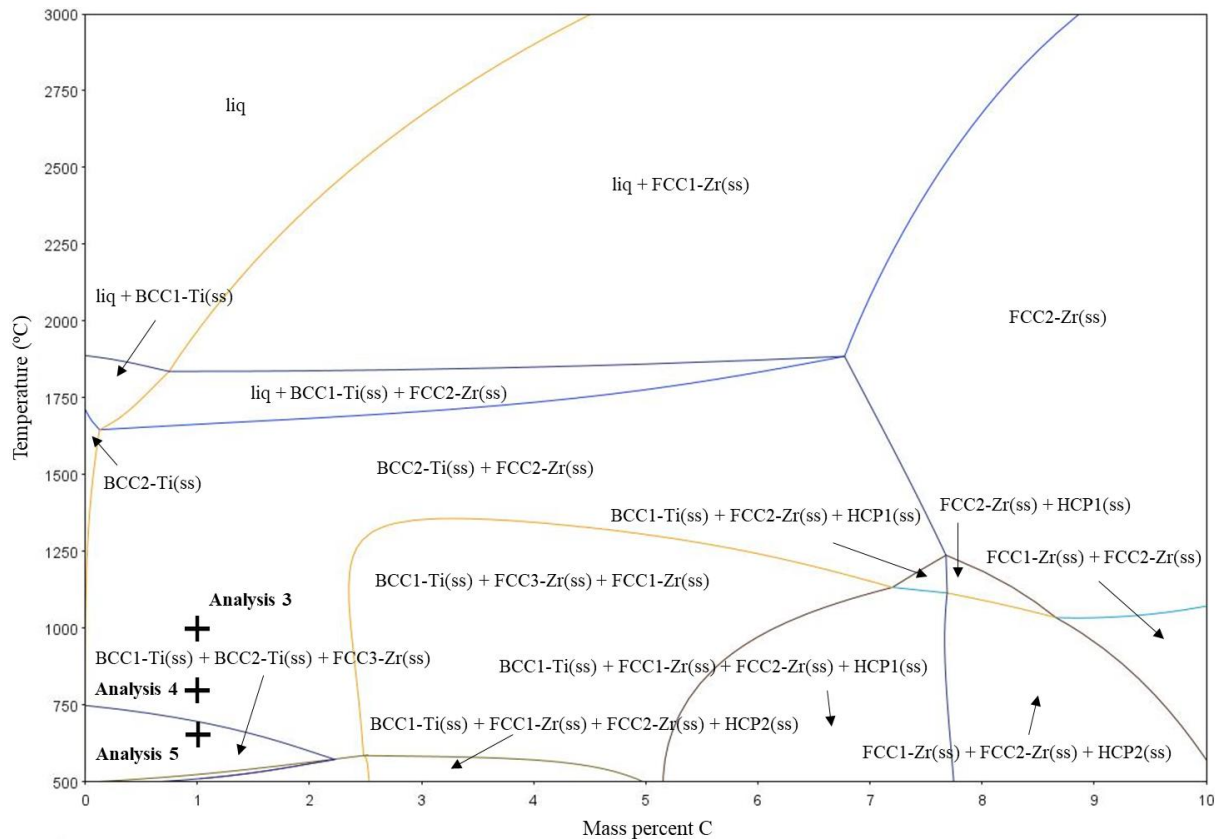


Fig. 93. Thermodynamic simulations of the C influence on the equimassic TNZT MEAs phase diagram by Thermo-Calc software AB, version 2022a and TCHEA5: High Entropy Alloy v5.0 database.

These figures show the existence of ternary systems at low temperatures, while only two different phases could be detected by XRD. It means that the kinetic of the system is extremely slow because samples were cooled from high temperatures without any temperature influence, only that of room. These phases are related to BCC1-Ti(ss) + FCC2-Zr(ss) for the equiatomic alloys and to BCC2-Ti(ss) + FCC2-Zr(ss) for the equimassic ones, whose composition for 1% of C influence is detailed in **Table 41** and **Table 42**. Moreover, some analysis were made in the ternary systems area to verify the composition of each BCC-Ti phase.

The compositional analysis has been done at 1 mol% C for equiatomic TNZT MEAs and at 1 wt.% for the equimassic ones. The reason is because although all the PCA introduced is not C, it is the maximum amount in weight that could be introduced assuming it is. Furthermore, it is more accurate than trying to choose the exact percentage of C associated to each type of alloy since the phase distribution remains the same and the only issue is to determine the feasibility of the assumptions that have been made. Thus, this analysis show the existence of a

Zr-carbide, however, calculations determined around 3 mol%C for the equiatomic alloys as opposed to the approximately 40 at.% determined by the thermodynamic simulation. On the other hand, for equimassic TNZT MEAs, it is determined around a 8 wt%C as opposed to the approximately 0.45 wt% calculated. In addition, both BCC-Ti phases of the ternary compound have very different composition, what means that the microstructure was definitely ‘frozen’ when two phases are formed. So, not having seen the ternary system is not an error associated with the similarity of BCC1-Ti and BCC2-Ti during the XRD analysis.

Table 41. Compositional analysis to the thermodynamic simulated stable phases for equiatomic TNZT MEAs shown in Fig. 92 at 1%C.

Stable Phases	Element	Analysis 1 - 1,300 °C		Analysis 2 - 750 °C	
		Wt. (%)	mol(%)	Wt. (%)	mol(%)
BCC1-Ti(ss)	Ti	-	-	0.06284	0.15916
	Nb	-	-	0.28072	0.36643
	Zr	-	-	0.05229	0.06952
	Ta	-	-	0.60414	0.40489
	C	-	-	1.826E-8	1.844E-7
BCC2-Ti(ss)	Ti	0.11358	0.24620	0.20918	0.35772
	Nb	0.22815	0.25487	0.13130	0.11572
	Zr	0.21408	0.24356	0.51254	0.46005
	Ta	0.44412	0.25474	0.14699	0.06651
	C	0.00007	0.00062	1.019E-6	6.946E-6
FCC2-Zr(ss)	Ti	0.01140	0.01467	0.00088	0.00111
	Nb	0.02027	0.01343	0.00221	0.00143
	Zr	0.83331	0.56247	0.91405	0.60321
	Ta	0.05908	0.02010	0.00449	0.0015
	C	0.07595	0.38933	0.07836	0.39275

Table 42. Compositional analysis to the thermodynamic simulated stable phases for equimassic TNZT MEAs shown in Fig. 93 at 1%C.

Stable Phases	Element	Analysis 3 - 1,000 °C		Analysis 4 - 800 °C		Analysis 5 - 600 °C	
		Wt. (%)	mol(%)	Wt. (%)	mol(%)	Wt. (%)	mol(%)
BCC1-Ti(ss)	Ti	-	-	-	-	0.11575	0.25221
	Nb	-	-	-	-	0.40084	0.45009
	Zr	-	-	-	-	0.03353	0.03834
	Ta	-	-	-	-	0.44988	0.25936
	C	-	-	-	-	3.217E-9	2.794E-8
BCC2-Ti(ss)	Ti	0.27155	0.46979	0.27273	0.47188	0.38200	0.57891
	Nb	0.28220	0.25160	0.28369	0.25296	0.20495	0.16007
	Zr	0.16459	0.14945	0.16001	0.14531	0.24181	0.19234
	Ta	0.28163	0.12892	0.28357	0.12983	0.17124	0.06867
	C	0.0003	0.0023	2.679E-6	0.00002	4.734E-7	2.860E-6
FCC2-Zr(ss)	Ti	0.01051	0.01299	0.00316	0.00390	-	-
	Nb	0.01534	0.00977	0.00575	0.00366	-	-
	Zr	0.87249	0.56595	0.90249	0.58581	-	-
	Ta	0.01947	0.00637	0.00656	0.00215	-	-
	C	0.08219	0.40492	0.08201	0.40447	-	-
FCC3-Zr(ss)	Ti	-	-	-	-	0.00077	0.00095
	Nb	-	-	-	-	0.00171	0.00109
	Zr	-	-	-	-	0.91425	0.59422
	Ta	-	-	-	-	0.00160	0.00052
	C	-	-	-	-	0.08168	0.40322

FCC-Zr was firstly reported in cold-rolled Zr in 2017 (Zhao, Hu, Song, & Ni, 2017), as a consequence of plastic deformations, and secondly in an as-cast Zr alloy in 2020 (Liu et al., 2020). What is more, Islam and Haque (2018) investigated the induction of phase transformation in Zr thin film as consequence of tensile strain using classical molecular dynamics simulation. α -Zr (HCP) transformed to the FCC phase during the tensile loading along specific directions. In fact, when temperature increased, the energy needed to induce transformation was reduced and it was independent of the film thickness. Thereby, the pressing or mechanical alloying steps could promote the strain-induced phase transformation in Zr. In the same line, Tang et al. (2021) studied about the phase formation and phase transformation along with powder consolidation of the Al-Ti-Mn ternary system. This established the effectiveness of the straining to promote the transformation from the α phase to the ω phase.

Comparing the XRD and the TEM diffraction patterns obtained in this work with those of Wang et al. (2017) and Zhao, Hu, Song, and Ni (2017), great similarity was found to both. Therefore, there was nothing to confirm the existence of the FCC phase due to the formation of the Zr-carbide or the plastic deformation that the Zr may have undergone during the TNZT fabrication. The only certainty is the relationship between FCC-Zr with the mechanical alloying process, since Nguyen et al. (2020) worked on an equiatomic direct casting TZNT alloy with a Ti-Nb-Ta-rich BCC_1 and a Zr-rich BCC_2 .

Finally, from the microstructural part, **Fig. 62-65** showed a homogeneous distribution of immiscible Zr through the microstructure. Carmen, Kamel, and Carmen-Iulia (2014) worked with casting samples whose chemical compositions were Ti-21Nb-6Zr-15Ta and Ti-25Nb-10Zr-8Ta and had a higher diffusion of the elements compared to the alloys studied throughout this work. It can therefore be concluded that the atomic diffusion depends mainly on the sintering temperature and the chemical composition and, according to the latter, the solubility of Zr is between 10 and 25%at. for this type of alloys. There are other authors such as Li, Ma, Xiong, Qu, and Li (2022) who have worked with an amount of Zr between these percentages, but have not described the observed element diffusion.

When looking the mechanical properties of the studied alloys, it can be seen that the casting samples have a much higher hardness than those obtained by powder metallurgy. Theoretically, the alloys with BCC structure have a higher hardness than those with FCC structure, and grain size and porosity also play a role, so that the smaller the grain size and porosity, the higher the hardness. In this sense, taking into account **Table 27** according to the XRD results, the casting samples have a higher percentage of BCC phase. In addition, **Fig. 58** shows a comparison of the porosity in each TNZT alloy, where the casting alloys have the least porosity and, in turn, the equimassic have fewer pores than the equiatomic. Nevertheless, as can be seen in **Fig. 67**, powder metallurgy alloys have smaller grain size. Ta amount blocks grain growth, namely the higher the atomic amount, the smaller the grain size.

Therefore, conventional powder metallurgical samples, although they have a smaller grain size, also have a lower percentage of the BCC phase, as well as a higher porosity, which means they have a lower hardness. In turn, if they are compared with the hardness values of other typical alloys in the biomedical field, such as Ti-6Al-4V, 316 stainless steel (SS) or stellite 6, which is a Cr-Co alloy, it is observed that they have similar values. Only 316 SS and MA PM are lower than 400 HV. These values are shown in **Table 43**.

Table 43. Hardness properties comparison between TNZT MEAs and Ti-6Al-4V, 316 SS, and Stellite 6 (Yeh et al., 2004).

Alloy	Preparation method	Hardness (HV)
MA PM	Powder metallurgy	213 - 241
MA C	Powder metallurgy + casting	412 - 416
316 SS	Casting	189
Stellite 6	Casting	413
Ti-6Al-4V	Casting	412

According to Carmen, Kamel, and Carmen-Iulia (2014), new TNZT alloys have low elastic modulus of about 20-25% of others alloys. Moreover, Laheurtea et al. (2010) established that a decrease in Ta content should result in a decrease in the intrinsic modulus. In that case, where β -Ti and α'' -Ti was obtained, this reduction of the elastic modulus is not only related to

the Ta content, but to the overall chemical composition, as β -Ti has a lower elastic modulus than α' -Ti. Therefore, it may be an overall effect of the use of beta-stabilisers. Even though equimassic TNZT alloys, who have a fewer Ta content, have a lower elastic modulus, as can be seen in **Table 44**, the decrease in the elastic modulus is not as large as expected based on the trend of the samples of Laheurtea et al. (2010). This confirms the influence of the overall chemical composition of the alloy. Nevertheless, looking this property alone, TNZT MEAs has no advantage over the related alloys developed.

Table 44. *Intrinsic elastic modulus comparison between TNZT MEAs and Ti-6Al-4V, 316L SS, Co-Cr-Mo (Semlitsch & Willert, 1980), CP-Ti (grade 4) (Li, 2000), Ti-35Nb-5Ta-7Zr (Narayan, 2012), and bone (Castro, Jaeger, Baptista, & Oliveira, 2021).*

Alloy	Preparation method	Intrinsic elastic modulus (GPa)
(EM/EA) MA PM	Powder metallurgy	111 - 133
(EM/EA) MA C	Powder metallurgy + casting	115 - 127
316L SS	Hot forge + annealed	200
Co-Cr-Mo	Casting + wrought	200 - 230
CP-Ti (grade 4)	Annealed	105
Ti-35Nb-5Ta-7Zr	Annealed	55
Ti-6Al-4V	Hot forge + annealed	110
Bone (*)	-	5 - 30

(*) Depending on whether it is cortical or cancellous.

However, in different tests, equimassic TNZT samples have a higher elasticity and the highest resistance. **Fig. 79**. Despite it, the samples elongation is very low, less than 1% and it is not possible to make a comparison between the different chemical compositions. Only in the case for the 4-point bending test were both types of alloys compared, showing that it is the equiatomic samples that show a higher elongation. These values are shown in **Fig. 82**.

Additionally, small punch test results do not provide clarity on the trend of the mechanical behaviour of the alloys as a function of the manufacturing process or chemical composition. It is explained because it is a specific test designed to forge. Even so, it allows to test many

samples with low quantity of material requirements, a situation which was faced along this work. What is clear is that the plastic slope is much lower than the elastic one and the first breakage is produced before reaching the maximum force supported by the alloys.

Regarding corrosion behaviour, the corrosion rate is higher for the TNZT alloys studied compared to CP-Ti and Ti-6Al-4V. Although the i_{corr} is higher for Ti-6Al-4V, TNZT alloys do not stand out in terms of corrosion behaviour. These values can be seen in **Table 45**.

Table 45. Kinetic corrosion parameters for CP-Ti and Ti-6Al-4V (Rossi, Ventura, Milián, Escuder, & Amigó Borrás, 2022)

Alloy	E_{corr} (V)	i_{corr} ($\mu\text{A}/\text{cm}^2$)	R_p ($\text{k}\Omega/\text{cm}^2$)	C_r ($\mu\text{m}/\text{year}$)
EA MA PM	-0.29 ± 0.03	0.083 ± 0.011	308 ± 43	7.81
EM MA PM	-0.24 ± 0.07	0.052 ± 0.038	282 ± 59	4.98
EA MA C	-0.28 ± 0.04	0.081 ± 0.029	346 ± 153	7.65
EM MA C	-0.23 ± 0.003	0.092 ± 0.028	297 ± 111	8.74
CP-Ti	-0.25 ± 0.13	0.054 ± 0.021	509 ± 199	0.46
Ti-6Al-4V	-0.18 ± 0.02	0.147 ± 0.103	231 ± 129	1.25

According to the study by Socorro-Perdomo, Florido-Suárez, Mirza-Rosca and Saceleanu (2022), increasing the amount of Ta leads to a reduction in polarisation resistance (R_p). However, the opposite is observed in the results obtained for TNZT MEAs, as the equiatomic alloys, which have a higher weight percentage of tantalum, have a higher R_p .

Finally, in relation to the wettability of the alloys, it is important that they are hydrophilic so interaction with the biological medium is allowed, as well as protein adhesion. In other words, for proper adhesion and subsequent proliferation, it is important that samples have a predominantly polar behaviour.

From the results obtained, **Fig. 89** shows that all the samples have a hydrophilic character with a contact angle of less than 90° . Furthermore, there is a tendency for the contact angle to decrease when water, which is the polar liquid, is used as the medium for the equimassic

samples. However, the non-polar contact angle increases. What is clear is that, despite the overall energy calculation, there is no coherent behaviour, but when the energies are analysed separately, there is. That is, analysing the polar energy on the one hand and the dispersed energy on the other hand.

Contact angle also depends on other factors such as porosity. In this aspect, a contradictory behaviour is observed between water and diiodomethane. In particular, sample EA MA C shows disproportionate contact angle values and, consequently, disproportionate surface energy values compared to the rest of the samples. Indeed, it also behaved differently from the rest of the samples in corrosion tests, which demonstrates the great influence not only of the chemistry but also of the phases that make up the alloys in determining their behaviour.

Despite their promising properties, the TNZT alloys studied do not show significant advantages over the alloys used in the biomedical field to date. However, it would be interesting to continue along the same lines, analysing another type of compositions that would allow the development of alloys with good chemical and mechanical properties that have a lower density and elastic modulus to fight against stress shielding.

6. CONCLUSIONS

Among the conclusions obtained, it is worth outstanding the great variability of the results obtained and the lack of machinability found throughout the processing of the TNZT samples in all the ways of obtention. That is referred to the processing route by powder metallurgy and by casting, both in the case of the equiatomic and equimassic compositions from MA powders. Nevertheless, that lack of machinability is higher in the case of the equimassic ones.

Based on electron microscopic studies on equiatomic and equimassic samples, despite mixing the different powders by mechanical alloying, there is not complete homogeneity, which explains the diffusion problems in all the alloys studied.

Moreover, during the sintering process, carried out in the high vacuum furnace according to the cycle shown, the large volumetric contractions produced in the samples stand out. These contractions allow for a significant decrease in the relative porosity of the alloys, displayed in very small concentrations of micropores. In fact, despite what might be expected at first, the porosity does not disappear in the case of the samples obtained by electric arc casting. It may be due to the encapsulation of air bubbles produced during the melting of the material because of the large difference between the melting points of the four elements that make up the alloys. However, a remarkable reduction of the porosity was noticed in both chemical compositions.

In addition, it was confirmed by optical microscopy that the porosity of the equimassic alloys contains fewer micropores than the equimassic ones. At the same time, those obtained by casting, as expected, have less porosity. This observation technique made possible to appreciate the formation of two distinct crystalline phases that are homogeneously distributed among the same main matrix.

Subsequently, by means of electron microscopy, having determined the compositional analysis of both phases, the predominance of tantalum in one of them and the zirconium in the

other was obtained. Thus, there is scarce atomic diffusion in the four different working conditions.

The crystalline structure obtained by XRD agreed with the results of the phase distribution by obtaining two different crystalline structures for all the cases. One of them, associated with the phase with the highest Ti-Nb-Ta content, BCC, and the other, associated with the phase with the highest Zr content, FCC. In addition, these results were consistent with the EBSD analysis and, above all, with the diffraction patterns obtained by TEM.

On the other hand, the grain size turns out to be larger for the case of the cast samples, where, in addition, each grain has a kind of inner grains that have the same preferential orientation associated with the grain in which they are found. As a result of that, a parent-child relationship is established and mostly explained by the crystallographic relationship defined by Pitsch.

Regarding the mechanical characterisation, the elastic modulus analysed by ultrasound is higher than that of other reported TNZT alloys from the literature. This is due to the high concentration of tantalum, which has the highest Young's modulus compared to other elements. In addition, the brittleness and hardness of all the samples was outstanding, as well as the existence of a clear tendency towards greater strength and elasticity and lower elongation of the equimassic alloy comparing with the equiatomic one, both obtained by conventional powder metallurgy.

Finally, the technological behaviour in service in all the alloys showed a good behaviour against corrosion, which was similar for all of them. Within the capacity for interaction with fluids, the higher hydrophilicity of the equimassic samples stands out.

7. FUTURE WORKS

According to the conclusions of this project, the works considered necessary to achieve a more precise evaluation of the mechanical properties of the alloys presented are formulated in the following paragraphs.

Firstly, it is necessary to carry out nanoindentation tests to establish the behaviour of each phase, which cannot be achieved with microhardness alone due to the small size of the grains.

Secondly, it would be interesting to obtain a larger number of samples with the aim to obtain more precise and significant statistical results on the behaviour of the alloys presented. Likewise, it is important to carry out a specific analysis of their oxygen content, given that the compositional analysis made through electron microscopy are not suitable for this purpose.

Along the same lines, other processing parameters used to prepare the MA of the elements should be evaluated to obtain a completely alloyed starting powder. In that sense, a perfect powder alloy is necessary to achieve a homogeneous microstructure that provides better results in terms of their behaviour. At the same time, determining whether or not stearic acid is the precursor of the FFC-Zr phase is a very important factor to be found. Concerning casting process, it is advisable to carry out a preceding solution treatment to improve the elements diffusion.

Finally, it would be convenient to carry out different biological analyses to evaluate the acceptance of the material by different tissues, on account of obtaining a complete evaluation of the feasibility of the different alloys for biomedical use.

8. REFERENCES

- Bandarenka, V., & Ragoisha, G. (2013). *EIS Spectrum Analyser download page*. Retrieved from <http://www.abc.chemistry.bsu.by/vi/analyser/program/program.htm>
- Banerjee, R., Nag, S., Stechschulte, J., & Fraser, H. L. (2004). Strengthening mechanisms in Ti–Nb–Zr–Ta and Ti–Mo–Zr–Fe orthopaedic alloys. *Biomaterials*, *25*, 3413-3419. doi:10.1016/j.biomaterials.2003.10.041
- Beier, F., Gyöngyösi, M., Raeder, T., Von Eckardstein, E., Sperker, W., Albrecht, P., . . . Mudra, H. (2006). First in–human randomized comparison of an anodized niobium stent versus a standard stainless steel stent. *Clin Res Cardiol*, *95*, 455-460. doi:doi.org/10.1007/s00392-006-0406-7
- Biesiekierski, A., Wang, J., Gepreel, M. A.-H., & C. W. (2012). A new look at biomedical Ti-based shape memory alloys. *Acta Biomaterialia*, *8*, 1661-1669. doi:10.1016/j.actbio.2012.01.018
- Brailovski, V., Prokoshkin, S., Gauthier, M., Inaekyan, K., Dubinskiy, S., Petrzhik, M., & Filonov, M. (2011). Bulk and porous metastable beta Ti–Nb–Zr(Ta) alloys for biomedical applications. *Materials Science and Engineering: C*, *31*(3), 643-657. doi:10.1016/j.msec.2010.12.008
- Carmen, B. A., Kamel, E., & Carmen-Iulia, C. (2014). In vitro evaluation of the cytotoxicity of some new titanium alloys. *Key Engineering Materials*, *587*, 303-308. doi:10.4028/www.scientific.net/KEM.587.303
- Castro, D., Jaeger, P., Baptista, A., & Oliveira, J. (2021). An Overview of High-Entropy Alloys as Biomaterials. *Metals*, *11*(4). doi:10.3390/met11040648
- Cuevas, A., Aguilar, C., Medinac, A., Béjarc, L., & Oseguera, J. (2019). Synthesis, characterization and mechanical properties of Ti-Nb-Ta-Zr foams for biomedical applications. *Materials Today: Proceedings*, *13*, 353-361. doi:10.1016/j.matpr.2019.03.165
- Derz, G., Matula, I., & Dercz, J. (2016). Phase composition and microstructure of new Ti-Ta-Nb-Zr biomedical alloys prepared by mechanical alloying method. *Washington University School of Medicine*. doi:10.1017/S0885715617000045

- Elias, L., Schneider, S., Schneider, S., Silva, H., & Malvisi, F. (2008). Microstructural and mechanical characterization of biomedical Ti–Nb–Zr(–Ta) alloys. *Materials Science and Engineering A*, 432, 108-112. doi: 10.1016/j.msea.2006.06.013
- Hori, T., Nagase, T., Todai, M., Matsugaki, A., & Nakano, T. (2019). Development of non-equiatomic Ti-Nb-Ta-Zr-Mo high-entropy alloys for metallic biomaterials. *Scripta Materialia*, 172, 83-87. doi:10.1016/j.scriptamat.2019.07.011
- Hua, N., Wang, W., Wang, Q., Ye, Y., Lin, S., Zhang, L., . . . Liaw, P. K. (2021). Mechanical, corrosion, and wear properties of biomedical Ti–Zr–Nb–Ta–Mo high entropy alloys. *Journal of Alloys and Compounds*, 861. doi:10.1016/j.jallcom.2020.157997
- Islam, Z., & Haque, A. (2018). Strain induced phase transformation in zirconium thin films. *Computational Materials Science*, 143, 425-430. doi:10.1016/j.commatsci.2017.11.032
- Jakubowicz, J. (2020). Special Issue: Ti-Based Biomaterials: Synthesis, Properties and Applications. *Materials*, 13(7). doi:10.3390/ma13071696
- Kiyoshi, A., Niitsu, K., Bertoni, E., Caldeira, L., César, F., Gandra, G., & Sócrates, E. (2020). Appraising the potential of Zr-based biomedical alloys to reduce magnetic resonance imaging artifacts. *Scientific reports*, 10. doi:10.1038/s41598-020-59247-1
- Laheurtea, P., Primab, F., Eberhardtc, A., Gloriantd, T., Warye, M., Patoorc, & E. (2010). Mechanical properties of low modulus β titanium alloys designed from the electronic approach. *Journal of the Mechanical Behavior of Medical Materials*, 3(8), 565-573. doi:10.1016/j.jmbbm.2010.07.001
- Lario, J., Amigó, A., Vicente, Á., & Segovia, F. (2016). Desarrollo de las aleaciones de titanio y tratamientos superficiales para incrementar la vida útil de los implantes. *Revista de Metalurgia*, 52(4), 1-13. doi:10.3989/revmetalm.084
- Lario, J., Escuder, A. V., Segovia, F., & Amigó, V. (2022). Electrochemical corrosion behavior of Ti-35Nb-7Zr-5Ta powder metallurgic alloys after Hot Isostatic Process in fluorinated artificial saliva. *Journal of Materials Research and Technology*, 16, 1435-1444. doi:10.1016/j.jmrt.2021.12.085
- Lario, J., Poler, R., & Amigó, V. (2022). Powder metallurgy: a new path for advanced titanium alloys in the EU medical device supply chain. *Applied Materials Today*.
- Lasia, A. (2014). *Electrochemical Impedance Spectroscopy and its Applications*. New York: Springer Science + Business Media. doi:10.1007/978-1-4614-8933-7

- Li, J. (2000). Microstructure and properties of materials. *World Scientific*, 2, 49-55. doi:10.1038/71527
- Li, Q., Ma, X., Xiong, C., Qu, W., & Li, Y. (2022). Effects of annealing temperature on microstructures and shape memory effect of Ti-19Zr-11Nb-2Ta alloy sheets. *Journal of Alloys and Compounds*, 897. doi:10.1016/j.jallcom.2021.162728
- Li, Y., Yang, C., Haidong, Z., Qu, S., Li, X., & Li, Y. (2014). New Developments of Ti-Based Alloys for Biomedical Applications. *Materials*, 7, 1709-1800. doi:10.3390/ma7031709
- Liu, C., Li, G., Gu, H., Yuan, F. H., Ali, M., Zhang, Y., & Guo, W. (2020). Observation of FCC-Zr phase in as-cast Zircaloy-4 alloy. *Materials Letters*, 267. doi:10.1016/j.matlet.2020.127551
- Long, Y., Niinomi, M., Akahori, T., Fukui, H., & Toda, H. (2005). Corrosion resistance and biocompatibility of Ti-Ta alloys for biomedical applications. *Materials Science and Engineering A*, 398, 28-36. doi:10.1016/j.msea.2005.03.032
- Martín, R., & Bautista, A. (2014). Simulación mediante Circuitos Equivalentes de la Impedancia Electroquímica de armaduras de acero inoxidable en mortero. *Universidad Carlos III de Madrid*.
- Medvedev, A., Molotnikov, A., Lapovok, R., Rolf Zeller, B. S., Habersetzer, P., & Dalla, T. (2016). Microstructure and mechanical properties of Ti-15Zr alloy used as dental implant material. *Science Direct*. doi:10.1016/j.jmbbm.2016.05.008
- Miracle, D., & Senkov, O. (2017). A critical review of high entropy alloys and related concepts. *Acta Materialia*, 122, 448-511. doi: 10.1016/j.actamat.2016.08.081
- Nag, S., Banerjee, R., & Fraser, H. L. (2009). Intra-granular alpha precipitation in Ti-Nb-Zr-Ta biomedical alloys. *J Mater Sci*, 44, 808-815. doi:10.1007/s10853-008-3148-2
- Nagoshi, T., Yasuda, T., Otaki, N., Tahara, M., Hosoda, H., & Sone, M. (2020). Evaluation of the Shape Memory Effect by Micro-Compression Testing of Single Crystalline Ti-27Nb Ni-Free Alloy. *Materials*, 13, 110. doi:10.3390/ma13010110
- Narayan, R. (2012). Materials for medical devices, fundamentals of medical implant materials. *ASM Handbook*, 23, 6-16.
- Nguyen, V., Qian, M., Shi, Z., Song, T., Huang, L., & Zou, J. (2018). A novel quaternary equiatomic Ti-Zr-Nb-Ta medium entropy alloy (MEA). *Intermetallics*, 101, 39-43. doi: 10.1016/j.intermet.2018.07.008

- Nguyen, V., Qian, M., Shi, Z., Tran, X., Fabijanic, D., Joseph, J., . . . Zou, J. (2020). Cuboid-like nanostructure strengthened equiatomic Ti–Zr–Nb–Ta medium entropy alloy. *Materials Science and Engineering: A*, 798. doi:10.1016/j.msea.2020.140169
- Niinomi, M. (2003). Fatigue performance and cyto-toxicity of low rigidity titanium alloy, Ti–29Nb–13Ta–4.6Zr. *Biomaterials*, 24(16), 2673-2683. doi:10.1016/S0142-9612(03)00069-3
- O'Brien, B. (2015). Niobium Biomaterials. In M. Niinomi, T. Narushima, & M. Nakai, *Advances in Metallic Biomaterials: Tissues, Materials and Biological Reactions* (Vol. 3, pp. 245-272). Berlin: Springer Series. doi:10.1007/978-3-662-46836-4_11
- Okazaki, Y. (2001). A New Ti–15Zr–4Nb–4Ta alloy for medical applications. *Current Opinion in Solid State and Materials Science*, 5(1), 45-53. doi: 10.1016/S1359-0286(00)00025-5
- Raducanu, D., Vasilescu, E., Cojocaru, V., Cinca, I., Drob, P., Vasilescu, C., & Drob, S. (2011). Mechanical and corrosion resistance of a new nanostructured Ti–Zr–Ta–Nb alloy. *Journal of the Mechanical Behavior of Biomedical Materials*, 4(7), 1421-1430. doi:10.1016/j.jmbbm.2011.05.012
- Rossi, M., Ventura, B., Milián, L., Escuder, A., & Amigó Borrás, V. (2022). Study of Electrochemical and Biological Characteristics of As-Cast Ti-Nb-Zr-Ta System Based on Its Microstructure. *Metals*, 12. doi:10.3390/met12030476
- Semlitsch, M., & Willert, H. (1980). Properties of implant alloys for artificial hip joints. *Medical and Biological Engineering and Computing*, 18, 511–520. doi:10.1007/BF02443329
- Sharma, P., Dwivedi, V., & Dwivedi, S. P. (2021). Development of high entropy alloys: A review. *Materials Today: Proceedings*, 43, Part 1, 502-509. doi:10.1016/j.matpr.2020.12.023
- Slokar, L., Matković, T., & Matković, P. (2012). COMPARISON OF MICROSTRUCTURAL CHARACTERISTICS FOR BIOMEDICAL Ti(70,80 at.%)–Cr–Mo AND Ti(70,80 at.%)–Nb–Zr ALLOYS. *Materials Science*, 6, 178-182.
- Socorro-Perdomo, P., Florido-Suárez, N., Mirza-Rosca, J., & Saceleanu, M. (2022). EIS Characterization of Ti Alloys in Relation to Alloying Additions of Ta. *Materials*, 15(2). doi:10.3390/ma15020476

- Tang, Y., Murayama, M., Edalati, K., Wang, Q., Iikubo, S., Masuda, T., . . . Horita, Z. (2021). Phase transformations in Al-Ti-Mg powders consolidated by high-pressure torsion: Experiments and first-principles calculations. *Journal of Alloys and Compounds*, 889. doi:10.1016/j.jallcom.2021.161815
- Torralba, J. M., P., A., & García-Junceda, A. (2019). High-entropy alloys fabricated via powder metallurgy. A critical review. *Powder Metallurgy*, 62:2, 84-114. doi:10.1080/00325899.2019.1584454
- Tsai, M.-H., & Yeh, J.-W. (2014). High-Entropy Alloys: A Critical Review. *Materials Research Letters*, 2(3), 107-123. doi: 10.1080/21663831.2014.912690
- University of Trento. (2022). *MAUD: Materials Analysis Using Diffraction version 2.993*. Retrieved from <http://maud.radiographema.eu/>
- Wang, G., Liu, Q., Yang, J., Li, X., Sui, X., Gu, Y., & Liu, Y. (2019). Synthesis and thermal stability of a nanocrystalline MoNbTaTiV refractory high-entropy alloy via mechanical alloying. *International Journal of Refractory Metals and Hard Materials*, 84. doi:10.1016/j.ijrmhm.2019.104988
- Wang, J., Ni, D., Dong, S., Yang, G., Gao, Y., Kan, Y., . . . Zhang, X. (2017). Synthesis of nanocrystallized zirconium carbide based on an aqueous solution-derived precursor. *The Royal Society of Chemistry*, 7, 22722–22727. doi:10.1039/c7ra02586f
- Yang, W., Liu, Y., Pang, S., Liaw, P., & Zhang, T. (2020). Bio-corrosion behavior and in vitro biocompatibility of equimolar TiZrHfNbTa high-entropy alloy. *Intermetallics*, 124. doi:10.1016/j.intermet.2020.106845
- Yeh, J., Chen, S., Lin, S., Gan, J., Chin, T., Shun, T., . . . Chang, S. (2004). Nanostructured high-entropy alloys with multiple principal elements: Novel alloy design concepts and outcomes. *Advanced Engineering Materials*, 6(5), 299-303. doi:10.1002/adem.200300567
- Yılmaz, E., Gökçe, A., Findik, F., Gulsoy, H. O., & İyibilgin, O. (2018). Mechanical properties and electrochemical behavior of porous Ti-Nb biomaterials. *Journal of the Mechanical Behavior of Biomedical Materials*, 87, 59-67. doi:10.1016/j.jmbbm.2018.07.018
- Zhao, H., Hu, X., Song, M., & Ni, S. (2017). Mechanisms for deformation induced hexagonal close-packed structure to face-centered cubic structure transformation in zirconium. *Scripta Materialia*, 132, 63-67. doi:10.1016/j.scriptamat.2017.01.034

RESULT'S DISSEMINATION

The results obtained in this Master's thesis have so far been disseminated as follows.

- *Conferences*

XVI Congreso Nacional de Materiales. Ciudad Real, Spain

González, C., González, G., AL-Hawajreh ,G., Romero, L., Amigó, V. (2022). Análisis del comportamiento mecánico de aleaciones cuaternarias de alta entropía. *XVI Congreso Nacional de Materiales, Libro de Abstracts*. Edited by Sociedad Española de Materiales, ISBN 978-84-09-38118-0.

At this conference some of the results of this research project were presented, in particular those related to the routine followed to produce the samples and the mechanical characterisation together with some microstructural notions.

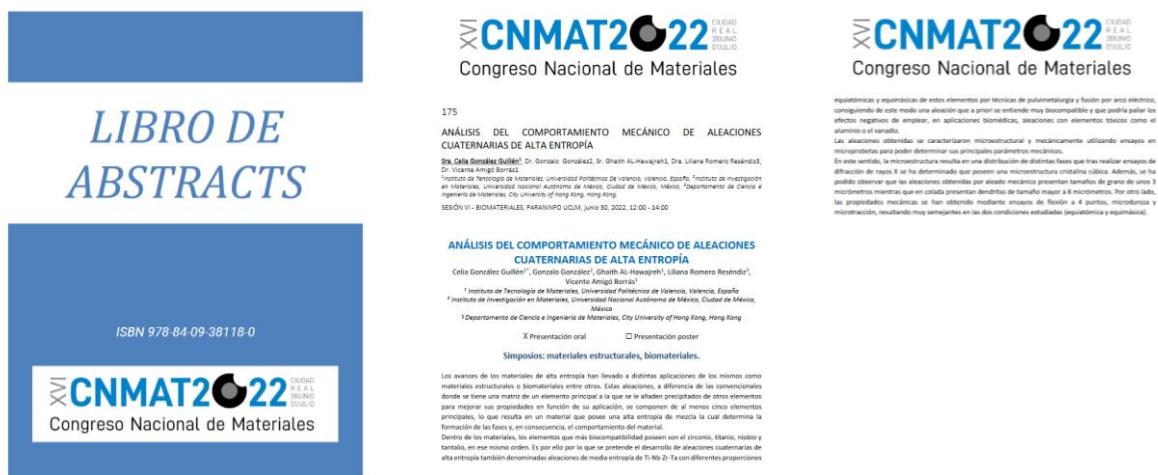


Fig. 94. Abstract presented.



UNIVERSITAT
POLITÈCNICA
DE VALÈNCIA



ESCUELA TÉCNICA
SUPERIOR INGENIERÍA
INDUSTRIAL VALENCIA

ANALYSIS OF THE MECHANICAL BEHAVIOUR AND STRUCTURAL CHARACTERISATION OF HIGH ENTROPY QUATERNARY ALLOYS

DOCUMENT II: BUDGET

CELIA GONZÁLEZ GUILLÉN

Student, Instituto de Tecnología de Materiales, Universitat Politècnica de Valencia, Valencia, Spain

VICENTE AMIGÓ BORRÁS

University Professor, Instituto de Tecnología de Materiales, Universitat Politècnica de Valencia, Valencia, Spain

ÁNGEL VICENTE ESCUDER

Teaching and Research Staff, Instituto de Tecnología de Materiales, Universitat Politècnica de Valencia, Valencia, Spain

LILIANA ROMERO RESENDIZ

Postdoctoral Researcher, Materials Science and Engineering Department, City University of Hong Kong, Hong Kong

CONTENTS

1. UNIT PRICES 1

2. PRICE BREAKDOWN 5

3. EXECUTION BUDGET 20

4. OVERALL BUDGET 23

LIST OF TABLES

Table 46. Workforce price table.....	1
Table 47. Machinery, equipment, and software price table.....	1
Table 48. Consumable materials price table.....	3
Table 49. Breakdown prices for the unit of work 01.....	6
Table 50. Breakdown prices for the unit of work 02.....	7
Table 51. Breakdown prices for the unit of work 03.....	7
Table 52. Breakdown prices for the unit of work 04.....	8
Table 53. Breakdown prices for the unit of work 05.....	9
Table 54. Breakdown prices for the unit of work 06.....	9
Table 55. Breakdown prices for the unit of work 07.....	10
Table 56. Breakdown prices for the unit of work 08.....	10
Table 57. Breakdown prices for the unit of work 09.....	11
Table 58. Breakdown prices for the unit of work 10.....	11
Table 59. Breakdown prices for the unit of work 11.....	11
Table 60. Breakdown prices for the unit of work 12.....	12
Table 61. Breakdown prices for the unit of work 13.....	12
Table 62. Breakdown prices for the unit of work 14.....	13
Table 63. Breakdown prices for the unit of work 15.....	13
Table 64. Breakdown prices for the unit of work 16.....	14
Table 65. Breakdown prices for the unit of work 17.....	15
Table 66. Breakdown prices for the unit of work 18.....	15
Table 67. Breakdown prices for the unit of work 19.....	15
Table 68. Breakdown prices for the unit of work 20.....	16
Table 69. Breakdown prices for the unit of work 21.....	16
Table 70. Breakdown prices for the unit of work 22.....	17
Table 71. Breakdown prices for the unit of work 23.....	18
Table 72. Breakdown prices for the unit of work 24.....	19
Table 73. Budget broken down by chapter 01.....	20
Table 74. Budget broken down by chapter 02.....	21
Table 75. Budget broken down by chapter 03.....	21
Table 76. Budget broken down by chapter 04.....	21

Table 77. Budget broken down by chapter 05..... 22
Table 78. Budget broken down by chapter 06..... 22
Table 79. Budget overview..... 23

1. UNIT PRICES

Throughout the chapter, the cost of carrying out a research project like this will be detailed.

Starting with the workforce costs, the work has been carried out by a project manager, some assistant project managers, a junior engineer, and a laboratory technician, as detailed in **Table 46**, where the abbreviation WF stands for workforce.

Table 46. *Workforce price table.*

WORKFORCE PRICE TABLE			
Code	Description	Units	Price (€/u)
WF01	Project Manager	h	66.00
WF02	Assistant Project Manager	h	33.00
WF03	Junior Engineer	h	16.50
WF04	Laboratory technician	h	24.75

Within the machinery, this is amortised over a range of 3-10 years, and has an annual service of between 1,200 and 1,800 hours, which makes its hourly price as shown in **Table 47**, where MAC stands for machinery.

Table 47. *Machinery, equipment, and software price table.*

MACHINERY, EQUIPMENT, AND SOFTWARE PRICE TABLE						
Code	Description	Units	Unit price (€/u)	Service life (years)	Annual hours of use	Price (€/h)
MAC01	Glove box	U.	15,422.00	5	1,600	1.93
MAC02	Precision balance	U.	1,412.50	5	1,800	0.16
MAC03	Planetary ball mill	U.	26,199.98	5	1,800	2.91

MACHINERY, EQUIPMENT, AND SOFTWARE PRICE TABLE						
Code	Description	Units	Unit price (€/u)	Service life (years)	Annual hours of use	Price (€/h)
MAC04	Metal jar	U.	423.00	3	1,800	0.08
MAC05	Floating bending die	U.	2,416.25	3	1,800	0.45
MAC06	Compacting press	U.	8,841.11	5	1,600	1.11
MAC07	High vacuum furnace	U.	74,510.49	5	1,200	12.42
MAC08	Electric arc furnace	U.	18,928.00	5	1,200	3.15
MAC09	Mastersizer	U.	42,123.42	5	1,800	4.68
MAC10	X-ray equipment	U.	71,816.00	10	1,200	5.98
MAC11	Vacuum pump	U.	2,438.65	3	1,600	0.51
MAC12	Archimedes equipment	U.	680.50	3	1,800	0.13
MAC13	Universal testing machine	U.	52,175.00	5	1,600	6.52
MAC14	Bending tooling	U.	283.99	3	1,600	0.06
MAC15	Micro-tensile tooling	U.	640.80	3	1,600	0.13
MAC16	Micro-compression tooling	U.	235.75	3	1,600	0.05
MAC17	Small punch tooling	U.	485.50	3	1,600	0.10
MAC18	Durometer	U.	19,413.00	10	1,800	1.08
MAC19	Microhardness tester	U.	23,810.40	5	1,800	2.65
MAC20	Optical microscope	U.	66,406.00	5	1,800	7.38
MAC21	Electron microscope FESEM	U.	325,498.30	10	1,600	20.34
MAC22	Electron microscope FIB	U.	548,426.00	5	1,600	68.55
MAC23	Grinding machine	U.	18,972.90	5	1,600	2.37
MAC24	Semi-automatic polishing machine with dosing unit	U.	28,381.30	5	1,600	3.55
MAC25	Vibratory polishing machine	U.	35,627.36	5	1,600	4.45
MAC26	Ultrasonic equipment	U.	8,540.67	3	1,600	1.78

MACHINERY, EQUIPMENT, AND SOFTWARE PRICE TABLE						
Code	Description	Units	Unit price (€/u)	Service life (years)	Annual hours of use	Price (€/h)
MAC27	Ultrasonic cleaning equipment	U.	2,170.37	3	1,600	0.45
MAC28	Mounting press	U.	18,972.44	5	1,600	2.37
MAC29	Milling machine	U.	5,445.66	5	1,200	0.91
MAC30	Cutter	U.	23,545.12	5	1,800	2.62
MAC31	Stove	U.	4,560.65	5	1,600	0.57
MAC32	AgCl electrode	U.	389.99	5	1,800	0.04
MAC33	Pt Counter-electrode	U.	485.00	5	1,800	0.05
MAC34	Potentiostat	U.	19,473.30	5	1,800	2.16
MAC35	Corrosion cell	U.	242.95	5	1,800	0.03
MAC36	Magnetic stirrer with heating plate	U.	352.49	3	1,800	0.07
MAC37	Drop Shape Analyzer	U.	12,455.36	5	1,800	1.38
MAC38	Electron microscope TEM	U.	595,851.40	5	1,600	74.48

Finally, one of the most important parts of the budget is the accounting of the consumables used, which are listed in **Table 48**, where MAT stands for materials.

Table 48. Consumable materials price table.

CONSUMABLE MATERIALS PRICE TABLE			
Code	Description	Units	Price (€/u)
MAT01	Alumina disc	U.	123.00
MAT02	Conductive black resin	kg	90.00
MAT03	Transparent non-conductive resin	kg	85.75
MAT04	Diapro water-based diamond suspension	L	239.20
MAT05	OPS solution	L	78.65

CONSUMABLE MATERIALS PRICE TABLE			
Code	Description	Units	Price (€/u)
MAT06	MD Rag long 9 μm	h	31.15
MAT07	MD chem rag 1 μm	h	0.10
MAT08	Reference stickers	U.	0.10
MAT09	Ethanol	L	17.96
MAT10	Acetone	L	15.51
MAT11	SiC sandpaper (220 mesh)	U.	3.00
MAT12	SiC sandpaper (500 mesh)	U.	3.20
MAT13	SiC sandpaper (1000 mesh)	U.	3.49
MAT14	NaCl	kg	17.40
MAT15	KCl	kg	22.42
MAT16	CaCl ₂	kg	43.56
MAT17	Lactate	L	112.48
MAT18	Stearic Acid	kg	87.50
MAT19	Zinc stearate	U.	58.23
MAT20	Distilled water	L	0.60
MAT21	Kroll's Reagent	L	236.52
MAT22	Diiodomethane	L	4,274.40
MAT23	Ti powder	kg	698.88
MAT24	Nb powder	kg	1,480.96
MAT25	ZrH ₂ powder	kg	2,250.56
MAT26	Ta powder	kg	3,577.60

2. PRICE BREAKDOWN

In order to be able to carry out this research project, different tools, materials, and workforce were needed, which have been grouped into 24 different units of work. In this case, instead of making a chapter about measurements, the hours of work attributed to the workforce, amortisation, and the necessary units of consumable materials have been established for each unit of work shown below.

- UW01. Powder analysis.
- UW02. Powder obtention by mechanical alloying.
- UW03. Mechanical alloying powder analysis.
- UW04. Press and sintering process.
- UW05. Casting process.
- UW06. Mounting.
- UW07. Grinding.
- UW08. Polishing.
- UW09. Special surface preparation.
- UW10. X-Ray Diffraction.
- UW11. Optical Microscopy.
- UW12. Field – Emission Scanning Electron Microscopy.
- UW13. Electron Backscatter Diffraction.
- UW14. Transmission Electron Microscopy.
- UW15. Modulus of elasticity.
- UW16. Archimedes test.
- UW17. Hardness test.
- UW18. Microhardness test.
- UW19. Bending test.
- UW20. Micro-tensile test.
- UW21. Micro-compression test.
- UW22. Small punch.

- UW23. Electrochemical corrosion.
- UW24. Wettability.

In turn, these units of work, whose prices are broken down as shown in the following tables, are referred to the different tasks needed to develop the project.

Specifically, the first unit of work reflects the cost associated with carrying out different analyses on the raw materials used to obtain the different samples worked throughout this project.

Table 49. Breakdown prices for the unit of work 01.

UW01		Powder analysis				
Code	Description	Units	Price (€/u)	Quantity	Amount (€)	
MAC09	Mastersizer	h	4.68	1	4.68	
MAC10	X-ray equipment	h	5.98	1.5	8.97	
MAC21	Electron microscope FESEM	h	20.34	1.0	20.34	
WF01	Project Manager	h	66.00	3	198.00	
WF02	Assistant Project Manager	h	33.00	2	66.00	
WF03	Junior Engineer	h	16.50	11	181.50	
WF04	Laboratory technician	h	24.75	2	49.50	
	3% indirect costs				15.87	
Total per UW01.....:					544.86	

On the other hand, the second unit of work reflects the cost associated with obtaining the mechanical alloying powder in which in a single process that powder can be obtained for the manufacture of several samples with different compositions.

Table 50. Breakdown prices for the unit of work 02.

UW02		Powder obtention by mechanical alloying				
Code	Description	Units	Price (€/u)	Quantity	Amount (€)	
MAC01	Glove box	h	1.93	2	3.86	
MAC02	Precision balance	h	0.16	1	0.16	
MAC03	Planetary ball mill	h	2.91	40	116.40	
MAC04	Metal jar	h	0.08	224	17.92	
MAT23	Ti powder	kg	698.88	0.043	30.05	
MAT24	Nb powder	kg	1,480.96	0.055	81.45	
MAT25	ZrH2 powder	kg	2,250.56	0.055	123.78	
MAT26	Ta powder	kg	3,577.60	0.080	286.21	
WF01	Project Manager	h	66.00	4	264.00	
WF02	Assistant Project Manager	h	33.00	1	33.00	
WF03	Junior Engineer	h	16.50	15	247.50	
WF04	Laboratory technician	h	24.75	10	247.50	
	3% indirect costs				45.05	
Total per UW02.....:					1,546.72	

As with the first unit of work, the third one consists of different equipment and workforce associated with the analysis of powders of a given chemical composition after mechanical alloying.

Table 51. Breakdown prices for the unit of work 03.

UW03		Mechanical alloying powder analysis				
Code	Description	Units	Price (€/u)	Quantity	Amount (€)	
MAC09	Mastersizer	h	4.68	1	4.68	
MAC10	X-ray equipment	h	5.98	1.5	8.97	

UW03		Mechanical alloying powder analysis				
Code	Description	Units	Price (€/u)	Quantity	Amount (€)	
MAC21	Electron microscope FESEM	h	20.34	1	20.34	
WF01	Project Manager	h	66.00	3	198.00	
WF02	Assistant Project Manager	h	33.00	2	66.00	
WF03	Junior Engineer	h	16.50	11	181.50	
WF04	Laboratory technician	h	24.75	2	49.50	
	3% indirect costs				15.87	
Total per UW03.....:					544.86	

In the case of the fourth unit of work, it is envisaged in the breakdown that the 8 samples initially obtained can be prepared in the same sintering cycle.

Table 52. Breakdown prices for the unit of work 04.

UW04		Press and sintering process				
Code	Description	Units	Price (€/u)	Quantity	Amount (€)	
MAC05	Floating bending die	h	0.45	2	0.90	
MAC06	Compacting press	h	1.11	2	2.22	
MAC07	High vacuum furnace	h	12.42	13.5	167.65	
MAT18	Stearic Acid	kg	87.50	0.036	3.15	
MAT19	Zinc stearate	U.	58.23	0.215	12.52	
WF01	Project Manager	h	66.00	2	132.00	
WF02	Assistant Project Manager	h	33.00	0.5	16.50	
WF03	Junior Engineer	h	16.50	8	132.00	
WF04	Laboratory technician	h	24.75	2	49.50	
	3% indirect costs				15.49	
Total per UW04.....:					531.93	

However, from the fifth work unit onwards, unless otherwise stated, the different decomposed prices are obtained considering that each process is carried out for a specific sample.

Table 53. Breakdown prices for the unit of work 05.

UW05		Casting process				
Code	Description	Units	Price (€/u)	Quantity	Amount (€)	
MAC08	Electric arc furnace	h	3.15	1	3.15	
WF01	Project Manager	h	66.00	1	66.00	
WF02	Assistant Project Manager	h	33.00	0.5	16.50	
WF03	Junior Engineer	h	16.50	2	33.00	
WF04	Laboratory technician	h	24.75	1	24.75	
	3% indirect costs				4.30	
Total per UW05.....:					147.70	

Table 54. Breakdown prices for the unit of work 06.

UW06		Mounting				
Code	Description	Units	Price (€/u)	Quantity	Amount (€)	
MAC28	Mounting press	h	2.37	0.2	0.47	
MAT02	Conductive black resin	kg	90.00	0.05	4.50	
MAT19	Zinc stearate	U.	58.23	0.005	0.29	
WF01	Project Manager	h	66.00	0.1	6.60	
WF03	Junior Engineer	h	16.50	0.4	6.60	
WF04	Laboratory technician	h	24.75	0.2	4.95	
	3% indirect costs				0.70	
Total per UW06.....:					24.11	

Table 55. Breakdown prices for the unit of work 07.

UW07		Grinding			
Code	Description	Units	Price (€/u)	Quantity	Amount (€)
MAC23	Grinding machine	h	2.37	0.75	1.78
MAT11	SiC sandpaper (220 mesh)	U.	3.00	1	3.00
MAT12	SiC sandpaper (500 mesh)	U.	3.20	1	3.20
MAT13	SiC sandpaper (1000 mesh)	U.	3.49	1	3.49
WF01	Project Manager	h	66.00	0.25	16.50
WF03	Junior Engineer	h	16.50	1	16.50
WF04	Laboratory technician	h	24.75	0.1	2.48
	3% indirect costs				1.41
Total per UW07.....:					48.36

Table 56. Breakdown prices for the unit of work 08.

UW08		Polishing			
Code	Description	Units	Price (€/u)	Quantity	Amount (€)
MAC24	Semi-automatic polishing machine with dosing unit	h	3.55	0.4	1.42
MAT04	Diapro water-based diamond suspension	L	239.20	0.02	4.78
MAT05	OPS solution	L	78.65	0.02	1.57
MAT06	MD Rag long 9 µm	h	31.15	0.2	6.23
MAT07	MD chem rag 1 µm	h	0.10	0.2	0.02
MAT09	Ethanol	L	17.96	0.05	0.90
WF01	Project Manager	h	66.00	0.1	6.60
WF03	Junior Engineer	h	16.50	0.5	8.25
WF04	Laboratory technician	h	24.75	0.05	1.24
	3% indirect costs				0.93
Total per UW08.....:					31.94

Table 57. Breakdown prices for the unit of work 09.

UW09		Special surface preparation			
Code	Description	Units	Price (€/u)	Quantity	Amount (€)
MAC25	Vibratory polishing machine	h	4.45	12	53.40
WF01	Project Manager	h	66.00	0.5	33.00
WF03	Junior Engineer	h	16.50	3	49.50
WF04	Laboratory technician	h	24.75	0.5	12.38
	3% indirect costs				4.45
Total per UW09.....:					152.73

Table 58. Breakdown prices for the unit of work 10.

UW10		X-Ray Diffraction			
Code	Description	Units	Price (€/u)	Quantity	Amount (€)
MAC10	X-ray equipment	h	5.98	8	47.84
WF01	Project Manager	h	66.00	0.5	33.00
WF02	Assistant Project Manager	h	33.00	2	66.00
WF03	Junior Engineer	h	16.50	4	66.00
WF04	Laboratory technician	h	24.75	1	24.75
	3% indirect costs				7.13
Total per UW10.....:					244.72

Table 59. Breakdown prices for the unit of work 11.

UW11		Optical Microscopy			
Code	Description	Units	Price (€/u)	Quantity	Amount (€)
MAC20	Optical microscope	h	7.38	1	7.38
MAT20	Distilled water	L	0.60	0.05	0.03

UW11		Optical Microscopy				
Code	Description	Units	Price (€/u)	Quantity	Amount (€)	
MAT21	Kroll's Reagent	L	236.52	0.02	4.73	
WF01	Project Manager	h	66.00	0.75	49.50	
WF02	Assistant Project Manager	h	33.00	0.2	6.60	
WF03	Junior Engineer	h	16.50	3	49.50	
WF04	Laboratory technician	h	24.75	0.1	2.48	
	3% indirect costs				3.61	
Total per UW11.....:					123.83	

Table 60. Breakdown prices for the unit of work 12.

UW12		Field - Emission Scanning Electron Microscopy				
Code	Description	Units	Price (€/u)	Quantity	Amount (€)	
MAC21	Electron microscope FESEM	h	20.34	1.5	30.51	
WF01	Project Manager	h	66.00	2	132.00	
WF02	Assistant Project Manager	h	33.00	1	33.00	
WF03	Junior Engineer	h	16.50	5	82.50	
WF04	Laboratory technician	h	24.75	0.25	6.19	
	3% indirect costs				8.53	
Total per UW12.....:					292.73	

Table 61. Breakdown prices for the unit of work 13.

UW13		Electron Backscatter Diffraction				
Code	Description	Units	Price (€/u)	Quantity	Amount (€)	
MAC22	Electron microscope FIB	h	68.55	2.5	171.38	
WF01	Project Manager	h	66.00	1	66.00	

UW13		Electron Backscatter Diffraction				
Code	Description	Units	Price (€/u)	Quantity	Amount (€)	
WF02	Assistant Project Manager	h	33.00	2	66.00	
WF03	Junior Engineer	h	16.50	5	82.50	
WF04	Laboratory technician	h	24.75	0.25	6.19	
	3% indirect costs				11.76	
Total per UW13.....:					403.83	

Table 62. Breakdown prices for the unit of work 14.

UW14		Transmission Electron Microscopy				
Code	Description	Units	Price (€/u)	Quantity	Amount (€)	
MAC22	Electron microscope FIB	h	68.55	4	274.20	
MAC38	Electron microscope TEM	h	74.48	3.5	260.68	
MAC23	Grinding machine	h	2.37	1	2.37	
MAC30	Cutter	h	2.62	1.4	3.67	
WF01	Project Manager	h	66.00	4	264.00	
WF02	Assistant Project Manager	h	33.00	4	132.00	
WF03	Junior Engineer	h	16.50	8	132.00	
WF04	Laboratory technician	h	24.75	3	74.25	
					34.30	
Total per UW14.....:					1,177.47	

Table 63. Breakdown prices for the unit of work 15.

UW15		Modulus of elasticity determination				
Code	Description	Units	Price (€/u)	Quantity	Amount (€)	
MAC26	Ultrasonic equipment	h	1.78	0.25	0.45	

UW15		Modulus of elasticity determination				
Code	Description	Units	Price (€/u)	Quantity	Amount (€)	
WF01	Project Manager	h	66.00	0.1	6.60	
WF02	Assistant Project Manager	h	33.00	0.2	6.60	
WF03	Junior Engineer	h	16.50	0.5	8.25	
WF04	Laboratory technician	h	24.75	0.1	2.48	
	3% indirect costs				0.73	
Total per UW15.....:					25.11	

Then, in UW16, in each run for the determination of the density and porosity, samples with the same composition are measured.

Table 64. Breakdown prices for the unit of work 16.

UW16		Archimedes test				
Code	Description	Units	Price (€/u)	Quantity	Amount (€)	
MAC02	Precision balance	h	0.16	0.5	0.08	
MAC11	Vacuum pump	h	0.51	0.3	0.15	
MAC12	Archimedes equipment	h	0.13	0.5	0.07	
MAC31	Stove	h	0.57	1	0.57	
MAT20	Distilled water	L	0.60	0.5	0.30	
WF01	Project Manager	h	66.00	0.15	9.90	
WF02	Assistant Project Manager	h	33.00	0.1	3.30	
WF03	Junior Engineer	h	16.50	1	16.50	
WF04	Laboratory technician	h	24.75	0.1	2.48	
	3% indirect costs				1.00	
Total per UW16.....:					34.35	

Table 65. Breakdown prices for the unit of work 17.

UW17		Hardness test				
Code	Description	Units	Price (€/u)	Quantity	Amount (€)	
MAC18	Durometer	h	1.08	0.06	0.07	
WF01	Project Manager	h	66.00	0.02	1.32	
WF03	Junior Engineer	h	16.50	0.50	8.25	
	3% indirect costs				0.29	
Total per UW17.....:					9.93	

Table 66. Breakdown prices for the unit of work 18.

UW18		Microhardness test				
Code	Description	Units	Price (€/u)	Quantity	Amount (€)	
MAC19	Microhardness tester	h	2.65	0.4	1.06	
WF01	Project Manager	h	66.00	0.25	16.50	
WF03	Junior Engineer	h	16.50	1	16.50	
	3% indirect costs				1.02	
Total per UW18.....:					35.08	

Table 67. Breakdown prices for the unit of work 19.

UW19		Bending test				
Code	Description	Units	Price (€/u)	Quantity	Amount (€)	
MAC13	Universal testing machine	h	6.52	0.45	2.93	
MAC14	Bending tooling	h	0.06	0.45	0.03	
MAT08	Reference stickers	U.	0.10	2	0.20	
WF01	Project Manager	h	66.00	0.75	49.50	
WF02	Assistant Project Manager	h	33.00	0.1	3.30	

UW19		Bending test				
Code	Description	Units	Price (€/u)	Quantity	Amount (€)	
WF03	Junior Engineer	h	16.50	5	82.50	
WF04	Laboratory technician	h	24.75	0.1	2.48	
	3% indirect costs				4.23	
Total per UW19.....:					145.17	

Table 68. Breakdown prices for the unit of work 20.

UW20		Micro-tensile test				
Code	Description	Units	Price (€/u)	Quantity	Amount (€)	
MAC13	Universal testing machine	h	6.52	0.45	2.93	
MAC15	Micro-tensile tooling	h	0.13	0.45	0.06	
MAC29	Milling machine	h	0.91	1	0.91	
MAC30	Cutter	h	2.62	0.75	1.97	
MAT08	Reference stickers	U.	0.10	2	0.20	
WF01	Project Manager	h	66.00	0.75	49.50	
WF02	Assistant Project Manager	h	33.00	0.3	9.90	
WF03	Junior Engineer	h	16.50	4	66.00	
WF04	Laboratory technician	h	24.75	0.1	2.48	
	3% indirect costs				4.02	
Total per UW20.....:					137.97	

Table 69. Breakdown prices for the unit of work 21.

UW21		Micro-compression test				
Code	Description	Units	Price (€/u)	Quantity	Amount (€)	
MAC13	Universal testing machine	h	6.52	0.45	2.93	

UW21		Micro-compression test			
Code	Description	Units	Price (€/u)	Quantity	Amount (€)
MAC16	Micro-compression tooling	h	0.05	0.45	0.02
MAC30	Cutter	h	2.62	1.5	3.93
MAT08	Reference stickers	U.	0.10	2	0.20
WF01	Project Manager	h	66.00	0.75	49.50
WF02	Assistant Project Manager	h	33.00	0.3	9.90
WF03	Junior Engineer	h	16.50	5.5	90.75
WF04	Laboratory technician	h	24.75	0.1	2.48
	3% indirect costs				4.79
Total per UW21.....:					159.71

Table 70. Breakdown prices for the unit of work 22.

UW22		Small punch			
Code	Description	Units	Price (€/u)	Quantity	Amount (€)
MAC13	Universal testing machine	h	6.52	0.6	3.91
MAC17	Small punch tooling	h	0.10	0.6	0.06
MAC30	Cutter	h	2.62	0.75	1.97
MAT08	Reference stickers	U.	0.10	2	0.20
WF01	Project Manager	h	66.00	0.75	49.50
WF02	Assistant Project Manager	h	33.00	0.3	9.90
WF03	Junior Engineer	h	16.50	7	115.50
WF04	Laboratory technician	h	24.75	0.1	2.48
	3% indirect costs				5.51
Total per UW22.....:					189.03

Table 71. Breakdown prices for the unit of work 23.

UW23		Electrochemical corrosion			
Code	Description	Units	Price (€/u)	Quantity	Amount (€)
MAC27	Ultrasonic cleaning equipment	h	0.45	0.25	0.11
MAC32	AgCl electrode	h	0.04	3	0.12
MAC33	Pt Counter-electrode	h	0.05	3	0.15
MAC34	Potentiostat	h	2.16	3	6.48
MAC35	Corrosion cell	h	0.03	3	0.09
MAC36	Magnetic stirrer with heating plate	h	0.07	0.25	0.02
MAT09	Ethanol	L	17.96	0.02	0.36
MAT10	Acetone	L	15.51	0.02	0.31
MAT14	NaCl	kg	17.40	0.0006	0.01
MAT15	KCl	kg	22.42	0.000038	0.001
MAT16	CaCl ₂	kg	43.56	0.000023	0.001
MAT17	Lactate	L	112.48	0.000515	0.06
MAT20	Distilled water	L	0.60	0.08	0.05
WF01	Project Manager	h	66.00	0.5	33.00
WF02	Assistant Project Manager	h	33.00	0.1	3.30
WF03	Junior Engineer	h	16.50	7	115.50
WF04	Laboratory technician	h	24.75	0.1	2.48
	3% indirect costs				4.86
Total per UW23.....:					166.90

Table 72. Breakdown prices for the unit of work 24.

UW24		Wettability			
Code	Description	Units	Price (€/u)	Quantity	Amount (€)
MAC37	Drop Shape Analyzer	h	1.38	0.25	0.35
MAT20	Distilled water	L	0.60	0.01	0.01
MAT22	Diiodomethane	L	4,274.40	0.01	42.74
WF01	Project Manager	h	66.00	0.2	13.20
WF03	Junior Engineer	h	16.50	1	16.50
	3% indirect costs				2.18
Total per UW24.....:					74.98

3. EXECUTION BUDGET

At the same time, the units of work detailed above have been grouped into different budget chapters. These are as follows:

- 01. Obtaining samples by mechanical alloying.
- 02. Obtaining the samples by casting.
- 03. Metallographic preparation of samples.
- 04. Microstructural analysis of samples.
- 05. Mechanical analysis of samples.
- 06. Chemical analysis of samples.

In this point, at the end of each table, the execution budget associated with each chapter is shown after taking the measurements corresponding to each unit of work who take part in.

Table 73. Budget broken down by chapter 01.

CHAPTER 01. Obtaining samples by mechanical alloying						
Code	Description	Units	Price (€/u)	Quantity	Amount (€)	
UW01	Powder analysis	U.	544.86	4	2,179.44	
UW02	Powder obtention by mechanical alloying	U.	1,546.72	1	1,546.72	
UW03	Mechanical alloying powder analysis	U.	544.86	2	1,089.72	
UW04	Press and sintering process	U.	531.93	1	531.93	
Total CHAPTER 01:					5,347.81	

Table 74. Budget broken down by chapter 02.

CHAPTER 02. Obtaining the samples by casting					
Code	Description	Units	Price (€/u)	Quantity	Amount (€)
UW05	Casting process	U.	147.70	2	295.40
Total CHAPTER 02:					295.40

Table 75. Budget broken down by chapter 03.

CHAPTER 03. Metallographic preparation of samples					
Code	Description	Units	Price (€/u)	Quantity	Amount (€)
UW06	Mounting	U.	24.11	4	96.48
UW07	Grinding	U.	48.36	8	386.88
UW08	Polishing	U.	31.94	8	255.54
UW09	Special surface preparation	U.	152.73	4	610.92
Total CHAPTER 03:					1,253.34

Table 76. Budget broken down by chapter 04.

CHAPTER 04. Microstructural analysis of samples					
Code	Description	Units	Price (€/u)	Quantity	Amount (€)
UW10	X-Ray Diffraction	U.	244.72	4	978.88
UW11	Optical Microscopy	U.	123.83	4	495.32
UW12	Field - Emission Scanning Electron Microscopy	U.	292.73	6	1,756.38
UW13	Electron Backscatter Diffraction	U.	403.83	4	1,615.33
UW14	Transmission Electron Microscopy	U.	1,177.47	4	4,709.88
Total CHAPTER 04:					9,555.79

Table 77. Budget broken down by chapter 05.

CHAPTER 05. Mechanical analysis of samples					
Code	Description	Units	Price (€/u)	Quantity	Amount (€)
UW15	Modulus of elasticity determination	U.	25.11	8	200.88
UW16	Archimedes test	U.	34.35	4	137.40
UW17	Hardness test	U.	9.93	8	79.44
UW18	Microhardness test	U.	35.08	4	140.32
UW19	Bending test	U.	145.17	6	871.02
UW20	Micro-tensile test	U.	137.97	4	551.88
UW21	Micro-compression test	U.	159.71	6	958.26
UW22	Small punch	U.	189.03	10	1,890.30
Total CHAPTER 05:					4,829.50

Table 78. Budget broken down by chapter 06.

CHAPTER 06. Chemical analysis of samples					
Code	Description	Units	Price (€/u)	Quantity	Amount (€)
UW06	Mounting	U.	24.11	12	289.32
UW07	Grinding	U.	48.36	12	580.32
UW08	Polishing	U.	31.94	12	383.28
UW23	Electrochemical corrosion	U.	166.90	12	2,002.80
UW24	Wettability	U.	74.98	4	299.92
Total CHAPTER 06:					3,555.64

4. OVERALL BUDGET

Finally, all the different chapters detailed in the previous section are grouped together and after applying 13% overheads costs, 6% know-how tax and the corresponding 21% V.A.T., a base tender budget of **thirty-five thousand seven hundred and sixty-three euros and forty-eight cents** is obtained.

Table 79. *Budget overview.*

Invoice items		Total amount (€)
01	Obtaining samples by mechanical alloying	5,347.81
02	Obtaining the samples by casting	295.40
03	Metallographic preparation of samples	1,253.34
04	Microstructural analysis of samples	9,555.79
05	Mechanical analysis of samples	4,829.50
06	Chemical analysis of samples	3,555.64
Material execution budget		24,837.48
Overheads costs (13%)		3,228.87
Know-how tax (6%)		1,490.25
Contractual execution budget		29,556.60
V.A.T. (21%)		6,206.89
BASE TENDER BUDGET		35,763.48

